Research Square

Preprints are preliminary reports that have not undergone peer review.
They should not be considered conclusive, used to inform clinical practice,
or referenced by the media as validated information.

Hydrogen sulfide binds to the catalytic zinc ion in HDAC6 to modulate enzyme activity via an alternative deacetylation pathway

Yi-Chun Zhu

yczhu@shmu.edu.cn

Fudan University https://orcid.org/0000-0002-0873-2957

Chen Sun

Shanghai Key Laboratory of Bioactive Small Molecules, Department of Physiology and Pathophysiology, School of Basic Medical Sciences, Fudan University Shanghai Medical College, Shanghai 200032, Chin

Yin-fang Wang

Shanghai Key Laboratory of Bioactive Small Molecules, Department of Physiology and Pathophysiology, School of Basic Medical Sciences, Fudan University Shanghai Medical College, Shanghai 200032, Chin

Sheng-Yang Cai

Fudan University

Kui-fang Xie

Shanghai Key Laboratory of Bioactive Small Molecules, Department of Physiology and Pathophysiology, School of Basic Medical Sciences, Fudan University Shanghai Medical College, Shanghai 200032, Chin

Xue-Pan Mu

Shanghai Key Laboratory of Bioactive Small Molecules, Department of Physiology and Pathophysiology, School of Basic Medical Sciences, Fudan University Shanghai Medical College, Shanghai 200032, Chin

Zhini Zhu

Fudan University

Yulin Chao

Shanghai Stomatological Hospital, School of Stomatology, Shanghai Key Laboratory of Medical Epigenetics, International Co-laboratory of Medical Epigenetics and Metabolism, Fudan University

Zixuan Zhou

Shanghai Stomatological Hospital, School of Stomatology, Shanghai Key Laboratory of Medical Epigenetics, International Co-laboratory of Medical Epigenetics and Metabolism, Fudan University

Xiqing Bian

Macau University of Science and Technology https://orcid.org/0000-0003-2319-2271

Wen Miu

State Key Laboratory of Quality Research in Chinese Medicine and School of Pharmacy, Macau University of Science and Technology, Avenida WaiLong, Taipa, Macau 999078, China

Jianlin Wu
Macau University of Science and Technology https://orcid.org/0000-0002-3875-185X
Jingwei Weng
Fudan University
Jia-Qi Zhu
Fudan University
Ying Chen
Wenlong Xue
Fudan University
Meng-yao Li
Shanghai Key Laboratory of Bioactive Small Molecules, Department of Physiology and Pathophysiology, School of Basic Medical Sciences, Fudan University Shanghai Medical College, Shanghai 200032, Chin
Ai-Qiu Chi
Fudan University
Qian Ding
Macau University of Science and Technology
Ming-Jie Wang
Fudan University
Bei-Bei Tao
Fudan University
Igor Ying Zhang
Fudan university, Shanghai, China https://orcid.org/0000-0002-8703-1912
Yi-Zhun Zhu
Macau University of Science and Technology
Qianhui Qu
Fudan University https://orcid.org/0000-0002-5753-2599

Biological Sciences - Article

Keywords: Histone deacetylase 6, Hydrogen sulfide, Zinc-active-site, Metalloenzymes, Cell migration, H2S senser

Posted Date: January 12th, 2026

DOI: https://doi.org/10.21203/rs.3.rs-777997/v1

License: This work is licensed under a Creative Commons Attribution 4.0 International License.
Read Full License

Additional Declarations: There is **NO** Competing Interest.

Version of Record: A version of this preprint was published at Nature Communications on September 23rd, 2026. See the published version at https://doi.org/10.1038/s41467-026-77932-z.

Hydrogen sulfide binds to the catalytic zinc ion in HDAC6 to modulate enzyme activity via an alternative deacetylation pathway

Running title: H_2S functions as a micro-modulator at the zinc-active-site of HDAC6

Chen Sun[1, 2], Yin-Fang Wang[1, 7], Sheng-Yang Cai[1], Kui-Fang Xie[1], Xue-Pan Mu[1], Zhi-Ni Zhu[3, 4], Yu-Lin Chao[3, 4], Zi-Xuan Zhou[3, 4], Xi-Qing Bian[2], Wen Miao[2], Jian-Lin Wu[2], Jingwei Weng[6], Jia-Qi Zhu[1], Ying Chen[1], Wen-Long Xue[1], Meng-Yao Li[1], Ai-Qiu Chi[1], Qian Ding[2], Ming-Jie Wang[1], Bei-Bei Tao[1], Igor Ying Zhang[6], Yi Zhun Zhu[2,5, *], Qian-Hui Qu[3, 4, *], Yi-Chun Zhu[1, *,#]

[1]Shanghai Key Laboratory of Bioactive Small Molecules, Department of Physiology and Pathophysiology, School of Basic Medical Sciences, Fudan University Shanghai Medical College, Shanghai 200032, China

[2]State Key Laboratory of Quality Research in Chinese Medicine and School of Pharmacy, Macau University of Science and Technology, Avenida WaiLong, Taipa, Macau 999078, China

[3]Shanghai Stomatological Hospital, School of Stomatology, Institutes of Biomedical Sciences, Fudan University, Shanghai, China

[4]Shanghai Key Laboratory of Medical Epigenetics, International Co-laboratory of Medical Epigenetics and Metabolism (Ministry of Science and Technology), Department of Systems Biology for Medicine, Fudan University, Shanghai, 200032, China

[5]Department of Pharmacology, School of Pharmacy, Fudan University, Shanghai 200433, China

[6]Department of Chemistry, Fudan University, Shanghai 200438, China

[7]Central Laboratory, Putuo Hospital, Shanghai University of Traditional Chinese Medicine, Shanghai 200062, China

#Lead contact

***Corresponding author:**

Prof. Yi-Chun Zhu, M.D., Ph.D.

Department of Physiology and Pathophysiology

School of Basic Medical Sciences

Fudan University Shanghai Medical College

138 Yi Xue Yuan Road Shanghai 200032, China

Tel: +086 21 5423 7098

E-mail address: yczhu@shmu.edu.cn (Y. C. Zhu)

Dr. Qian-Hui Qu, Ph.D.

Shanghai Stomatological Hospital

School of Stomatology

Institutes of Biomedical Sciences

Fudan University

138 Yi Xue Yuan Road Shanghai 200032, China

Tel: +086 21 5423 7821

E-mail address: qqh@fudan.edu.cn (Q. H. Qu)

Prof. Yi Zhun Zhu, M.D., Ph.D.

School of Pharmacy

Macau University of Science and Technology

Avenida WaiLong, Taipa, Macau 999078, China

Tel: +853 8897 2880

E-mail address: yzzhu@must.edu.mo (Y. Z. Zhu)

Abstract

The present study aims to examine if a tiny gas molecule, hydrogen sulfide (H_2S), directly binds to the catalytic zinc ion of histone deacetylase 6 (HDAC6) to regulate enzyme activity via a mechanism beyond the post-translational modifications (PTMs) theory. H_2S was found to coordinate with the catalytic metal ions in a series of metalloenzymes centered by zinc, ferrum, calcium, manganese, or copper via sulfur-metal coordination bonds evidenced by formation of specific localized molecular orbitals (LMOs). In HDAC6, H_2S diffused to the bottom of active-site tunnel to identify the catalytic zinc ion yielding an S–Zn bond involving interactions of atom/molecular orbitals to promote enzyme activity. The binding between HDAC6 and H_2S was dependent on H_2S concentrations as measured using surface plasmon resonance (SPR). Quantum chemical (QC) calculations further uncovered a new deacetylation pathway modulated by H_2S. This alternative reaction was characterized with an H_2S-mediated nucleophilic attack generating a novel product, thioacetic acid, which was identified in cell-free reactions, cultured cells, mouse organs and human serums. Such alternative reaction had a much lower energy barrier in the rate-limiting reaction step resulting in much higher reaction efficiency. The cryo-electron microscopy (cryo-EM) structure of human HDAC6 also revealed a rather wide active-site tunnel in CD2 which allowed substrate binding for a series of substrates in contrast to a narrow and twisted active-site tunnel in CD1. QC calculations also revealed the mechanism of H_2S recycling inside the CD2-active-site. In cultured cells and a mouse model of hind-limb ischemia, H_2S-induced increase in cell migration and angiogenesis was dependent on HDAC6.

The CD2-active-site was essential in H_2S-induced increase in HDAC6 activity and cell migration, as examined in the cells expressing a series of recombinant HDAC6 variants with mutations to inactivate either CD1 or CD2 active sites. Acetylomics regulated via the CSE/H_2S-HDAC6 pathway were also displayed revealing 7 regulated proteins relevant to cell migration in addition to well-established α-tubulin. In conclusion, H_2S directly identifies multiple catalytic metal ions in the metalloenzyme family via interaction of molecular/atom orbitals. The biochemical role of such an H_2S coordination was embodied in HDAC6 where H_2S modulated an alternative deacetylation pathway coupled with generation of thioacetic acid to promote cell migration and angiogenesis, suggesting a mechanism of protein regulation beyond the current PTMs concept as well as a role of HDAC6 as an H_2S senser.

Key words: Histone deacetylase 6; Hydrogen sulfide; Zinc-active-site; Metalloenzymes; Cell migration; H_2S senser.

Introduction

Post-translational modifications (PTMs) have been established as one of the fundamental mechanisms in regulating the function of proteins[1]. However, whether the current PTMs theory explains all kinds of protein regulation at the post-translational level remains unknown. A tiny gas transmitter, hydrogen sulfide (H_2S), has recently been found to directly bind to the copper ion in the active site of Cu/Zn-SOD using X-ray crystallography[2]. On the other hand, exceeding 6000 enzymes have been found in biology and medicine to date, among which about one-third are metalloenzymes[3-6]. The metalloenzymes are characterized with active sites centered with certain kinds of metal ions including zinc, ferrum, calcium, manganese, and copper. Among these, more than half of the total metalloenzyme family members are zinc-centered metalloenzymes[5]. The binding between H_2S and the copper-active-site in Cu/Zn-SOD[2] inspires us to propose a hypothesis that H_2S might bind to multiple catalytic metal ions in the active sites in the entire metalloenzyme family including zinc-centered metalloenzymes to regulation enzyme function via some mechanisms beyond the current PTMs theory. Significantly, H_2S is a ligand too tiny to identify its target molecule via the "key-and-lock" theory which explains how a ligand recognizes its "receptor"[7,8]. Obviously, the spatial configuration of H_2S is not sufficient to form a "key". Certain mechanisms beyond molecular conformation such as quantum mechanisms might be involved in the for H_2S to recognize its target molecules. Here, we start with testing potential binding between H_2S and most kinds of catalytic metal ions in a series of metalloenzymes. Among these, H_2S binding and regulation at a particular zinc-centered metalloenzyme,

i.e., histone deacetylase 6 (HDAC6), would be extensively investigated to embody the biochemical role of such an H_2S binding.

HDAC6 has been recognized as a metalloenzyme with two zinc-centered catalytic domains, i.e., CD1 and CD2. Human HDAC6 (hHDAC6) is a unique member of the HDAC family with a complicated structure constructed by 1215 amino acid residues[9]. Its extensive substrate-binding selection feature enables the enzyme to deacetylate a series of cytoplasmic substrates such as α-tubulin, cortactin, heat shock protein 90, tau protein, and peroxiredoxin[10,11]. HDAC6 regulates various cell functions including cell migration, endocytosis, protein degradation, and autophagy[12,13] H_2S is endogenously generated in various tissues/organs in mammalians to serve as a signaling transmitter[14-16]. Moreover, H_2S levels are decreased in a variety of human diseases including hypertension[17], type 2 diabetes[18], and heart failure[19]. In this context, how H_2S levels are sensed also deserves to be examined including the potential senser role of HDAC6.

HDAC6 seems to serve as one of the hubs for intracellular signaling networks by catalyzing the deacetylation reactions of multiple important cytoplasmic proteins. The mechanisms underlying such an extensive substrate-binding selection feature remain unknown. The tandem structure of hHDAC6 including both CD1 and CD2 domains has not been completely resolved owing to the difficulties to crystalize its protein with complete structure[20,21]. Resolution of the tandem structure of hHDAC6 might also provide some structural insights into the distinguished substrate-binding selection feature between CD1 and CD2. This might also help to clarify the role of CD1 and CD2 in transducing the H_2S signals to regulate enzyme activity and cell migration.

Taken together, the present study aims to examine if H_2S binds to the zinc-active-site of hHDAC6 to regulate enzyme activity and cell function via a mechanism beyond the current PTMs theory. How such an H_2S binding might reversibly regulate the catalytic activity of this zinc-center metalloenzyme would also be investigated.

Results

H_2S binds to the catalytic metal ions in a series of metalloenzymes centered by zinc, ferrum, calcium, manganese, or copper via sulfur-metal coordination bonds

An HS^- (a major component of H_2S solution) spontaneously diffused to the CD2-active-site of HDAC6 with its thermal motion and finally bound to the catalytic zinc ion at the bottom of the active-site-tunnel as shown in molecular dynamic (MD) simulations (Figure 1a – d and S1; Video S1). The RMSD (HS^- fit to backbone) values converged to a narrow range of ~4 Å within 52 ns and remained stable till the end of the simulation (Figure 1b). The final HS^--binding was coupled with dissociation of an H_2O molecule originally bound at zinc ion (Figure 1b and c, Video S1). Such an HS^- binding was abolished when the catalytic zinc ion was deleted from the active site of HDAC6-CD2. This was shown in discrete RMSD (HS^- fit to backbone) values oscillating in a range as large as ~110 Å during the 1000 ns simulation period in contrast to converged RMSD values (< 4 Å) in the active site with Zn^{2+} ion (Figure S2a1 and b1; Video S2). The catalytic zinc ion exposed to the inner cavity of active-site-tunnel served as a specific binding site for HS^- diffused through the active-site-tunnel.

The nature of such a binding was further examined using quantum chemical (QC) calculations. The optimized structure of the active site of HDAC6-CD2 bound with HS^- was shown in Figure 1e where a coordination bond was formed between sulfur and zinc with a bond length of 2.37 Å. S–Zn bond order was 0.92 (fuzzy bond order) (Figure 1e) and 0.63 (Mayer bond order) (Figure S3b). Bond order revealed the average number of electron pairs shared between two bonding atoms. Calculation of localized molecular

orbitals (LMO) using Pipek-Mezey algorism with Mulliken and Becke population revealed orbitals with typical σ characteristics (red arrow) between the sulfur and zinc atoms (Figure 1e and S3b). Bond order density (BOD) was also calculated to visualize the global spatial distribution of the fuzzy bond order of the S–Zn bond from a real space perspective (Figure S4a). Natural adaptive orbital (NAdO) was calculated to decompose the *n*-center bonding indices used in real space theories of the S–Zn bond into one-electron contributions. NAdO with the largest eigenvalue (0.69) was shown in Figure S4c). The sum of all NAdO eigenvalues was equal to fuzzy bond order (0.92) of the S–Zn bond.

The mechanisms underlying such bond formation were further investigated. A major increase in electron density (red arrow) between the sulfur and zinc atoms owing to the interaction between HS^- and the catalytic zinc ion of HDAC6-CD2 was shown in isosurface maps (Figure S5a1) and contour maps (Figure S5a2) of electron density difference (EDD). The composition of the S–Zn bond was further investigated using charge decomposition analysis (CDA). As shown in Figure 1f, particular fragment orbitals of HDAC6-CD2-active-site (165, 166, 167, and 171) and HS^- (8 and 9) jointly contributed to the complex orbitals (175, red arrow) between S and Zn atoms in the form of σ-donation. Among these orbitals, orbital 171 was unoccupied which facilitated electron transfer from HS^- (8 and 9) to HDAC6-CD2-active-site resulting in net electron transfer of 0.086 (d-b value). In contrast, no unoccupied orbital was involved in HDAC6-CD2 coordinated with H_2O where less electron (d-b = 0.0257) was transferred to the enzyme active site (Figure S6). In addition, extended CDA (ECDA)

was further calculated yielding a total charge transfer of 0.456 from HS^- to the Zn active site. The contribution of natural orbitals for chemical valence (NOCV) pairs to orbital deformation density induced by orbital interaction upon HS^- coordination was further examined using extended transition state - NOCV (ETS-NOCV). Alteration in electron density of NOCV pair 1 was shown in Figure S7a. There was a σ-donation of charge transfer (black arrow) of 0.403 from NOCV ψ_{1637} to NOCV ψ_1 in NOCV pair 1 with orbital stabilization energies of −26.7 kcal/mol upon HS^- coordination. The HDAC6-CD2 structure coordinated with H_2O served as a control throughout all calculations (Figure S3 – S7).

The above QC calculations showed that HS^- recognized and bound with the zinc active site of HDAC6-CD2 by the interaction of a series of molecular/atom orbitals resulting in the formation of an S–Zn coordination bond. Such quantum events were also coupled with electron transfer to the enzyme active site which might subsequently change enzyme functions. Actually, the frontier molecular orbitals of HDAC6-CD2-active-site, including highest occupied molecular orbital (HOMO) and lowest unoccupied molecular orbital (LUMO) were also significantly changed upon HS^- coordination (Figure S8a) resulting in a decreased energy gap between HOMO and LUMO as compared with that of H_2O coordination (Figure S8b).

Interestingly, such a sulfur-metal coordination bond might also be formed in other members of the huge metalloenzyme family. In zinc-centered metalloenzymes, HS^- was also found to bind to the enzyme active sites of HDAC10 (Figure S9) and angiotensin converting enzyme (ACE) (Figure S10) via an S–Zn coordination bond. HS^- also bound

to the catalytic metal ions in a ferrum-centered metalloenzyme (histone lysine demethylase, PHF8; up to 3 HS^- to 1 Fe^{2+}) (Figure S11), a calcium-centered metalloenzyme (phospholipase A2) (Figure S12), and a manganese-centered metalloenzyme (arginase-1; 1 HS^- to 2 Mn^{2+}) (Figure S13) by formation of S–metal coordination bonds. In contrast, HS^- was not able to bind to the metal active site in certain metalloenzymes such as oxygenated hemocyanin II where two catalytic Cu^{2+} ions were fully coordinated (Figure S14a and b). Whereas, HS^- coordinated with the catalytic copper ions in deoxygenated hemocyanin II where two catalytic Cu^+ ions were not fully coordinated (Figure S14c). In certain enzymes with an active site without exposed catalytic metal ions such as sirtuin 2, HS^- did not coordinate to the structural Zn^{2+} ion contained in the enzyme (Figure S15a) nor to the non-metallic active site (Figure S15b). This was evidenced by an energy minimum of HS^- found at least 4.20 Å (S-N distance) away from the catalytic residue, H187, in the active site of sirtuin 2 (Figure S15b1). In addition, weak binding between HS^- and sirtuin 2 active site was also proved by a binding energy of 10.0 kcal/mol in contrast to a negative value of –142.5 kcal/mol found between HS^- and HDAC6 (Figure S15b2). Likewise, no HS^- binding was found at the structural potassium ions contained inside HDAC6-CD2 (Figure 1g and S2b).

These data suggest that H_2S might directly target various types of catalytic metal ions in the huge metalloenzyme family via particular S–metal coordination bonds (Figure 1h). In the present study, the biological role of such S–metal coordination was extensively examined in HDAC6, a zinc-centered metalloenzyme, which belongs to the

most populated child family in the entire metalloenzyme family.

H_2S binds directly to the catalytic zinc ion in the CD2-active-site of hHDAC6 to mediate a facilitated deacetylation reaction pathway

S-sulfhydration was not identified in hHDAC6-WT protein incubated with NaHS (12 μM) for 1 hour using high performance liquid chromatography-tandem mass spectrometry (HPLC-MS) analysis (Figure S16e). Moreover, the direct interaction between H_2S and HDAC6 was examined using surface plasmon resonance (SPR). The SPR sensorgram with a quick rise upon NaHS administration and a fast decline to the baseline upon washup, reflecting a reversible binding between H_2S and the hHDAC6-CD1-2 protein (K_d = 3.55 × 10^{-7} M) (Figure 2b and d). Such a binding was positively correlated to the concentrations of NaHS ranging from 0.023 to 12.00 μM (Figure 2b). This binding seemed to reach a platform at concentrations beyond 12.00 μM and to decline at very high concentrations ranging from 30 to 600 μM (Figure S16a and b). The SPR assay was validated by a zinc-specific inhibitor of HDAC6, Trichostatin A (TSA) as the control ligand and a mimic substrate of HDAC6, which showed a similar reversible binding sensorgram (K_d = 1.53 × 10^{-7} M) (Figure 2a and c). The SPR sensorgram for binding between TSA and the hHDAC6-CD1-2 protein was significantly changed in the presence of 600 μM NaHS (Figure S16d) but not in the presence of 12 μM NaHS (Figure S16c), indicating a decreased substrate-binding in the presence of high concentration of NaHS. Moreover, such binding assays were carried out between H_2S/TSA and hHDAC6-CD1-2 deprived of the zinc ions using an ion-

chelating agent. No binding signal was found in the SPR sensorgram in the reaction between H_2S and zinc-eliminated hHDAC6-CD1-2 (Figure 2g), nor in the reaction between TSA and zinc-eliminated hHDAC6-CD1-2. Indeed, hHDAC6-CD1-2 was inactivated upon zinc-elimination (Figure 2e and f). The data suggested that the binding between H_2S and hHDAC6-CD1-2 was dependent on the zinc ions contained in the enzyme active sites.

H_2S-induced increase in catalytic activity of hHDAC6 is dependent on the CD2-active-site

A series of hHDAC6 mutant/WT protein variants along with the human sirtuin 2 (hSirt2) protein were expressed and purified to examine the direct effects of H_2S in regulating their deacetylation activity (Figure 3a and Figure S17a). A fluorogenic peptide substrate derived from α-tubulin was used as a substrate to assess the deacetylation activity of these hHDAC6 variants. A fluorogenic peptide substrate derived from p53 was used as a substrate to assess the activity of hSirt2. Steady-state kinetics showed that hHDAC6-WT and hHDAC6-H216A (a CD1-active-site-inactive mutant) exhibited similar activity in catalyzing the substrate, while the CD2-active-site-inactive mutants (hHDAC6-H611A and hHDAC6-Y782F) and the mutant inactive at both the CD1- and CD2-active-site (hHDAC6-H216/611A) exhibited no catalytic activity on the substrate (Figure 3b and Table 3-1), indicating the CD2-active-site was the exclusive catalytic site for such substrate. The dose-response relationship experiment showed that a low concentration of NaHS (6 - 60 μM) significantly

increased the activity of hHDAC6-WT reaching its peak at a concentration of 12 μM, while an inhibitory effect was observed at a higher concentration of NaHS (>120 μM) (Figure 3c). Whereas, such inhibitory effects of NaHS observed at high concentration were reversible as shown with a recovery of the enzyme activity following a washout of H_2S by buffer exchange (Figure 3f). Similar dose-response to NaHS treatment was observed in hHDAC6 protein containing both CD1- and CD2 active-sites without the zinc-finger (ZNF) ubiquitin-binding domain (hHDAC6-CD1-2) construct (Figure S17b). Steady-state kinetics revealed that NaHS treatment (12 μM) led to a more than one-fold increase in catalytic efficiency (k_{cat}/K_M) in the hHDAC6-WT construct (Figure 3d and Table 3-2) and a 4-fold increase in catalytic efficiency in the hHDAC-H216A construct (Figure 3e and Table 3-2). NaHS administration (12 μM) also increased the activity in deacetylating the full-length α-tubulin substrate by 32% (Figure S17c and d). In contrast, NaHS did not affect the enzyme activity of hSirt2 which is a cytoplasmic deacetylase without a metal-active-site (Figure 3g and Table 3-2).

A unique produnct, thioacetic acid, was identified in HDAC6-catalized deacetylation reactions with H_2S in a cell-free system and in a series of biological samples

Thioacetic acid (CH_3COSH) was identified in cell-free deacetylation reaction mixture containing hHDAC6-CD1-2 and the fluorogenic substrate derived from α-tubulin in the presence of NaHS (12 μM) using Ultra-high performance liquid chromatography-tandem triple quadrupole mass spectrometry (UHPLC-qqq-MS) analysis, while no

thioacetic acid was found in such cell-free system in the absence of NaHS (Figure 3h and Figure S18). Thioacetic acid was also measured in living cells in the presence or absence of NaHS with or without knockout of HDAC6. In intact wild-type (WT) 293T cells, thioacetic acid was identified at a level of 204 ± 24 nM (Figure S19b). Treatment with NaHS (60 μM) caused a significant increase in cellular thioacetic acid by 216% and this increase was blunted in HDAC6 knockout cells (Figure 3i). Most notably, the knockout of HDAC6 itself caused an unexpected increase in thioacetic acid levels (Figure 3i). The data suggests that HDAC6 might not be the solitary site for generations of endogenous thioacetic acid. In contrast, HDAC6 might also serve as an enzyme for degradation of endogenous thioacetic acid. This HDAC6-mediated degradation of thioacetic acid was further confirmed in a cell-free system, where a significant decline in thioacetic acid levels was observed in thioacetic acid solutions containing HDAC6 in comparison with that without HDAC6 (Figure 3k). Thioacetic acid was also measured in various mouse organs, including the liver, kidney, heart, lung, brain, spleen, muscle and serum. Among which, thioacetic acid was identified in the liver and serum with basal levels of 1044 ± 215 nM and 1139 ± 152 nM (Figure S19a), respectively. Acute treatment with NaHS (30 μmol/kg/day) caused a significant increase in liver thioacetic acid levels in mice in comparison with that treated with vehicle (Figure 3j). Additionally, thioacetic acid was identified in the serum in healthy human at a level of 264 ± 68 nM (Figure 3l, Figure S19b).

Determination of the tandem structure of hHDAC6

The structure of the tandem catalytic domains of the hHDAC6 was determined using cryo-electron microscopy (cryo-EM) single particle analysis to provide necessary structural information to support further studies to examine the mechanisms underlying H_2S-induced increase in HDAC6 activity. The tandem catalytic domains of hHDAC6 (A84-R835, designated as hHDAC6-CD1-2) was expressed and purified. A cryo-EM map was obtained by image processing of the hHDAC6-CD1-2 datasets which was refined to 3.86-Å resolution and used for model building (Figure S20a, Figure S22e and Figure S23). The cryo-EM map showed a deteriorated density quality on one end-tip of the map, indicating high flexibility in this region as indicated with a red circle (Figure S20b and c). A start-up model was created using AlphaFold 2[22] for model building and refinement (Figure S22g) where the end-tip of CD1 was characterized with the well-fitted density of two alpha helices from L147 to T170 and the end-tip of CD2 was characterized with a flexible loop between two helices which actually corresponded to the missing corner (the red circle area) in the cryo-EM map (Figure S20b). Further rebuilding and refinement of the dataset revealed the structure of HDAC6-CD1-2 (PDB ID: 9K91) (Figure 4a; Table 4-1). The two catalytic domains were closely attached via interaction between three pairs of helices and two pairs of loops in the center region. The catalytic zinc ions of the two domains (CD1 and CD2) were ~48 Å apart with two active-site tunnels, respectively (Figure 4b). A closer view of the active sites of CD1 and CD2 revealed a highly conserved amino acid composition. In the active site of CD1, the Zn^{2+} was bonded to D253, D346, and H255, and the catalytic histidines H215 and

H216 were 4.7 Å and 5.2 Å apart from the Zn^{2+}, respectively (Figure 4c). Whereas, the Zn^{2+} in CD2 was bonded to D649, D742, and H651, and the catalytic histidine H610 and H611 were 4.0 Å and 5.5 Å apart from the Zn^{2+}, respectively (Figure 4d). The morphology of two active sites was constructed by showing the molecular surface of the two active sites which uncovered a CD2-active-site tunnel significantly distinguished from that of CD1. In CD2, the blind tunnel was wide and shallow, where the catalytic Zn^{2+} resided aside at the bottom of the tunnel (Figure 4f). In contrast, the CD1 tunnel was narrow and twisted, where the catalytic Zn^{2+} resided aside near the bottom of the tunnel with Y225 protruding in front of the catalytic Zn^{2+} on the side facing the opening of the tunnel (Figure 4e). Such tunnel morphology suggested a wider substrate selectivity for the CD2-active-site compared to that of CD1. In comparison with the previously determined zebrafish HDAC6-CD1-2, the CD1-active-site tunnel of hHDAC6-CD1-2 was narrow and twisted. While the overall backbone structure of HDAC6-CD1-2 and the conformation of CD2-active-stie was conserved between these two species (Figure S20 d – f; Figure S21). Moreover, no disulfide bond was found within the structure of hHDAC6-CD1-2 after examining the distance between each pair of adjacent cysteines in it (Figure S24).

Formation of the enzyme-substrate complex

Molecular dynamics (MD) simulations with three replicas were performed to obtain the enzyme-substrate (ES) complex. A stable binding between hHDAC6-CD2 and its substrate, Ac-Ser-Asp-Lys (Ac)-AMC, was observed (Figure S25). The root-

mean-square fluctuations (RMSF) of MD simulations were generally consistent with the B-factor in the crystallographic structure (PDB ID: 5EDU), confirming the validity of the MD simulations results (Figure S25h). The substrate was divided into three parts to analyze the root-mean-square deviation (RMSD). The RMSD results indicated that Lys (Ac) and AMC were more stable than Ac-Ser-Asp during the MD simulations (Figure S25c – e). The Zn^{2+} ion was stable with five-fold coordination to D649, H651, D742, substrate, and a water molecular in the ES complex during the MD simulations (Figure S25f and Figure S26). This was consistent with that in the previous density functional theory (DFT) quantum mechanics/molecular mechanics (QM/MM) studies of histone-deacetylase-like protein (HDLP) and HDAC8 (Figure S28a and b) [23,24]. In addition, representative photomicrographs showed co-localization of hHDAC6 and its endogenous substrate, α-tubulin, in HUVECs (Figure S27d and e). MD simulations demonstrated that α-tubulin (acetylated K40), was able to combine steadily with hHDAC6-CD2 (Figure S27a – c). In contrast, CD1 showed no catalytic activity on α-tubulin (acetyl K40) (Figure 3b). This might be ascribed to the obstruction of K353, which prevented acetylated K40 from entering the CD1-active-site (Figure 4e).

H_2S mediated an alternative deacetylation pathway coupled with generation of thioacetic acid

Here we propose an alternative mechanism of deacetylation reaction, which is catalyzed by H_2S-coordinated hHDAC6-CD2 (mechanism A in Figure 5a). Upon optimization of H_2S-coordinated ES structure, H_2S was dissociated into HS^- and H^+.

Meanwhile, H611 served as a general base to accept the dissociated proton. This process was barrier-free and might have occurred simultaneously during the substrate-binding process. The structure of ES - A1 was an HS^--coordinated system with a double-protonated H611 (HID610/HIP611). The Zn^{2+} ion was in four-fold coordination. This is consistent with the ES complex of the canonical reaction catalyzed by H_2O-coordinated zHDAC6 with HID573/HIP574 protonation states (Figure S28c)[25]. There were three elementary reaction steps to catalyze acetylated lysine into deacetylated lysine and thioacetic acid (Figure 5b and c). In the first step, the HS^- anion dissociated into S^{2-} and H^+ through its interaction with H610, which acted as a general base to accept the dissociated proton. Simultaneously, D647 served as a general base to accept a proton from H610. Secondly, the S^{2-} anion acted as a nucleophilic agent to attack the carbonyl C of the acetyl group, forming an S–C bond. Meanwhile, Y782 lent a proton to the oxygen atom of the acetyl group. This step was the rate-limiting step with an energy barrier of 17.3 kcal/mol (Figure 5d) for TS2 - A1, which was constant with the enzyme kinetics (Table 3-2). In the third step, H611 served as a general acid to provide a proton to the nitrogen atom of the lysine residue. This caused cleavage of the C–N bond between the acetyl group accompanied by an increase in C–N distance from 1.48 Å (INT2 - A1) to 2.80 Å (EP - A1). Meanwhile, a proton was transferred back to Y782 from the acetyl group.

The most likely alternative mechanism where HS^- might serve as a nucleophilic agent to attack carbonyl C of the acetyl group was also examined in mechanism A2 (Figure S29). The calculations revealed that an energy barrier of 26.6 kcal/mol was

calculated in mechanism A2. This was a rather high energy barrier as compared to that in mechanism A1, suggesting that mechanism A1 is more kinetically accessible under the studied conditions. Regarding the role of acidity, H_2S is known to possess stronger acidity than H_2O. This distinction in acid strength implies that H_2S and H_2O are likely to exhibit different reactivity patterns in proton-involved transition metal complex reactions. Such a difference in chemical behavior further supports the plausibility of distinct reaction pathways mediated by H_2S and H_2O. Furthermore, nucleophilicity of the species involved should be taken into account. The nucleophilicity of HS^- is lower than that of S^{2-}. This difference in nucleophilicity is a crucial factor that contributes to the distinct reaction pathways and mechanisms observed in current calculations.

Thioacetic acid was hydrolyzed to acetate acid in the active site of hHDAC6-CD2 coupled with recycling of H_2S

The transient product, thioacetic acid, was hydrolyzed into acetic acid and H_2S (mechanism C in Figure 5a and Figure S30)[26]. In the first step, an H_2O molecule generated an OH^- and H^+ where H611 served as a general base to accept an H^+. The OH^- anion initiated a nucleophilic attack on the carbonyl C of thioacetic acid. Secondly, this nucleophilic attack resulted in breaking of the S–C bond. Meanwhile, H610 served as a general base to accept an H^+ to generate acetate ion and HS^-. Subsequently, HS^- formed a coordination bond with Zn^{2+} ion (S–Zn bond length was 2.38 Å) resulting in a recycle of H_2S in H_2S-coordinated active site of hHDAC6-CD2 (Figure 5e2). The energy barrier in this reaction was 7.6 kcal/mol (Figure S30c).

The canonical deacetylation reaction mediated by H_2O

The reaction catalyzed by the H_2O-coordinated hHDAC6-CD2 active-site (mechanism B in Figure 5a) was initiated upon substrate-binding to the zinc-active-site including three elementary reaction steps (Figure S31a and b). In the first step, the H_2O molecule coordinated at active-site Zn^{2+} ion dissociated into OH^- and H^+ upon substrate-binding to the active-site (to Zn^{2+} ion and Y782) and an interaction with H611 serving as a general base. Simultaneously, the OH^- anion initiated a nucleophilic attack on the carbonyl carbon of the acetyl group, which was the rate-limiting step with an energy barrier of 18.2 kcal/mol (Figure S31c) for transition state 1 of mechanism B1 (TS1 - B1). This energy barrier was comparable to that of the enzyme kinetics (Table 3-2) and reported deacetylation reactions catalyzed by HDLP (19.1 kcal/mol)[23], HDAC8 (18.3 kcal/mol)[24] or zebrafish HDAC6 (zHDAC6) (19.3 kcal/mol)[25]. Secondly, H611 served as a general acid to provide a proton to the nitrogen connected to the acetyl group. Finally, H610 served as a general base to accept a proton from the acetic acid, thereby leading the cleavage of the C–N bond between the acetyl group and the lysine residue. Meanwhile, D647 served as a general base to accept a proton from H610, which was also found in the reactions catalyzed by zHDAC6[25]. This process resulted in an increase of the C–N distance from 1.58 Å (INT2 - B1) to 2.90 Å (EP - B1), leading to generation of deacetylated lysine and acetic acid. One water molecule was consumed in this reaction. The energy of the EP complex was 5.6 kcal/mol higher than that of ES. Notably, the EP complex was not its final form in this reaction. The product was

subsequently discharged from enzyme binding pocket. The free energy of the system could be further decreased due to a release in translational and rotational free energy. Such phenomenon is also reported in the reactions catalyzed by HDAC8[27] or the angiotensin converting enzyme (ACE)[28].

Variable protonation states at H610 and H611 in the ES complex were also explored as shown in mechanism B2 (Figure S32). The energy barrier in mechanism B2 was 26.1 kcal/mol. Such an energy barrier was quite high. However, this was comparable to that in the ES complex with HID131/HIP132 protonation in HDLP (25.9 kcal/mol)[23] or that with HID142/HIP143 protonation in HDAC8 (29.9 kcal/mol)[24]. In this context, mechanism B1 (HID610/HID611) is more reasonable as compared to mechanism B2 (HIP610/HID611 or HID610/HIP611). Mechanism B1 agrees with the proton-shuttle reaction mechanism proposed by Zhang and coworkers in the reactions catalyzed by HDLP[23] or HDAC8[24].

Comparison between the alternative deacetylation reaction with H_2S and the canonical reaction with H_2O

Obviously, the key event in these reaction steps was the cleavage of the C–N bond between the acetyl group and the lysine residue. This was achieved by nucleophilic attack on the carbonyl C of the conjugated acetyl group by the S^{2-} or OH^- anion in hHDAC6-CD2 coordinated with H_2S or H_2O, respectively. In H_2S-coordinated pathway, the dissociation of coordinated H_2S readily yielded HS^- through a barrier-free reaction step. This led to the subsequent generation of a more powerful nucleophilic agent S^{2-}.

In deacetylation reactions mediated by S^{2-}, the highest energy barrier corresponding to the rate-limiting step was 17.3 kcal/mol (found in TS2 - A1), demonstrating that H_2S facilitates the reaction by a new S^{2-}-mediated nucleophilic attack mechanism. H_2S was not consumed but recycled by consuming an H_2O. In H_2O-coordinated active sites, OH^- was yielded from the coordinated H_2O where the dissociation of H_2O and the nucleophilic attack on carbonyl C of the conjugated acetyl group occurred simultaneously with the highest energy barrier (TS1 - B1, 18.2 kcal/mol) among these three reaction steps (Figure S31). Obviously, the reaction with H_2S was a more efficient reaction pathway with a lower energy barrier, as compared to the canonical deacetylation pathway. The reduction of the energy barrier was correlated with an elevation in the reaction rate constant k_{cat}, as predicted by transition state theory.

HDAC6 mediates the H_2S effects in promoting migration of vascular endothelial cells

H_2S facilitated wound healing in human umbilical vein endothelial cells (HUVECs) at concentrations ranging from 12-90 μM (Figure S34a and b). A slow-releasing H_2S donor, GYY4137, showed a similar pro-migration effect in HUVECs (Figure S34e and f). Meanwhile, the acetylation level of α-tubulin decreased by ~56.8% with NaHS treatment (60 μM) in HUVECs without affecting HDAC6 expression (Figure 6a; Figure S34c and d).

HDAC6 knockdown induced by shRNA interference (Figure S35a and b) reduced its expression by 74-85 % and blunted the H_2S effects in promoting cell migration as

examined in wound-healing (Figure 6b; Figure S35d) and trans-well assays (Figure 6c; Figure S35c), as well as in cell tube formation (Figure 6e and f) in HUVECs. HDAC6 knockdown itself caused a decrease in cell migration and an inhibition of cell tube formation. Cell migration is driven by depolymerization and rearrangement of cytoskeleton proteins such as α-tubulin and actin filaments. Acetylated α-tubulin was significantly decreased in the cells with control transfection treated with NaHS (60 μM) and this effect was blunted in the cells with HDAC6 knockdown (Figure S36a). In migrating cells with control transfection, the polarized microtubule networks were aligned along with the axis of cell migration, and the consistency of such microtubule arrangement was strengthened by NaHS treatment (60 μM) (Figure S36a). In contrast, the microtubule networks were radially organized and showed no obvious polarization in the cells with HDAC6 knockdown which resulted in a disordered "pancake"-shape cell morphology, where the H_2S effects on microtubule arrangement and cell morphology were blunted (Figure S36a). However, NaHS treatment (60 μM) did not change cellular distribution of HDAC6 nor its co-localization pattern with α-tubulin (Figure S27d and e).

Cortactin is another HDAC6 substrate and acetylation of cortactin reduces the binding ability of F-actin and inhibits cell migration[10]. F-actin and cortactin distribution were examined using confocal microscopic imaging to determine the effects of H_2S on cell morphology related to the distribution of F-actin, though acetylated cortactin was not to shown due to the limitation of the primary antibodies against acetylated cortactin. The HUVECs of the control group showed normal cell morphology, clear polarization,

and a definite direction of movement. Cortactin distribution was seen at the front edge of cell migration and F-actin roughly extended from the front edge to the rear of the cells along the direction of cell migration. NaHS treatment (60 μM) promoted cell polarization and increased F-actin and cortactin colocalization near the leading edge of the cells. While HDAC6 knockdown caused a significant abnormality in cell morphology, resulting in a "pancake"-shape cell with no clear polarization direction, centralized cortactin distribution around the nucleus, and chaotic intracellular distribution of F-actin. Whereas the effects of NaHS treatment (60 μM) in promoting cell polarization were blunted in these cells with HDAC6 knockdown (Figure S36c - e).

In addition, a series of hHDAC6 variants with a single mutation at CD1/CD2-active sites were expressed in the cells knockout of endogenous HDAC6 treated with NaHS (60 μM) or vehicle. Treatment with NaHS promoted cell migration in the cells expressing hHDAC6-H216A, but not in the cells expressing hHDAC6-H611A or hHDAC6-H216/611A (Figure 6f; Figure S37). The data suggested that the H_2S effects in promoting cell migration are blunted in the cells expressing hHDAC6 mutated at its CD2-active-site but not in that mutated at the CD1-active-site.

Immunoprecipitation experiments have revealed a direct interaction between the endogenous hydrogen sulfide-producing enzyme cystathionine gamma-lyase (CSE) and the catalytic domain of HDAC6 (Figure S38a). Knocking out CSE in endothelial cells inhibits wound healing while exogenous administration of NaHS (60 μM) compensated this effect (Figure S38b and c), suggesting a role of CSE/H_2S-HDAC6 in regulating cell migration.

Moreover, the potential role of H_2S in cell autophagy was also examined by measuring some autophagy-related genes including LC3B II/I, p62 and Beclin-1 in serum-starved cells with or without knockout of HDAC6 (Figure S39a - d). H_2S treatment caused a significant decrease in LC3B II/I level, and this effect was blunted in HDAC6 knockout cells (Figure S39a - b).

The role of exogeneous H_2S and CSE on acetylomics in the cells with or without HDAC6

Exogenous administration of NaHS (60 μM) caused downregulation of acetylation at 965 sites in the cells as shown in acetylomics analysis (Figure 6g). In contrast, acetylation at 1,388 sites was upregulated in the cells knocked out of the H_2S generating enzyme, CSE (Figure 6h). Whereas, acetylation at 981 sites was upregulated in the cells knocked out of HDAC6 (Figure 6i). By taking the intersection of these altered sites, 27 acetylation sites distributed across 7 different proteins were identified. These intersectional proteins, including Enabled Actin Regulator (ENAH), Heterogeneous Nuclear Ribonucleoprotein K (HNRNPK), Cortactin (CTTN), Single-Stranded DNA Binding Protein 1 (SSBP1), GTP-binding nuclear protein Ran (RAN), Vimentin (VIM), and Centrin 2 (CETN2) are all closely linked to cell migration (Figure 6j and k). While the expression of these 7 proteins was not changed as shown in proteomics analysis (Figure S40a – c). Furthermore, proteomics analysis also revealed that the expression levels of HDAC6 were unchanged by exogenous administration of NaHS (60 μM) nor knockout CSE (Figure S40a – c). Regardless of the importance of the K40 lysine of

alpha-tubulin as a key downstream substrate regulated by HDAC6, it was not reckoned in above-mentioned intersectional acetylation sites. This might be ascribed to a decrease in the acetylation level of this site to a degree below the detection limit of the mass spectrometer in two of the three samples treated with exogenous H_2S (Figure S40d). In contrast, upregulation in acetylation at the K40 lysine site was conspicuous in the cells knockout of CSE or HDAC6. Further validation using Western blot analysis confirmed that exogenous H_2S treatment indeed downregulated acetylation at this K40 site in alpha-tubulin (Figure S40e and f).

The proangiogenic effect of H_2S is blunted in a disease model of hind-limb ischemia in HDAC6$^{-/-}$ mice

To further clarify the physiological role of HDAC6 in mediating H_2S-induced angiogenesis, the proangiogenic effects of H_2S were examined in both wild type (WT) and HDAC6$^{-/-}$ mice which were created by inserting an adenine after the 706-adenine-site in the mice HDAC6 genome to inactivate expression of HDAC6. Western blot analysis confirmed elimination of HDAC6 expression in both heart and kidney tissues (Figure S41a). The proangiogenic effect of H_2S was evidenced by increased protruding of microvessels and increased hemoglobin content in the Matrigel plugs embedded in wild type mice treated with NaHS at 30 μmol/L/kg/d as compared with that treated with vehicle. In contrast, these proangiogenic effects of H_2S were blunted in HDAC6$^{-/-}$ mice (Figure S41 b and c). To determine whether HDAC6 regulates H_2S-induced angiogenesis in a disease model of ischemic injury, hind-limb ischemia was surgically

induced in both wild type and HDAC6$^{-/-}$ mice. Following hind-limb ischemia injury, the mice were injected with NaHS or saline at 30 μmol/kg/d for 14 days. Blood flow in the ischemic limbs was increased in WT mice with NaHS treatment in 14 days as compared with that of the vehicle-treated group. In contrast, this increase in tissue blood flow was blunted in the HDAC6$^{-/-}$ mice (Figure 6l and m).

Discussion

The PTMs theory reveals the mechanisms underlying protein regulation at post-translational levels, where certain chemical groups are connected to specific amino acid residues via formation of particular covalent bonds. PTMs are usually dependent on specific enzymes to catalyze various chemical modifications. In particular, acetyl[29,30], methyl[31,32], glycosyl chains, or lactic acid[33] are attached to the nitrogen atoms. While the phosphate or glycosyl chains, thiol, and nitro group are attached to the oxygen-, sulfur- and carbon atoms of particular amino acid residues, respectively[34-36]. In contrast, H_2S binds to the copper ions in the active sites of a metalloenzyme where no modification enzymes are required for the formation or cleavage of such a sulfur-copper coordinate bond[2]. Moreover, we found here that H_2S bound to most types of catalytic metal ions in the active site of a series of metalloenzymes centered by zinc, ferrum, calcium, manganese, and copper. The zinc-centered enzymes are the predominant population among the entire metalloenzyme family. Here, the biochemical role of such H_2S binding was extensively investigated in a zinc-centered metalloenzyme, HDAC6. H_2S was found to recognize and bind at the catalytic zinc ion of HDAC6 by interaction

of atom/molecular orbitals. H_2S was also found to increase HDAC6 activity and promote migration and tube formation in human vascular endothelial cells. These effects were modulated via a direct binding of H_2S to its zinc-active-site without any kind of known chemical modifications on the amino acid residues. No modification enzymes are required for such an interaction between H_2S and HDAC6. This does not represent a new type of chemical modification but some alternative mechanisms beyond the current PTMs concept via a direct coordination and regulation on the catalytic zinc ions. Most notably, H_2S identified its target-site by interaction of molecular/atom orbitals instead of matching of molecular structures between H_2S and HDAC6. The current "key-and-lock" theory based on classical Newtonian mechanics falls short in understanding how ligands as tiny as H_2S identify their "receptors". A new view from conceived quantum physiology might help to uncover the mechanisms underlying interaction between tiny bioactive ligands and their "receptors".

Further QC calculations uncovered that an alternative H_2S-mediated nucleophilic attack on the carbonyl carbon (αC) of the acetyl group leading to cleavage of the acetyl group. Such an H_2S-attacked mechanism was more efficient than the canonical deacetylation reaction pathway where an H_2O molecule coordinates at the zinc-active-site dissociated to yield an OH^- anion, and OH^- pursues a nucleophilic attack resulting in cleavage of the acetyl group[20,23-25,37]. The high efficiency of this new-found deacetylation reaction pathway with H_2S was ascribed to a significantly lower energy barrier in the rate-limiting step. While a decrease in energy barrier of the rate-limiting step always facilitates the corresponding chemical reaction according to the transition-

state theory and Arrhenius equation[38]. These QC data are in line with our bench experiments with enzyme kinetics where H_2S treatment significantly increased the activity of HDAC6.

A further question is raised regarding more precise mechanisms underlying the H_2S-mediated reaction, i.e., does S^{2-} or HS^- serve as a nucleophile? In current QC calculations, all transition states and intermediates were successfully found in both reaction pathways mediated by S^{2-} or HS^-. In this context, both pathways are reasonable. However, the energy barrier of the rate-limiting step of the pathway with HS^- was found as high as 26.6 kcal/mol which was contradictory to enzyme kinetics. Indeed, the deacetylation reaction with H_2S has not been reported to date. No literature could be referenced for energy values nor for enzyme kinetics. Bench experiments to measure any transition states or most intermediates remain impossible due to current limitations in methodology. The pathways with S^{2-} had an energy barrier of 17.3 kcal/mol and might be predominant in terms of thermodynamics and enzyme kinetics. In addition, the QC mechanisms underlying generation of the S^{2-} anion via protonation of H610 have also been demonstrated. In realistic reactions, numerous HDAC6 molecules serve as multiple catalytic sites for ongoing deacetylation reactions. It is possible that some enzyme molecules might catalyze reactions via the HS^- pathway in spite of a lower reaction efficiency. Despite the limitation in definitely distinguishing between the pathways with S^{2-} or HS^-, the pathway with H_2S was evidenced by data based on a variety of approaches including biochemical identification of a specific product, thioacetic acid, in cell-free reactions and also in biological samples of cells/organs.

Endogenously generated H_2S in wild type cells seems to be sufficient to bind to the zinc-active-site of HDAC6 to catalyze a deacetylation reaction to yield thioacetic acid. This unique product was generated from the deacetylation reactions with H_2S. On the other hand, HDAC6 might also serve as an enzyme to catalyze thioacetic acid into acetic acid coupled with recycle of H_2S as demonstrated in QC calculation and also in cultured cells with or without HDAC6. H_2S served as a cyclical "micro-modulator" rather than as a reaction substrate for this metalloenzyme. Actually, thioacetic acid has not been identified in any organisms to date. The current study shed some light on identification of thioacetic acid in cells/organs and also the biphasic role of HDAC6 in generating and catalyzing endogenous thioacetic acid. Noticeably, knockout of HDAC6 caused an unexpected increase in cellular thioacetic acid. The data suggest that there might be more unknown pathways to generate endogenous thioacetic acid in addition to the current deacetylation reaction catalyzed by HDAC6 with H_2S. Moreover, HDAC6 might also serve as an enzyme for degradation of endogenous thioacetic acid coupled with generation of H_2S. In this context, thioacetic-acid/HDAC6 might also function as a generator of endogenous H_2S in addition to the established H_2S-generating pathway dependent on CSE, cystathionine beta-Synthase (CBS), and mercaptopyruvate sulfurtransferase (MPST)[39]. Indeed, much future studies are required to clarify the biological role of thioacetic acid.

In the present study, the binding between H_2S and HDAC6 was found to be reversible, being positively correlated to H_2S levels in the range of concentrations relevant to physiology as shown in SPR assays. On the other hand, there was a decline

in binding affinity at very high H_2S concentrations where a decrease in enzyme activity was also observed. This inhibitory effects of H_2S might be ascribed to a decreased binding between the substrate and enzyme as shown in SPR assays. However, the mechanisms underlying such a decrease in substrate binding are not known. H_2S might alter the structure of enzyme active sites at very high concentrations. Indeed, how potential structural alterations might regulate substrate binding and enzyme catalytic activity remains unknown.

Regarding to HDAC6 structure, it contains two active sites[40]. H_2S binding was found at the catalytic zinc ions in both active sites but not at the rest part of the enzyme as shown in SPR assays using recombinant CD1- or CD2 domains of HDAC6. An ion-chelating agent was also used to remove active-site zinc ions and the binding between H_2S and the metalloenzyme were abolished, suggesting that H_2S was bound to zinc ions in the active sites.

In lower life forms such as zebrafish, the complete structure of zebrafish HDAC6 (zHDAC6) has been determined, and comparable catalytic activity is found in both CD1- and CD2-active-sites[20,21]. However, the structure of hHDAC6 (with 57.8 % homology in amino acid sequences against zHDAC6) is much more difficult to determine[20,21]. Christianson and colleagues determined the CD2 structure of hHDAC6 using crystallography[20]. In their study, the whole hHDAC6 protein could not be crystalized and the CD2 domain took up to 6 months to grow a crystal[20]. The difficulties in obtaining protein crystals might be ascribed to some flexible regions contained in hHDAC6. In contrast to zHDAC6, the CD2-active-site is functionally predominant in

hHDAC6 by catalyzing deacetylation of most known substrates such as α-tubulin, cortactin, heat shock protein 90, tau protein, and peroxiredoxin[10,11]. The CD1-active-site of hHDAC6 rarely has a role in deacetylation of the above-mentioned substrates. The real potential substrates for human CD1 remain unknown[41]. hHDAC6 might be a much more complicated evolutionary outcome yielded from its early forms such as zHDAC6. Human CD2 is characterized by an extensive substrate-binding selection feature. Such a CD2 structure might enable hHDAC6 to serve as a hub for a series of intracellular lysine-acetylation-related signaling networks by catalyzing the deacetylation reactions of multiple important cytoplasmic proteins. In the present study, we showed that H_2S targeted human CD2 to increase enzyme activity, facilitate deacetylation of α-tubulin and cortactin, and promote cell migration. This might be ascribed to the dominant role of CD2 in hHDAC6 and thus the H_2S effects on CD2 might be predominant. The function of human CD1 and the potential role of H_2S on CD1 remains unknown. We have determined here the whole structure of hHDAC6 including both CD2 and CD1 in their naïve form using cryo-EM, which provided structural insights into the mechanisms underlying the substrate selectivity feature of CD1 and CD2. In addition, cryo-EM showed that CD2 had a rather flexible structure around its central zinc-active-site tunnel, which might serve as a flexible adaptor for various substrates to bind at enzyme active site for catalyzation. We found here that human CD2 could bind with different substrates, including acetylated lysine, acetylated polypeptides, and full-length acetylated α-tubulin, by adjusting its flexible regions around the active site during enzyme-substrate interaction. However, human CD1 was

too rigid to adapt to any of these substrates. The core zinc-active-sites of human CD2 and CD1 are similar, however their active-site tunnels and the surrounding structures to determine precise substrate-binding are distinguished from each other. These data might help to explain why it is CD2 but not CD1 to catalyze the deacetylation reactions for most known hHDAC6 substrates and functions as one of the hubs for multiple signaling networks in human cells.

In fact, an intrinsic linkage between CSE/H_2S and HDAC6 has been reported in human aortic endothelial cells[42] as well as in disease models including Angiotensin II-induced hypertension[43], high-fat diet-induced hypertension[44] and adjuvant-induced arthritis[45]. These studies suggest a negative feedback regulation of the purported CSE/H_2S-HDAC6 axis. To examine the role of the potential H_2S/CSE-HDAC6 axis, acetylomics were also examined in the cells treated with exogeneous H_2S, knocked-out of CSE, or knocked-out of HDAC6. Intersection of three acetylomics maps yielded from above experimental settings revealed 27 acetylation sites distributed across 7 different proteins, including ENAH, HNRNPK, CTTN, SSBP1, RAN, VIM, and CETN2. Although the linkage between H_2S/CSE-HDAC6 and the above proteins has not been reported to date, all these 7 proteins have been related to cell migration in some models[10,46-55]. The advantage of the LC/MS methods used in acetylomics is to provide a panorama of protein molecules regulated via specific physiological pathways. However, precise roles of these proteins in regulation via the potential H_2S/CSE-HDAC6 system remain to be clarified in future studies. Indeed, the current LC/MS methods also fall short in missing out on some relevant proteins. For instance,

acetylation levels of α-tubulin in two out of three samples were decreased to an extent below the limit of detection, leading intersection analysis of the acetylomics maps infeasible for detection of α-tubulin. Instead, Western blot analysis was applied to reveal regulation of acetylation on α-tubulin via the H_2S/CSE-HDAC6 axis in this case. In addition, proteins related to autophagy were not found in the intersection of these acetylomics maps in the above experimental models where autophagy was not induced. Actually, H_2S really regulated autophagy in a cell autophagy model mediated by HDAC6.

Plasma H_2S levels have been reported to be ranging from 30 - 100 μmol/L in human[56]. Changes in H_2S levels have been reported to be related to several disease statuses, e.g., a decrease in plasma H_2S levels was found in patients suffering from ischemic heart diseases[57]. In this context, fewer HDAC6 molecules might be coordinated with H_2S in the organs of these patients with decreased endogenous H_2S levels, probably leading to reduced HDAC6 activity and subsequent functional outcomes. HDAC6 might also serve as a senser for endogenous H_2S levels which might fluctuate in various disease status[17-19]. Future studies are required to examine the role of such H_2S regulation on HDAC6 in human diseases. Here we also found that H_2S treatment promoted angiogenesis in a mouse model of hindlimb ischemia and this effect was blunted in HDAC6$^{-/-}$ mice. The data revealed an H_2S-HDAC6 pathway to promote angiogenesis in a disease model combined with ischemia, oxidative stress and inflammatory response.

HDAC6 has been proposed as a drug target and its inhibitors have been developed

to treat malignant and chronic diseases[58-60]. The tandem hHDAC6 structure determined in the present study might also provide some structural insights for the design of new HDAC6 inhibitors. Indeed, the resolution of our current structural determination using cryo-EM is lower than that of the CD2 domain determined by Christianson and colleagues using X-ray crystallography[20]. Actually, it has been found too difficult to crystallize the protein of complete hHDAC6[20]. The scope of molecular weight applicable for cryo-EM determination is beyond 50 kD[61]. While the resolution in cryo-EM is limited in determining low molecular weight proteins due to ambiguous signal-to-noise ratio[62]. The molecular weight of recombinant tandem hHDAC6-CD1-2 is 84 kD, being close to the limit for cryo-EM determination. On the other hand, an increase in molecular flexibility also causes a decrease in cryo-EM resolution[63]. Actually, we obtained a resolution of 3.2 Å in some rigid region in hHDAC6-CD1-2. In contrast, the most flexible region was not visible in cryo-EM.

Taken together, we propose here a mechanism beyond the current PTMs concept to regulate the function of a protein, i.e., a tiny gas molecule, H_2S, coordinates at the zinc-active-site of hHDAC6 by interaction of atom/molecular orbitals to activate enzyme activity via an alternative H_2Smodulated deacetylation pathway coupled with generation of a novel chemical thioacetic acide. The determined tandem hHDAC6 structure also provides some insights into the structural basis underlying distinguished catalytic function between CD1 and CD2, the latter serves as a target site for H_2S to regulate acetylation levels of a series of CD2 substrates and promote cell migration.

To prospect, the current study proposes a hypothesis that H_2S might potentially

target most kinds of catalytic metal ions including zinc, ferrum, magnesium, or calcium in the active sites of the huge metalloenzyme family which account for about one-third of exceeding 6000 enzymes found in biology and medicine[3-6]. Indeed, each individual metalloenzymes might catalyze respective reactions with unique mechanisms, based on which H_2S might directly bind and regulate the metal active sites. H_2S might carry out regulation with diversified mechanisms, including to mediate some new chemical reaction pathways as found in the current HDAC6 study, rearrangement of the electrostatic force-arrays around the copper active site of Cu/Zn-SOD[2] (a diffusion-limited enzyme), or a possible regulation on the structure of the metal-centered active sites in numerous metalloenzymes. In particular, some of the metalloenzymes targeted by H_2S are key regulators in protein modifications and epigenetics, where the H_2S effects might be amplified, integrated, inherited and versified. Such a direct H_2S-targeting on the metal active sites might unseal a deeper layer of regulation on intracellular signaling networks as illustrated in the schematic diagram. In other words, numerous metalloenzymes might serve as a senser-network for endogenous H_2S with their catalytic metal ions as perceptional mechanisms (Figure S42).

Figures and Figure legends

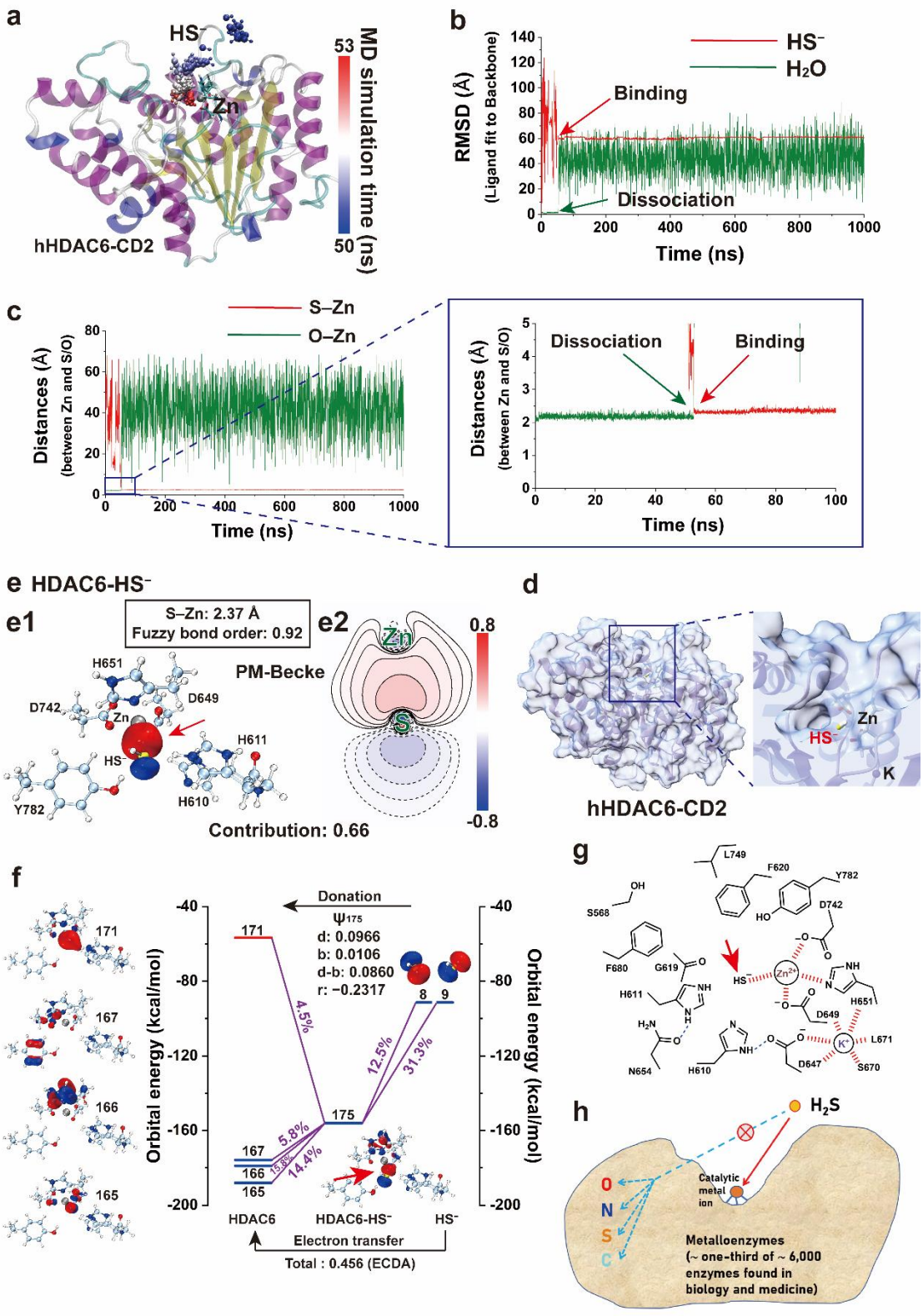


Figure 1. HS^- diffused to the catalytic zinc ions in the active site of HDAC6-CD2 inspiring potential interaction between HS^- and the catalytic metal ions in multiple members of the metalloenzyme family. a, Spontaneous diffusion of HS^- through the active-site tunnel of hHDAC6-CD2 to bind with the catalytic Zn^{2+} ion at the bottom of the tunnel from 50 ns to 53 ns. Purple, α-helix; yellow, β-sheet; white, coil; cyan, turn; blue, 3-10 helix. **b**, Root-mean-square deviation (RMSD) of coordinated HS^- (red) or H_2O (green) fit to the hHDAC6-CD2 backbone in molecular dynamics (MD) simulations lasted for 1000 ns. Binding of HS^- was coupled with dissociation of H_2O occurred at 53 ns of the MD simulations. c, S–Zn distance (red) and O–Zn distance (green) over the MD simulation period of 1000 ns. Binding with HS^- (red arrow) was coupled with dissociation (green arrow) of H_2O. **d**, A snapshot of the last frame of the MD simulations showing an HS^- bound at the active site of hHDAC6-CD2. **e**, Isosurface maps (isovalue = 0.05 a.u.) (**e1**) and contour maps (**e2**) of localized molecular orbitals (LMO) of the HDAC6-CD2 active site coordinated with HS^-. Structures were optimized at ε = 4/TPSSh-D3(BJ)/6-31G(d,p)|6-311+G(d,p)|SDD level. Fuzzy bond order (in Becke space) and LMO (Pipek-Mezey algorism with Becke population) were calculated at ε = 4/PBE0-D3(BJ)/6-311+G(2d,2p)|SDD level. Using orbital occupancy-perturbed bond order analysis, contribution of specific LMO to the bond order of the Zn–S bonds was given at the bottom of individual LMO maps. Red and blue regions respectively denoted the positive and negative orbital phases. **f**, Charge decomposition analysis (CDA) and orbital interaction diagram of HDAC6-CD2 active site coordinated with an HS^-. Orbital compositions were calculated using the Mulliken

method at ε = 4/PBE0-D3(BJ)/def2-TZVP|SDD level. Blue and red horizontal lines represented occupied (blue) and unoccupied (red) molecular orbitals (MOs) numbered according to the grades of energy levels of MOs of involved molecules. In isosurface maps (isovalue = 0.02 a.u.) of MOs of the corresponding energy levels, red and blue regions respectively denoted the positive and negative orbital phases. Purple lines/texts indicated the particular contribution of each fragment MOs to the major complex MOs of the S–Zn bond. The number of electrons donated, the number of electrons back donated, and the number of electrons involved in repulsive polarization were expressed as d, b, and r upon binding between HS^- and HDAC6-CD2. Net electrons transfer calculated using extended CDA (ECDA) method was 0.456. **g**, Schematic illustration of the active site of HDAC6-CD2 coordinated with an HS^- (red arrow). **h**, Schematic illustration showing that H_2S might bind at the catalytic metal ions in numerous members of the metalloenzyme family without inducing any forms of post-translational modifications (PTMs) which always occur at four kinds of atoms contained in particular amino acid residues, i.e., O, N, S and C.

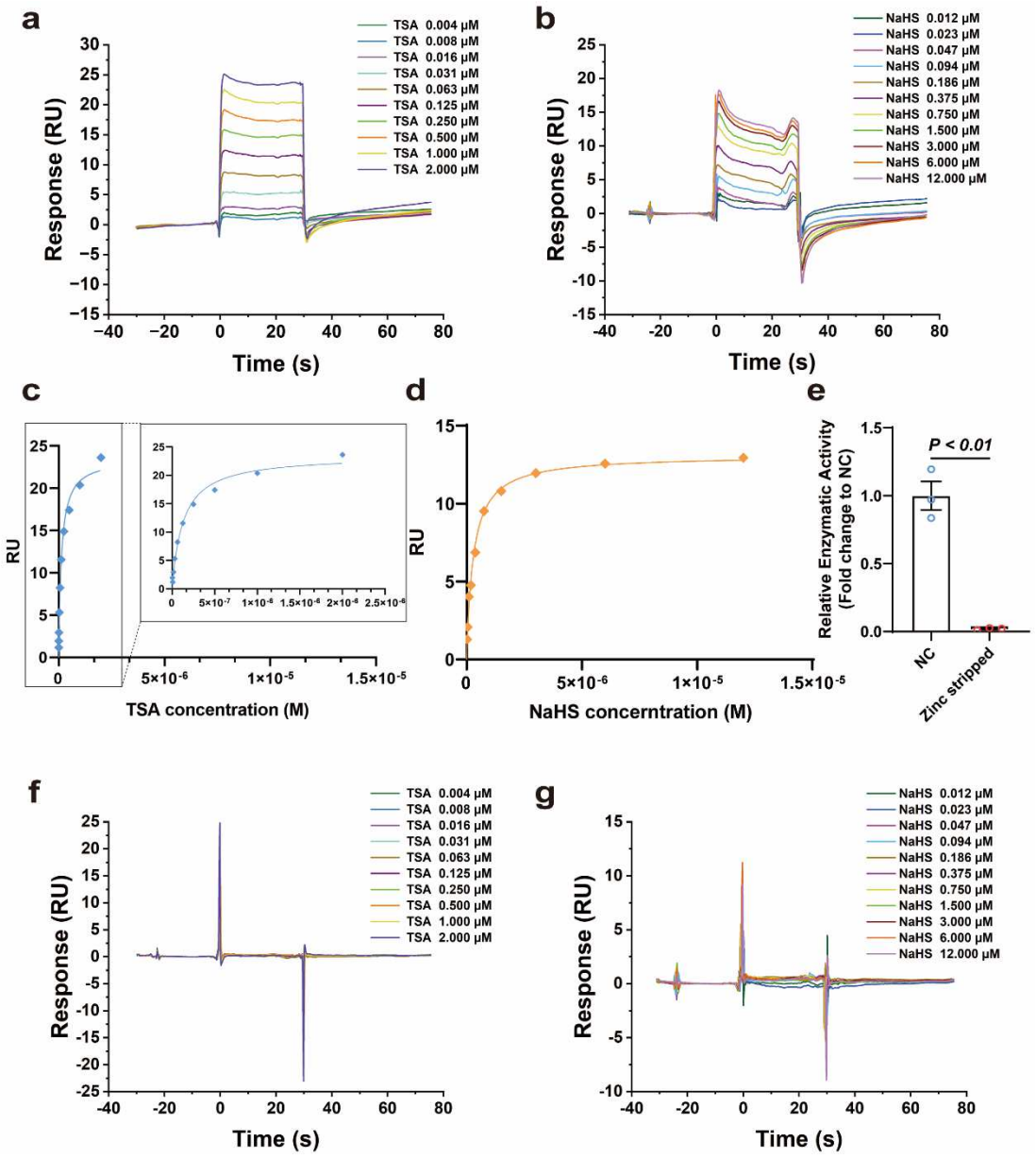


Figure 2. H_2S bound directly to the catalytic zinc ion in the active site of hHDAC6.

a-d, SPR sensorgram showing the kinetic analysis of TSA and NaHS binding to hHDAC6-CD1-2 protein, and the corresponding disassociation coefficient (Kd) fitting plot. **e**, The enzyme activity of Zinc-stripped hHDAC6-CD1-2 was assayed using a fluorogenic substrate derived from α-tubulin. **f-g**, SPR sensorgram showing the kinetic analysis of TSA and NaHS binding to the Zinc-stripped hHDAC6-CD1-2 protein.

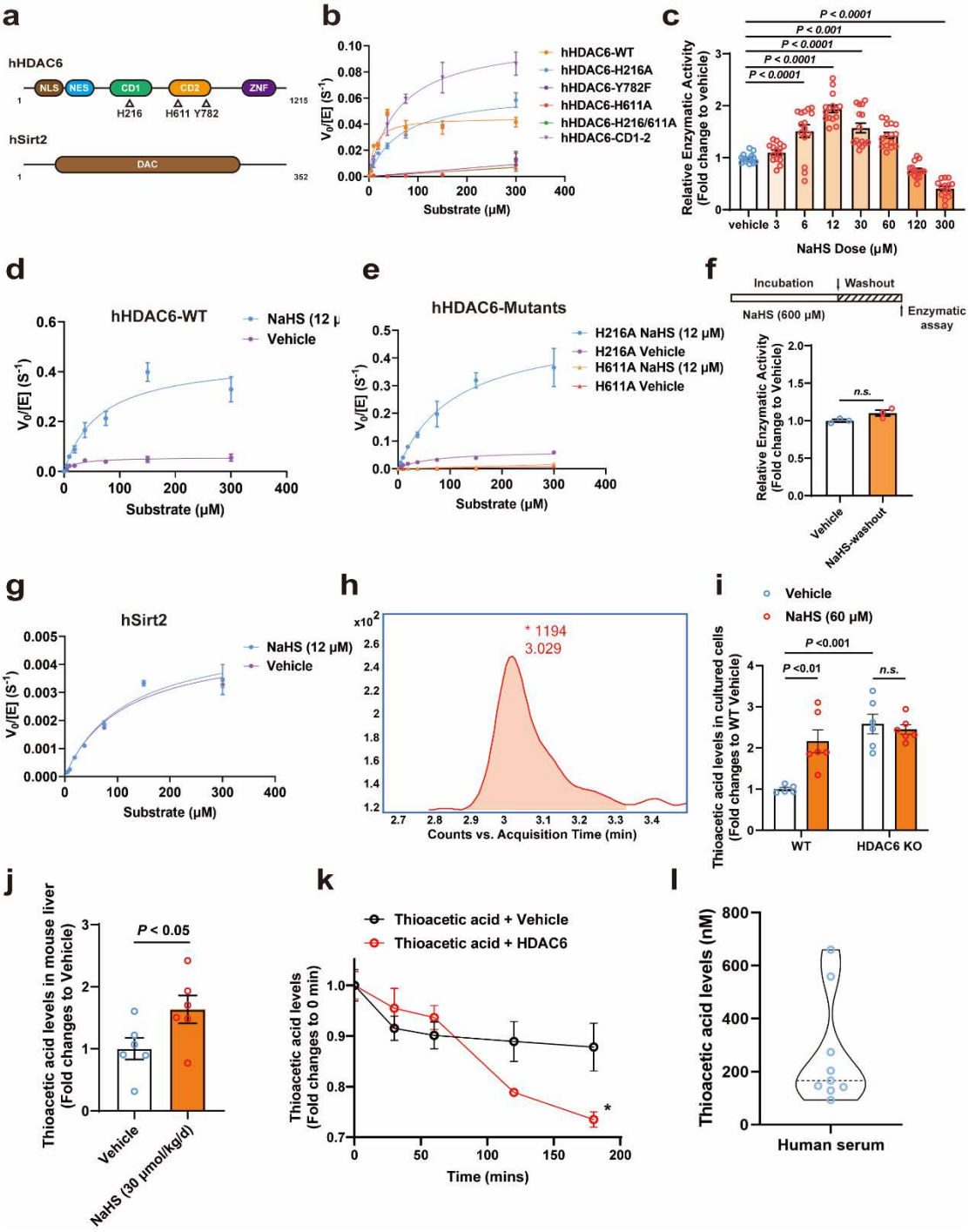


Figure 3. H_2S-induced increase in enzymatic activity of hHDAC6 was dependent on the CD2-active-site via an alternative deacetylation reaction pathway coupled with generation of thioacetic acid. **a**, Domain composition of hHDAC6 and hSirt2. NLS, nuclear localization signal; NES, nuclear export signal; CD1, the catalytic domain

1 of hHDAC6; CD2, the catalytic domain 2 of hHDAC6; ZNF, zinc-finger ubiquitin-binding domain. Approximate positions of residues subject to mutagenesis in hHDAC6 constructs are indicated underneath the domain cartoons. **b**, Steady-state kinetics showing the effects of H_2S on recombinant hHDAC6 constructs with mutations at a series of amino acid residues essential for the either active sites of CD1 or CD2 as assayed with a fluorogenic substrate derived from α-tubulin, n = 3; **c**, Dose-response relationship of NaHS treatment on enzyme activity of hHDAC6-WT, n = 15; **d**-**e**, Steady-state kinetics showing the effects of H_2S on recombinant hHDAC6-WT and hHDAC6 constructs with mutations at either the CD1 or CD2-active-sites as assayed with fluorogenic substrate derived from α-tubulin and 12 μM NaHS, n = 3-4, **f**, The enzyme activity of hHDAC6-CD1-2 protein assayed using a fluorogenic substrate derived from α-tubulin following a washout from a previous NaHS treatment at 600 μM. n = 3. **g**, Steady-state kinetics of NaHS treatment (12 μM) on the enzyme activity of human Sirt2 constructs as assayed with a fluorogenic substrate derived from p53. n = 3. **h**, UHPLC-qqq-MS analysis of the derivatized thioacetic acid products yielded from the enzymatic assay administrated with 12 μM NaHS. **i**, Effects of NaHS administration (60 μM) on the thioacetic acid levels in cultured WT and HDAC6 KO 293T cells, n = 5-6. **j**, Effects of NaHS administration (30 μmol/kg/d) on the thioacetic acid levels in mouse liver tissue, n = 6. **k**, Effects of HDAC6 on the degradation of thioacetic acid, n = 3. **i**, The thioacetic acid levels in heathy human serum, n = 9. UHPLC-qqq-MS, ultra-high performance liquid chromatography-tandem triple quadrupole mass spectrometry.

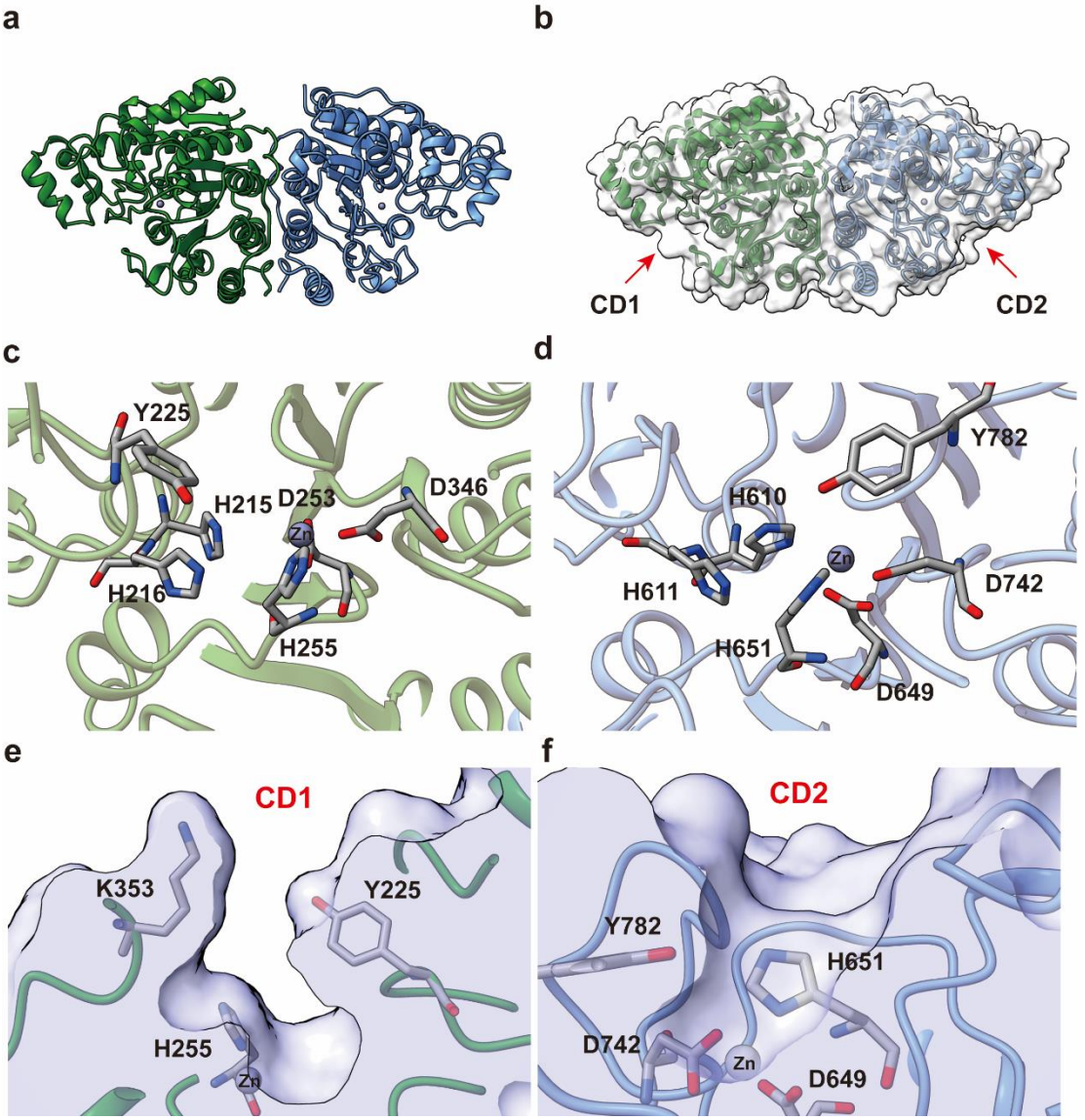


Figure 4. The tandem structure of hHDAC6 containing CD1 and CD2 (hHDAC6-CD1-2). **a**, Cartoon representation of the hHDAC6-CD1-2 structure, showing CD1 in green and CD2 in blue. **b**, Cartoon representation of hHDAC6-CD1-2 structure surface with red arrows indicating the opening of the active-site tunnels. **c** and **d**, Close-up view of the active-site conformation of CD1 (**c**) and CD2 (**d**). **e** and **f**, Molecular surface of the active-site tunnels of CD1 (**e**) and CD2 (**f**).

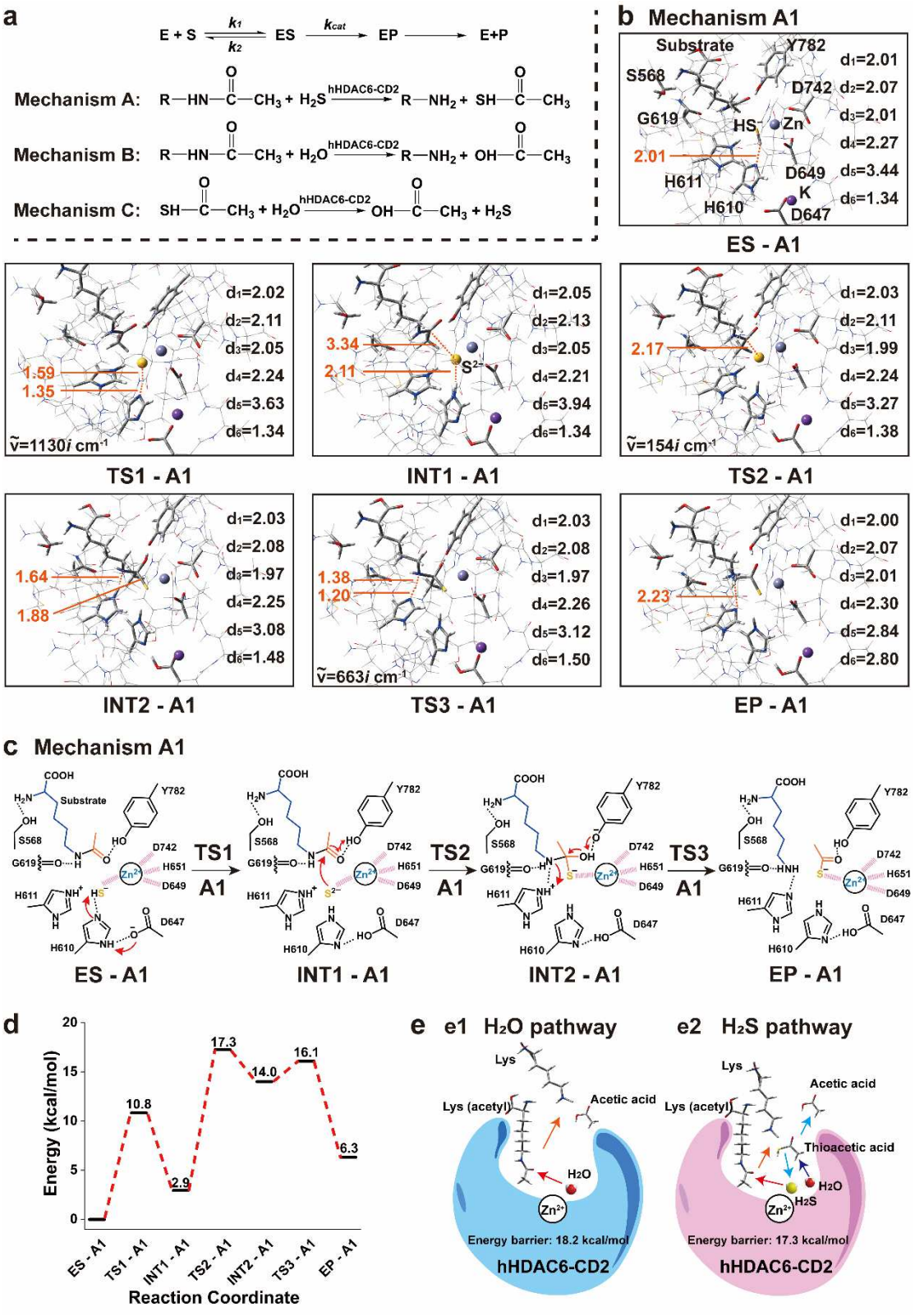

a
E + S
ES
EP
E+P
Mechanism A:
Mechanism B:
Mechanism C:
hHDAC6-CD2
b Mechanism A1
Substrate
Y782
S568
D742
G619
HS
Zn
H611
D649
K
H610
D647
ES - A1
TS1 - A1
INT1 - A1
TS2 - A1
INT2 - A1
TS3 - A1
EP - A1
c Mechanism A1
TS1
TS2
TS3
d
Energy (kcal/mol)
Reaction Coordinate
e e1 H2O pathway
e2 H2S pathway
Lys
Lys (acetyl)
Acetic acid
Thioacetic acid
Energy barrier: 18.2 kcal/mol
Energy barrier: 17.3 kcal/mol
hHDAC6-CD2

Figure 5. Quantum chemical calculations of alternative S^{2-}-mediated deacetylation reactions coupled with generation of thioacetic acid (mechanism A1). **a**, General equations of the enzyme-catalyzed reactions and three proposed mechanisms reactions catalyzed by hHDAC6-CD2 active-site (mechanism A, B and C). E, enzyme; S, substrate; P, product; *K*, the reaction rate constant. **b**, XO2 (ε = 4/B3LYP-D3(BJ)/6-31G(d,p)|6-311+G(d,p)|SDD:PM6-D3) optimized structures of ES, TSs, INTs, and EP in mechanism A1. d_1: distance between Zn^{2+} and D649; d_2: distance between Zn^{2+} and H651; d_3: distance between Zn^{2+} and D742; d_4: distance between Zn^{2+} and the S atom of the coordinated HS^-; d_5: distance between Zn^{2+} and the O atom of the acetyl group of the substrate; d_6: the amide bond of the substrate. Atom distances were given in Å. One imaginary frequency of every TS was given at the bottom left in the corresponding panels. **c**, Mechanism scheme of mechanism A1. The arrows indicate the directions of electron transfer. The dotted lines represent hydrogen bonds. The pink dashed lines represent coordination bonds. **d**, XO2 (ε = 4/MN15/def2-TZVP|SDD:PM6-D3) relative electronic energy profile for mechanism A1. **e**, Schematic illustrations of the deacetylation reactions catalyzed by hHDAC6-CD2 with its active site coordinated with H_2O (**e1**) or H_2S (**e2**), respectively. ES, enzyme-substrate complex; TS, transition state; INT, intermediate; EP, enzyme-product complex.

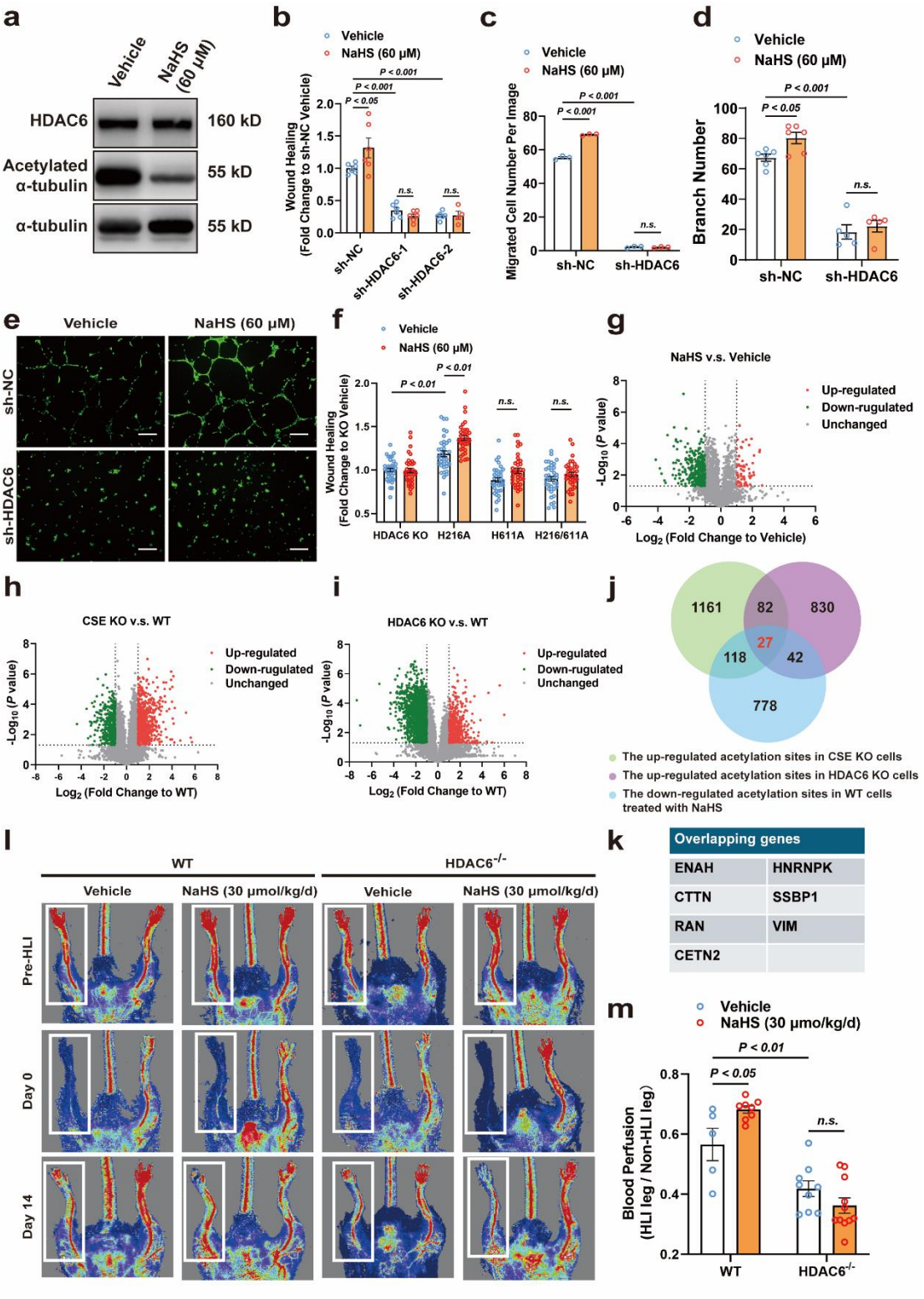

a
Vehicle
NaHS (60 μM)
HDAC6
160 kD
Acetylated α-tubulin
55 kD
α-tubulin
55 kD
b
Vehicle
NaHS (60 μM)
Wound Healing (Fold Change to sh-NC Vehicle)
sh-NC
sh-HDAC6-1
sh-HDAC6-2
c
Migrated Cell Number Per Image
sh-NC
sh-HDAC6
d
Branch Number
sh-NC
sh-HDAC6
e
Vehicle
NaHS (60 μM)
sh-NC
sh-HDAC6
f
Wound Healing (Fold Change to KO Vehicle)
HDAC6 KO
H216A
H611A
H216/611A
g
NaHS v.s. Vehicle
Up-regulated
Down-rugulated
Unchanged
-Log10 (P value)
Log2 (Fold Change to Vehicle)
h
CSE KO v.s. WT
Up-regulated
Down-rugulated
Unchanged
Log2 (Fold Change to WT)
i
HDAC6 KO v.s. WT
Up-regulated
Down-rugulated
Unchanged
Log2 (Fold Change to WT)
j
1161
82
830
27
118
42
778
The up-regulated acetylation sites in CSE KO cells
The up-regulated acetylation sites in HDAC6 KO cells
The down-regulated acetylation sites in WT cells treated with NaHS
k
Overlapping genes
ENAH
HNRNPK
CTTN
SSBP1
RAN
VIM
CETN2
l
WT
HDAC6-/-
Vehicle
NaHS (30 μmol/kg/d)
Pre-HLI
Day 0
Day 14
m
Vehicle
NaHS (30 μmo/kg/d)
Blood Perfusion (HLI leg / Non-HLI leg)
WT
HDAC6-/-

Figure 6. HDAC6 mediated the H_2S effects in promoting migration of vascular endothelial cells and angiogenesis in both *in vitro* and *in vivo* models. a, Representative western blot image showing the acetylation of α-tubulin and HDAC6 in HUVECs treated with NaHS at 60 μM. **b**, Effects of NaHS treatment (60 μM) on wound healing of HUVECs infected with sh-NC, sh-HDAC6-1, or sh-HDAC6-2 lentivirus, n = 6. **c**, Effects of NaHS treatment (60 μM) on the migration of HUVECs in a transwell model with or without knockdown of HDAC6, n = 3. **d** and **e**, Effects of NaHS treatment (60 μM) on the tube formation of HUVECs cultured on a matrigel matrix, bar = 100 μm, n = 5-6. **f**, Effects of NaHS treatment (60 μM) on wound healing of the HDAC6 knockout EA.hy 926 endothelial cells overexpressed with either CD1 active-stie mutated HDAC6 (H216A), CD2 active-stie mutated HDAC6 (H611A) or CD1 and CD2 mutated HDAC6 (H216/611A), n = 36. **g**, Volcano plot of acetylomic analysis of the EA.hy 926 cells treated with NaHS (60 μM), n = 3. **h**, Volcano plot of acetylomic analysis of the EA.hy 926 cells knocked out of CSE. n = 3. **i**, Volcano plot of acetylomic analysis of the EA.hy 926 cells knocked out of HDAC6. n = 3. **j**, Venn diagram demonstrating the intersection of three maps representing differentially regulated acetylated sites. The intersection (red) of these three maps contained 27 acetylation sites. **k**, List of 7 genes being ascribed to 27 regulated lysine acetylation sites in the intersection map shown in **j**. **l** and **m**, On day 0 and day 14 after hindlimb ischemia, blood flow was evaluated using laser Doppler imaging and quantified for each animal as a ratio of the values of the injured to the contralateral uninjured limbs. Representative images (**l**) and bar graphs (**m**) show that blood flow was significantly increased in

injured limbs in wild type mice treated with NaHS at 30 μmol/kg/d for 14 days as compared with that of vehicle-treated mice. This effect was blunted in HDAC6$^{-/-}$ mice, n = 5 - 11. sh-NC, short hairpin RNA negative control.

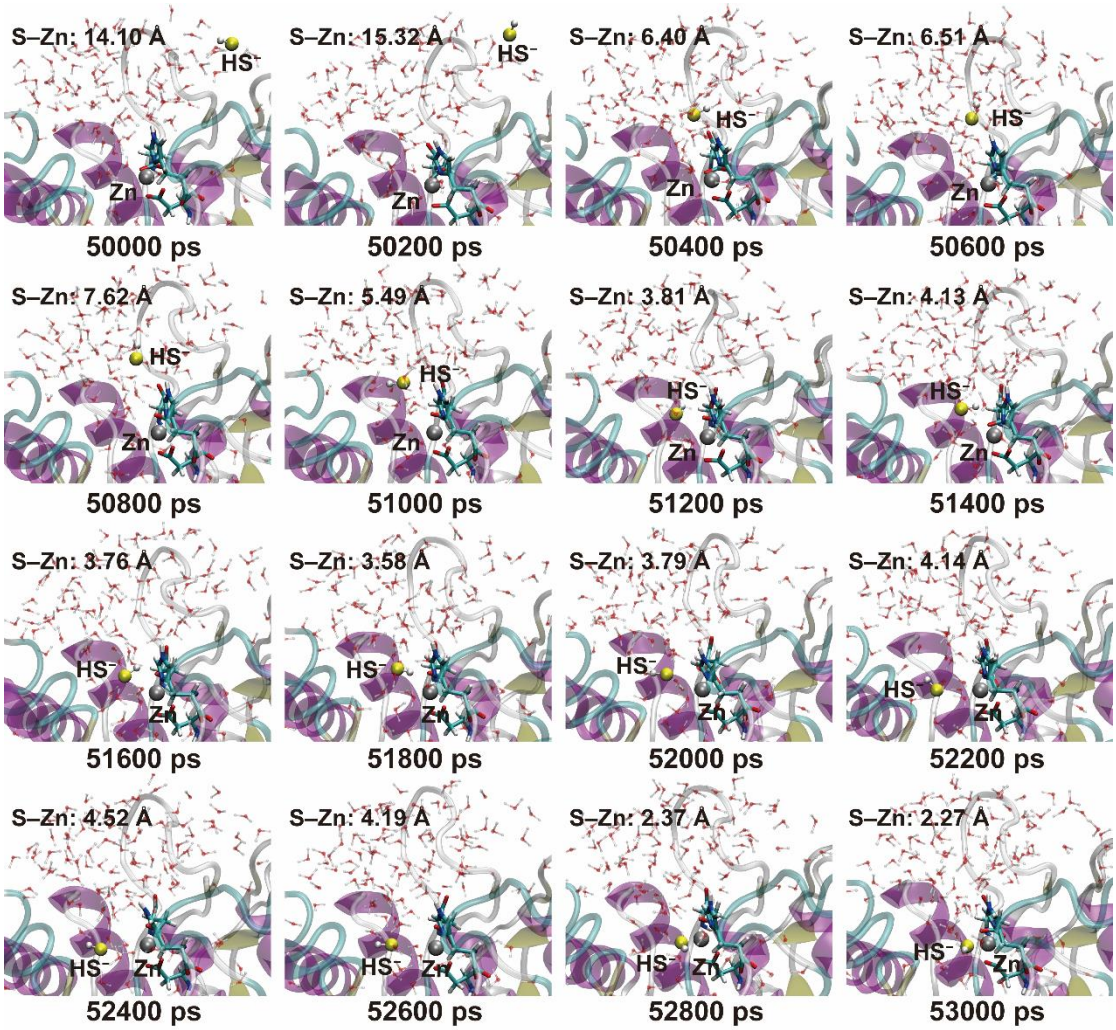


Figure S1 (for Figure 1a–d). Snapshots of the route of HS^- diffusion into the active site tunnel in hHDAC6-CD2 from 50000 ps to 53000 ps in molecular dynamics (MD) simulations. S–Zn distance was shown on the top-left in each snapshot. Purple, α-helix; yellow, β-sheet; white, coil; cyan, turn; blue, 3-10 helix.

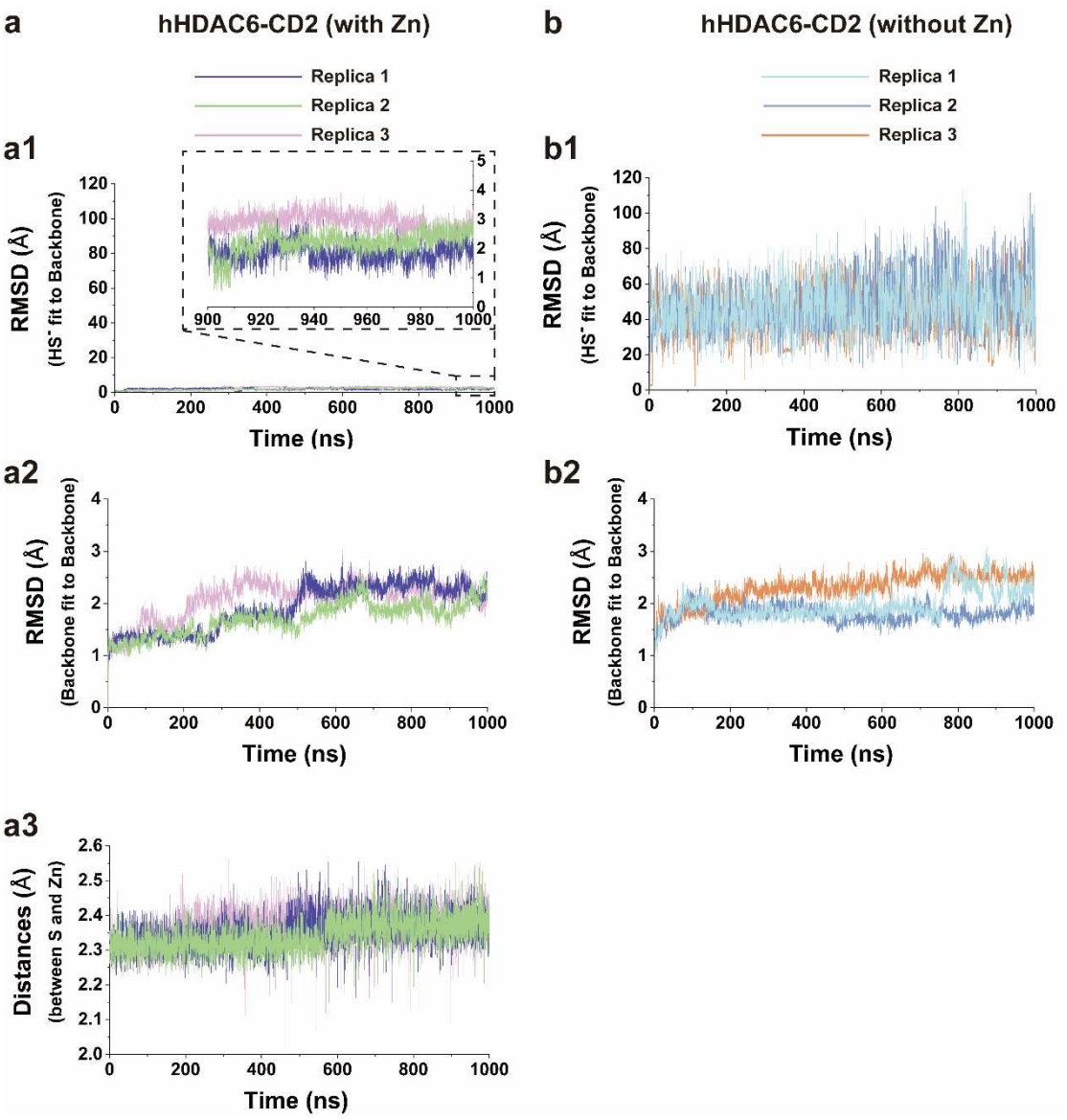
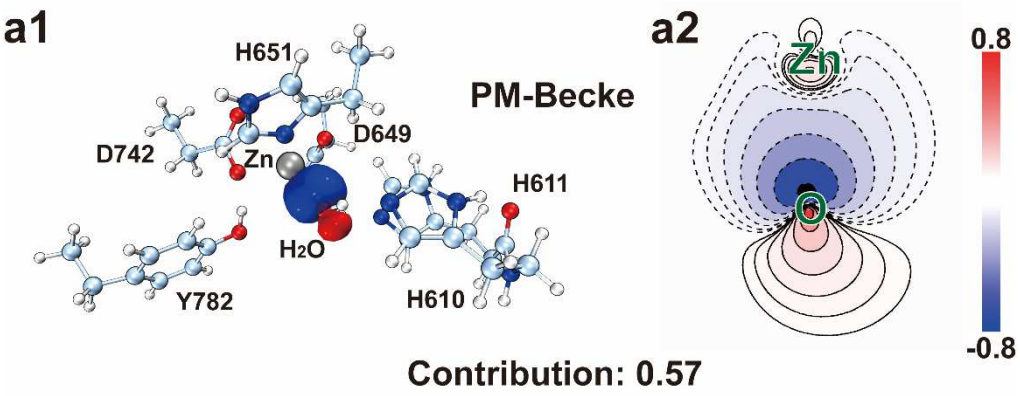

a
hHDAC6-CD2 (with Zn)
b
hHDAC6-CD2 (without Zn)
Replica 1
Replica 2
Replica 3
a1
b1
RMSD (Å)
(HS- fit to Backbone)
Time (ns)
a2
b2
(Backbone fit to Backbone)
a3
Distances (Å)
(between S and Zn)

Figure S2 (for Figure 1a–d). The binding between HS^- and hHDAC6-CD2 was dependent on the catalytic Zn^{2+} ion demonstrated using molecular dynamics (MD) simulations. a1, Root-mean-square deviation (RMSD) values kept converged within a narrow range of < 4 Å in MD simulations of HS^- bound with hHDAC6-CD2 till the end of 1000-ns simulations. **a2**, RMSD of backbone fit to backbone in hHDAC6-CD2 over the simulation period of 1000 ns. **a3**, S–Zn distance remained within the range of < 2.6 Å over the simulation period of 1000 ns. **b1**, Discrete RMSD values oscillating in a range of ~110 Å during 1000-ns MD simulations of interaction between HS^- and hHDAC6-CD2 abolished of catalytic Zn^{2+} ion. **b2**, RMSD of backbone fit to backbone in hHDAC6-CD2 abolished of catalytic Zn^{2+} ion over the simulation period of 1000 ns.

a HDAC6-H_2O

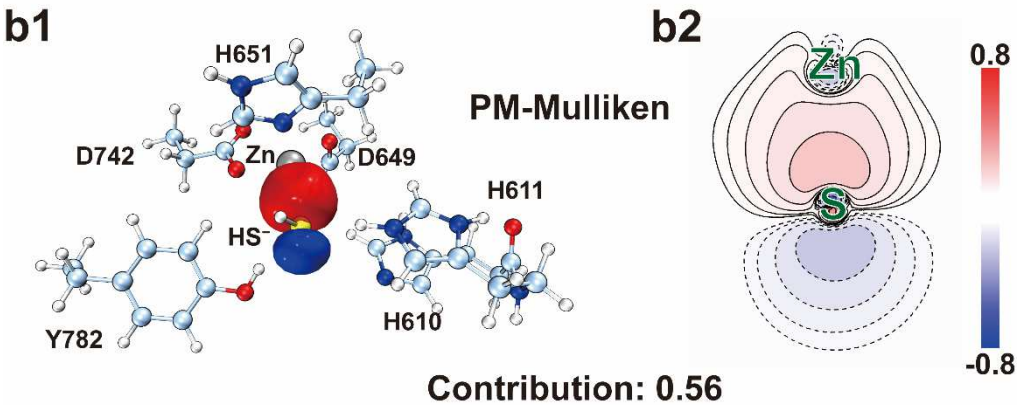
O–Zn: 2.05 Å
Fuzzy bond order: 0.83



Contribution: 0.57

b HDAC6-HS^-

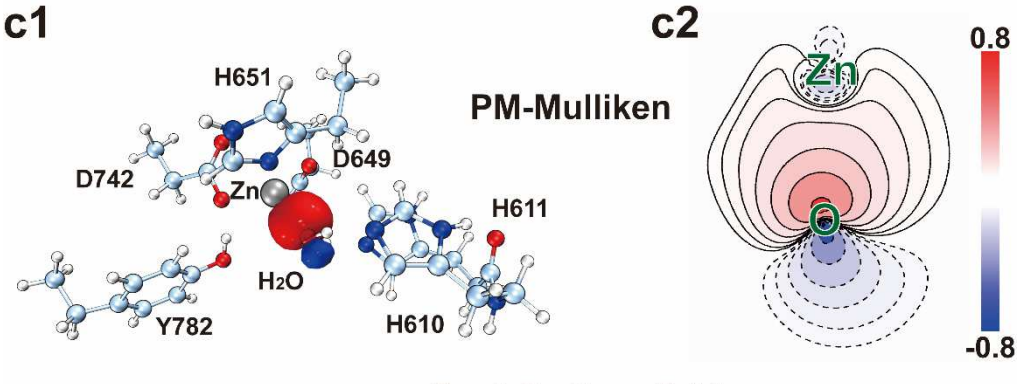
Mayer bond order: 0.63



Contribution: 0.56

c HDAC6-H_2O

Mayer bond order: 0.56



Contribution: 0.41

1

Figure S3 (for Figure 1e). Isosurface maps (a1, b1 and c1; isovalue = 0.05) and contour maps (a2, b2 and c2) of localized molecular orbitals (LMO) of hHDAC6-CD2 active site coordinated with HS^- or H_2O. a1 and **a2**, Fuzzy bond order (in Becke space) and LMO (Pipek-Mezey algorism with Becke population) of O–Zn bond in HDAC6-CD2 coordinated with an H_2O were calculated at ε = 4/PBE0-D3(BJ)/6-311+G(2d,2p)|SDD level. **b1-c2**, Mayer bond order (in Hilbert space) and LMO (Pipek-Mezey algorism with Mulliken population) S–Zn bond (**b1** and **b2**) or O–Zn bond (**c1** and **c2**) in HDAC6-CD2 active site coordinated with HS^- or H_2O were calculated at ε = 4/PBE0-D3(BJ)/def2-SVP|SDD level. Using orbital occupancy-perturbed bond order analysis, contribution of specific LMO to the bond order of S–Zn or O–Zn bonds was given at the bottom of individual LMO maps. Red and blue regions respectively denoted the positive and negative orbital phases.

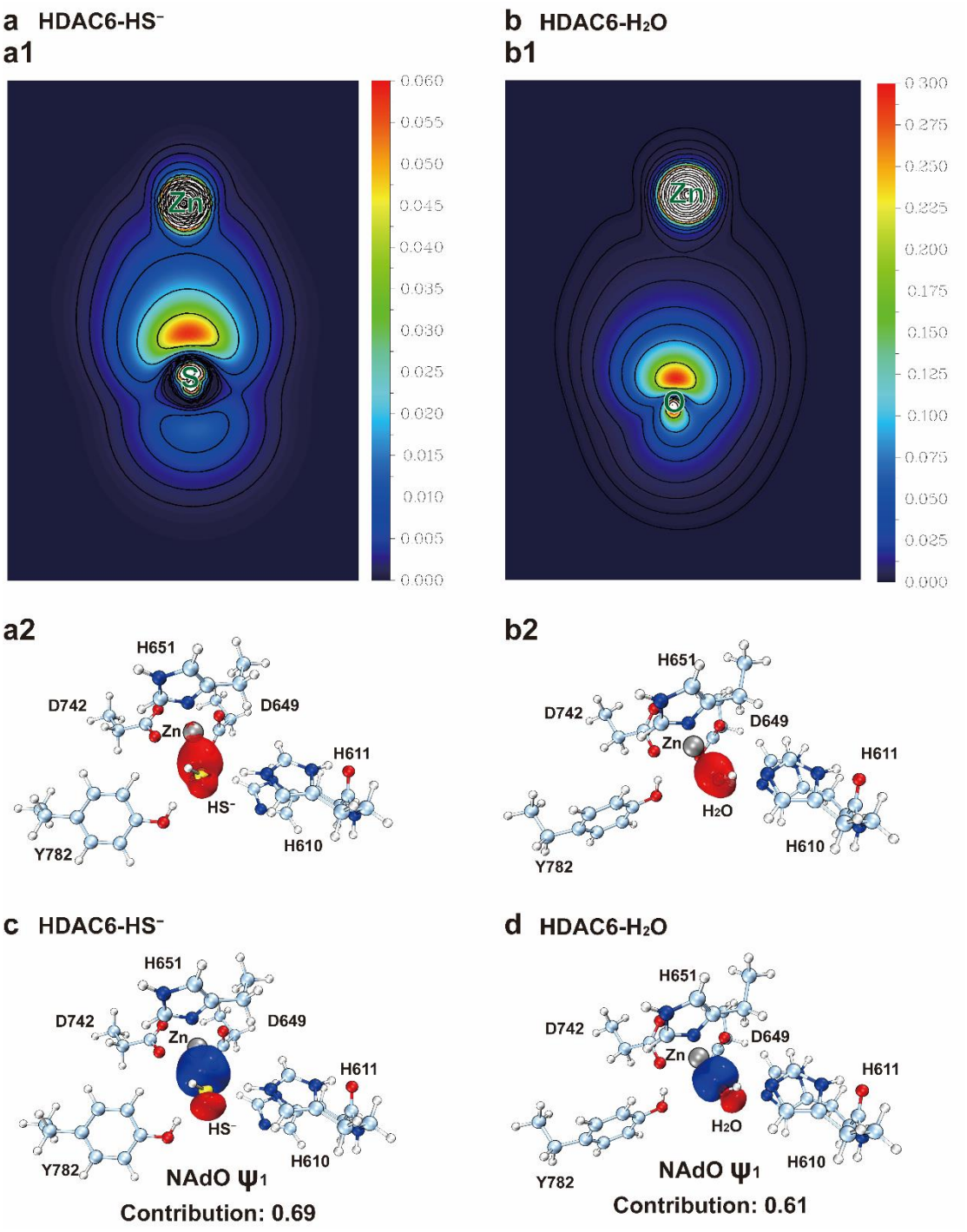

a HDAC6-HS⁻
a1
0.060
0.055
0.050
0.045
0.040
0.035
0.030
0.025
0.020
0.015
0.010
0.005
0.000
Zn
S
b HDAC6-H₂O
b1
0.300
0.275
0.250
0.225
0.200
0.175
0.150
0.125
0.100
0.075
0.050
0.025
0.000
Zn
O
a2
H651
D742
D649
Zn
H611
HS⁻
H610
Y782
b2
H651
D742
D649
Zn
H611
H₂O
H610
Y782
c HDAC6-HS⁻
H651
D742
D649
Zn
H611
HS⁻
H610
Y782
NAdO Ψ1
Contribution: 0.69
d HDAC6-H₂O
H651
D742
D649
Zn
H611
H₂O
H610
Y782
NAdO Ψ1
Contribution: 0.61

Figure S4 (for Figure 1e). Bond order density (BOD) and natural adaptive orbitals (NAdOs) analysis of the hHDAC6-CD2 active site coordinated with HS^- or H_2O. Becke's atomic spaces were used to calculate at ε = 4/PBE0-D3(BJ)/6-311+G(2d,2p)|SDD level. **a1** and **b1**, Contour maps of BOD in HDAC6-CD2 active site coordinated with HS^- (**a1**) or H_2O (**b1**). **a2** and **b2**, Isosurface maps (isovalue = 0.005 a.u.) of BOD in HDAC6-CD2 active site coordinated with HS^- (**a2**) or H_2O (**b2**). **c** and **d**, Isosurface maps (isovalue = 0.05 a.u.) of NAdO in HDAC6-CD2 active site coordinated with HS^- (**c**) or H_2O (**d**). The NAdO eigenvalues respectively denoted the contribution of NAdOs to the fuzzy bond order of S–Zn and O–Zn bonds.

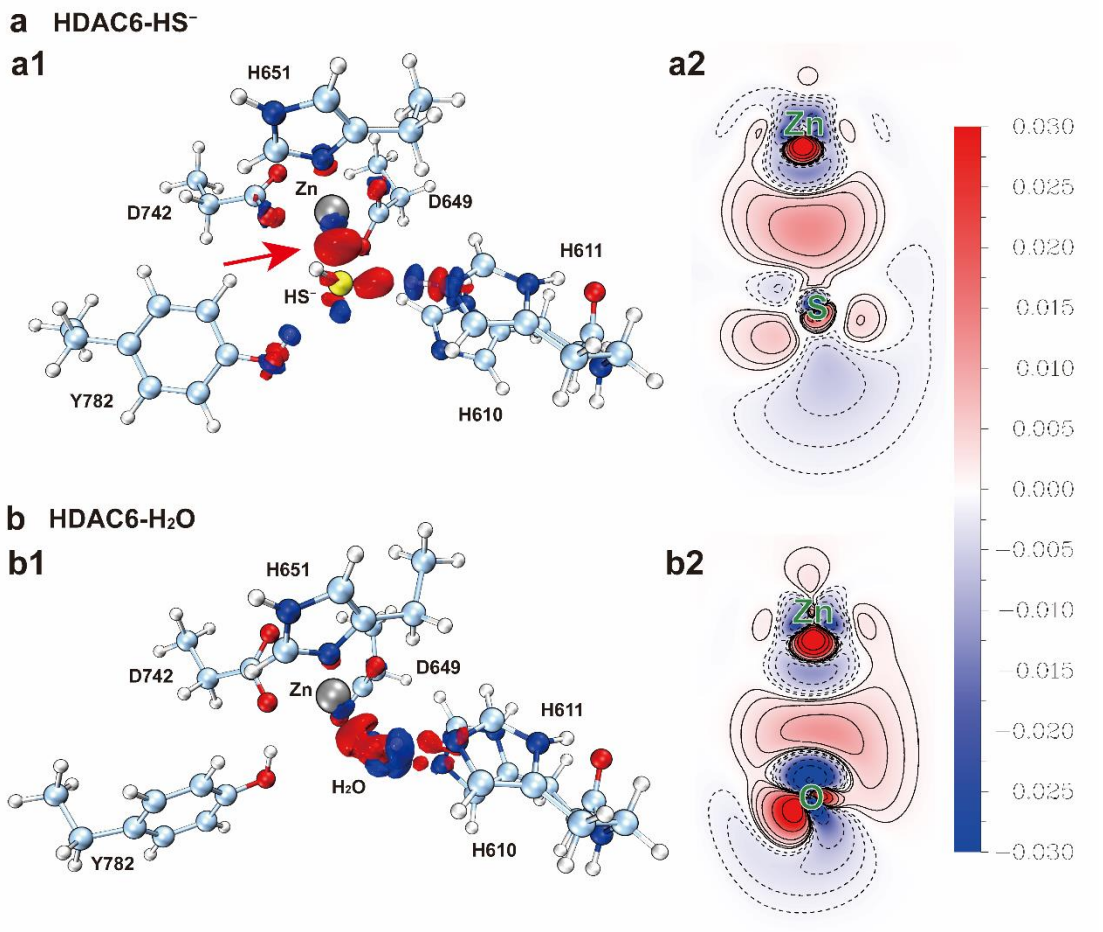


Figure S5 (for Figure 1e). Isosurface maps (a1 and b1, isovalue = 0.005 a.u.) and contour maps (a2 and b2) of electron density difference of the hHDAC6-CD2 active site coordinated with HS^- (a) or H_2O (b). Electron densities were calculated at ε = 4/PBE0-D3(BJ)/6-311+G(2d,2p)|SDD level. Red and blue regions correspond to the regions with an increase and a decrease in electron density upon binding between the enzyme and HS^- (**a**) or H_2O (**b**), respectively.

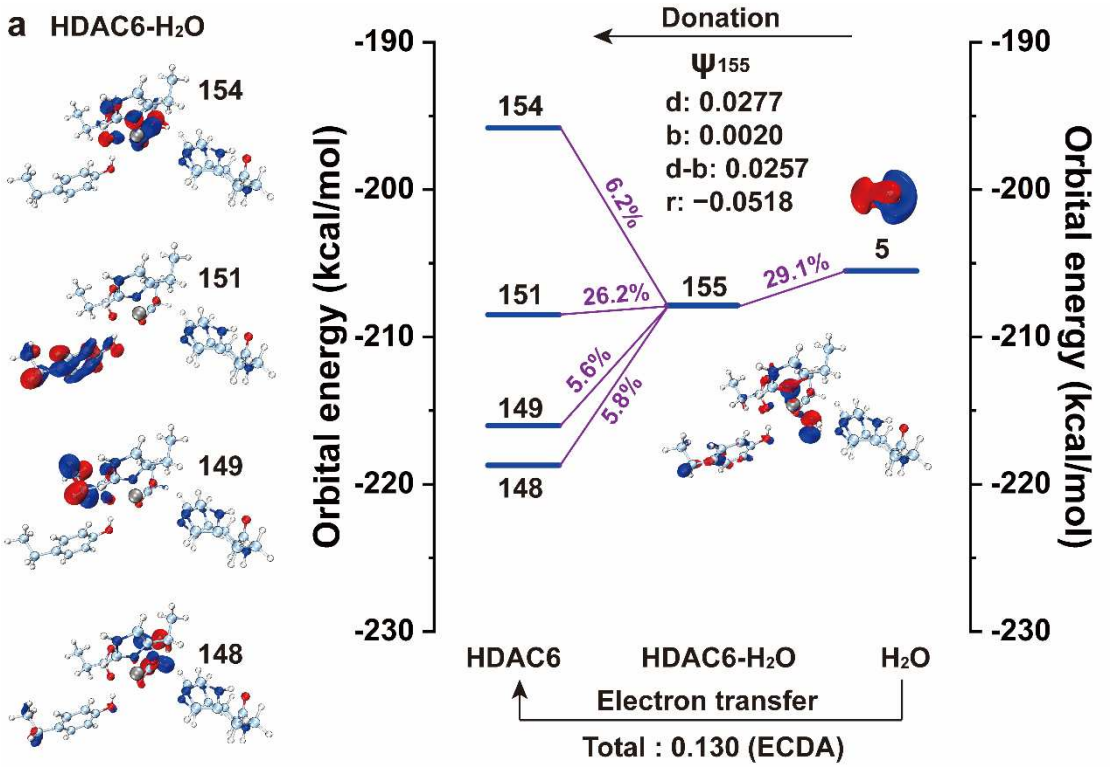


Figure S6 (for Figure 1f). Charge decomposition analysis (CDA) and orbital interaction diagram of the hHDAC6-CD2 active site coordinated with H_2O. Orbital compositions were calculated using Mulliken method at ε = 4/PBE0-D3(BJ)/def2-TZVP|SDD level. Blue solid bars corresponded to the energy of occupied molecular orbitals (MOs), denoted with individual orbital numbers corresponding to respective grades of energy levels. In isosurface maps (isovalue = 0.02 a.u.) of MOs corresponding to orbital numbers, red and blue regions respectively denoted the positive and negative orbital phases. Purple lines/texts indicated the particular contribution of each fragment MOs to the major complex MOs for the O–Zn bond. The number of electrons donated, the number of electrons back donated, and the number of electrons involved in repulsive polarization were expressed as d, b, and r for the binding process between HDAC6-CD2 and H_2O. The net electrons obtained by HDAC6 during this binding were

calculated using extended CDA (ECDA) method.

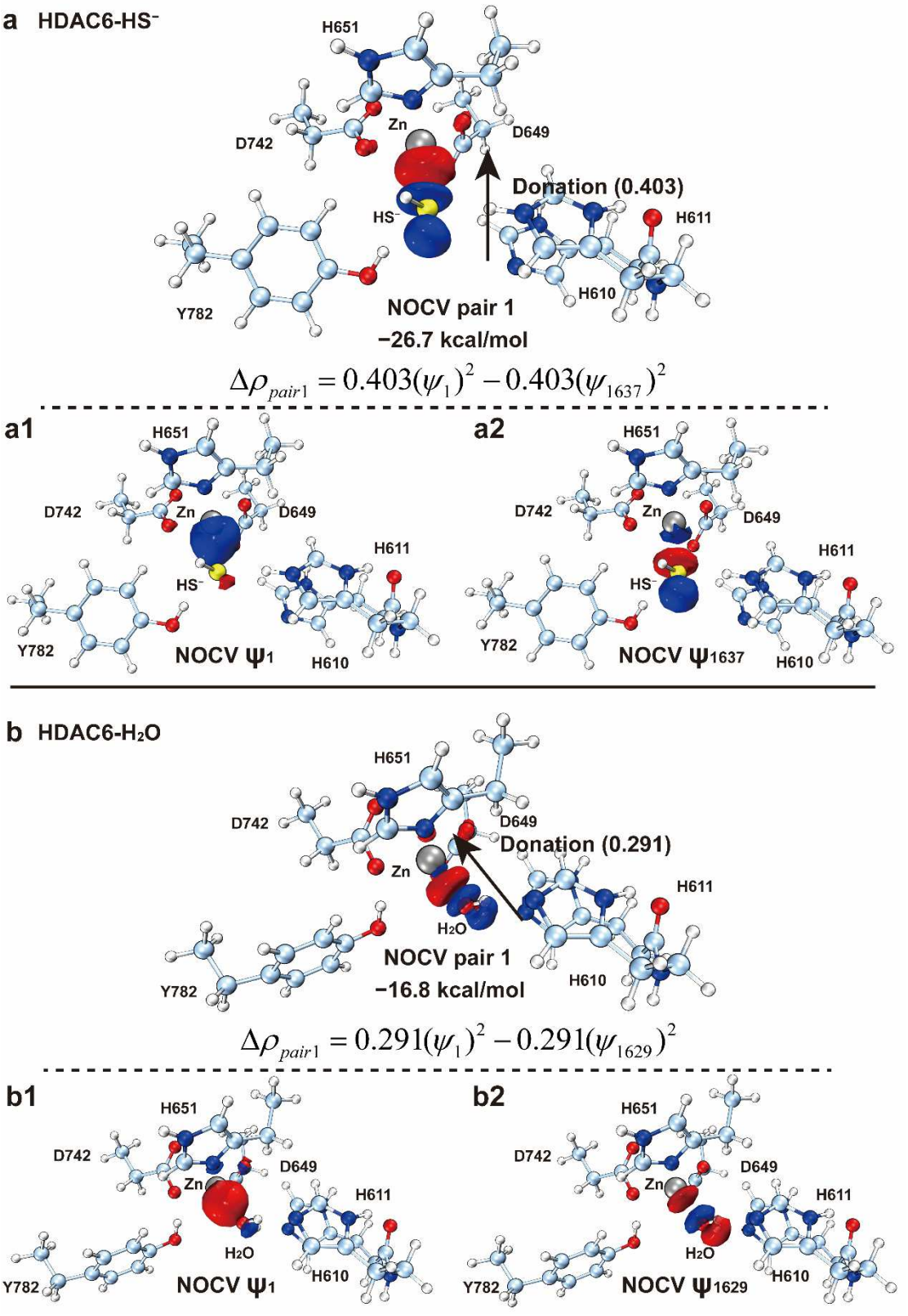


Figure S7 (for Figure 1e). Extended transition state - natural orbitals for chemical valence (ETS-NOCV) analysis of the hHDAC6-CD2 active site coordinated with HS^- (a) or H_2O (b). ETS-NOCVs were calculated at ε = 4/PBE0-D3(BJ)/6-311+G(2d,2p)|SDD level. Red and blue regions represented increased- and decreased electron density resulting from orbital interactions, respectively. **a** and **b**, Isosurface maps (isovalue = 0.003 a.u.) of NOCV pair 1 in the active site of HDAC6-CD2 coordinated with HS^- (**a**) or H_2O (**b**). The amount of transferred electron shown in absolute eigenvalue (σ-donation, $\Delta\rho_{pair1}$) in NOCV pair 1 were given in corresponding panels. The corresponding orbital stabilization energies were −26.7 kcal/mol and −16.8 kcal/mol in NOCV pair 1 of HDAC6-CD2 coordinated with HS^- and H_2O, respectively. **a1** and **a2**, isosurface maps (isovalue = 0.08 a.u.) of the complementary NOCV orbitals representing donation from ψ_{1637} (**a2**) to ψ_1 (**a1**) in HDAC6-CD2 coordinated with HS^-. **b1** and **b2**, Isosurface maps (isovalue = 0.08 a.u.) of the complementary NOCV orbitals representing donation from ψ_{1629} (**b2**) to ψ_1 (**b1**) in HDAC6-CD2 coordinated with H_2O. Red and blue regions in NOCV orbitals respectively denoted the positive and negative orbital phases.

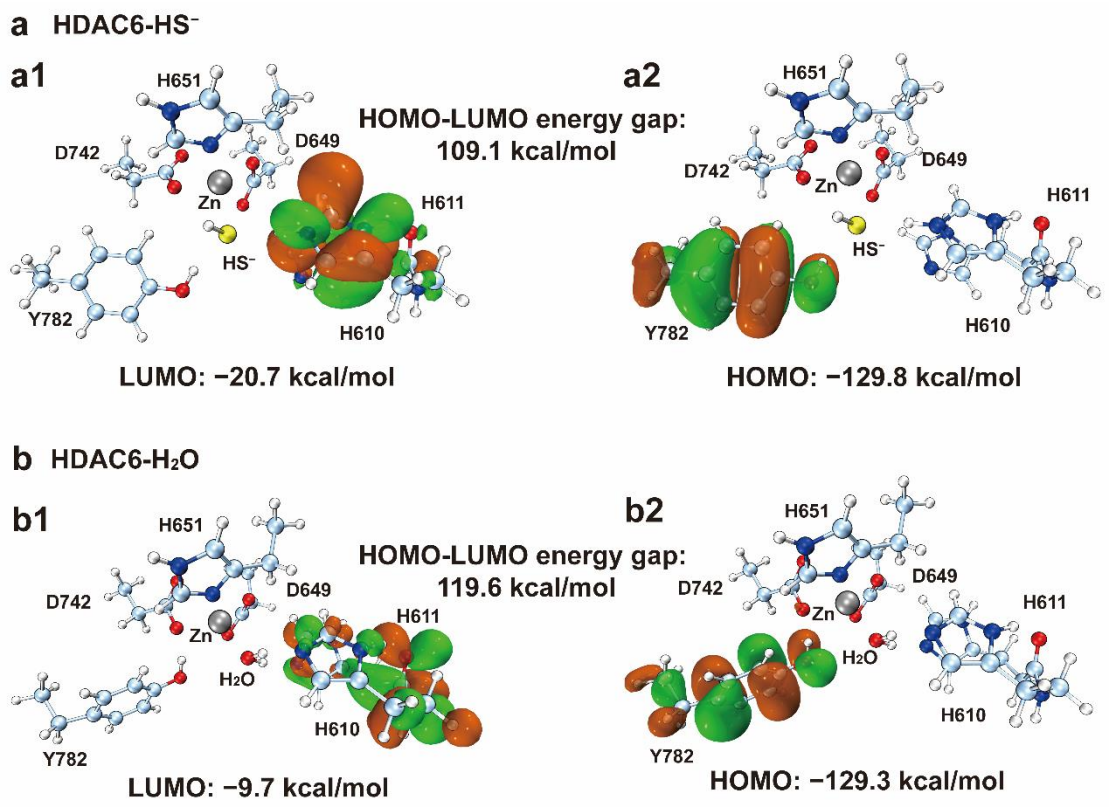


Figure S8 (for Figure 1a-e). Isosurface maps (isovalue = 0.02 a.u.) of highest occupied molecular orbital (HOMO) and lowest unoccupied molecular orbital (LUMO) of the hHDAC6-CD2 active site coordinated with HS^- (a) or H_2O (b). Energy gaps were calculated at ε = 4/B3PW91-D3(BJ)/6-311+G(2d,2p)|SDD level. Orange and green regions respectively denoted the positive and negative orbital phases.

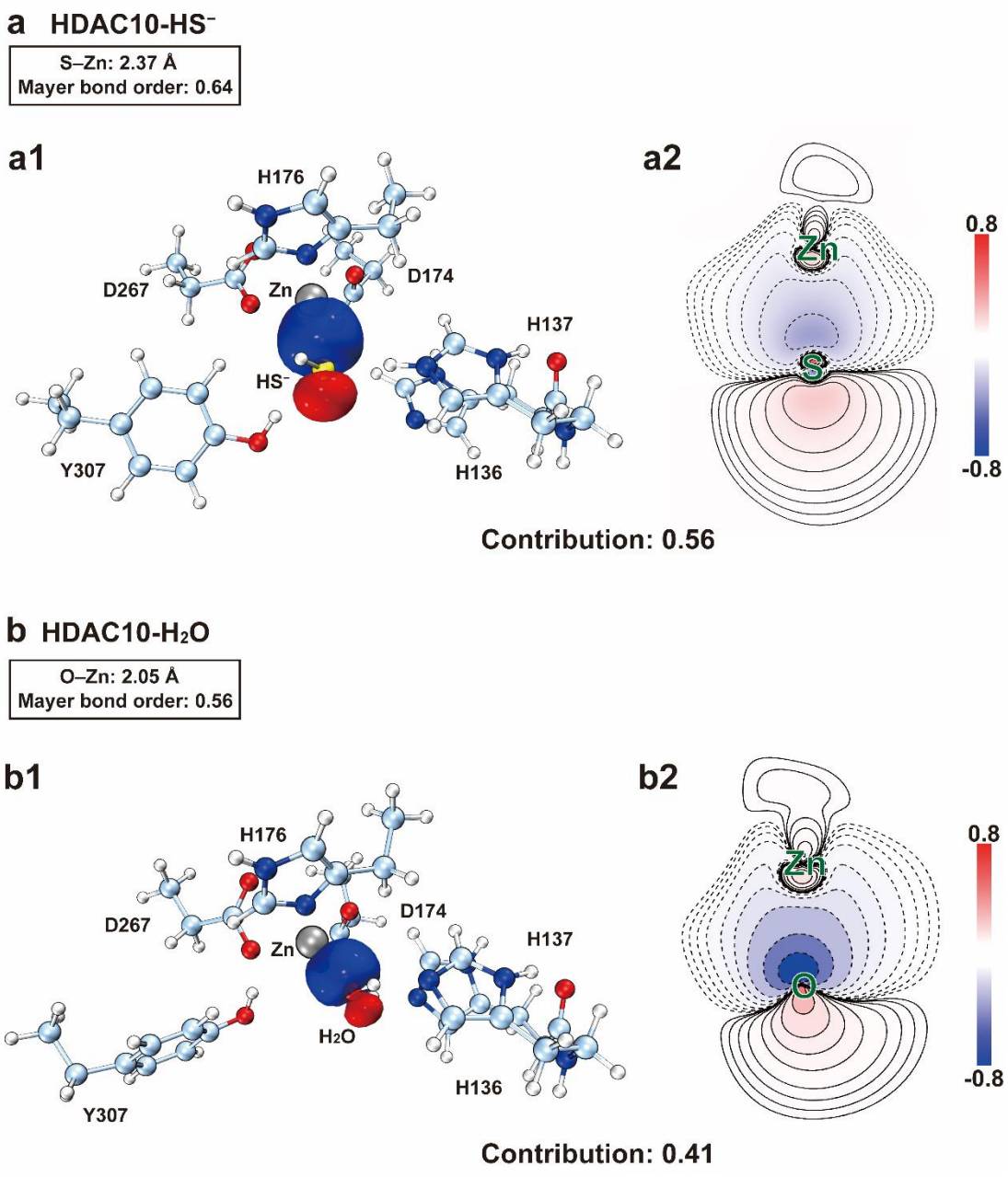


Figure S9 (for Figure 1h). One HS^- anion was coordinated to the zinc active site of HDAC10. Isosurface maps (isovalue = 0.05 a.u.) and contour maps of localized molecular orbitals (LMO) of the active sites of HDAC10 coordinated with HS^- (**a**) or H_2O (**b**). Mayer bond order (in Hilbert space) and LMO (Pipek-Mezey algorism with Mulliken population) were calculated at ε = 4/PBE0-D3(BJ)/def2-SVP|SDD level. Using orbital occupancy-perturbed bond order analysis, contribution of specific LMO

to bond order of S–Zn or O–Zn bonds was given at the bottom of individual LMO maps. Red and blue regions respectively denoted the positive and negative orbital phases.

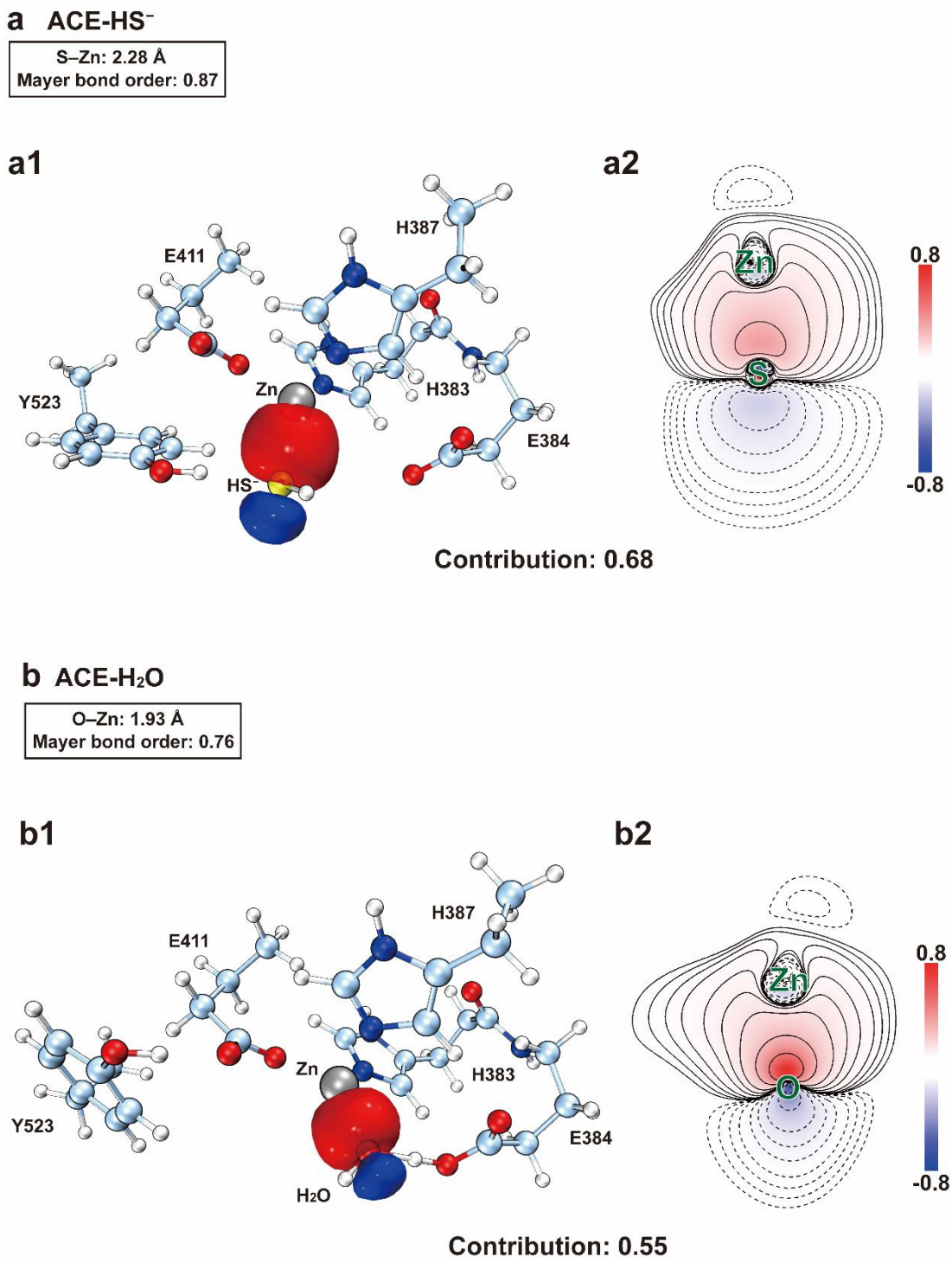


Figure S10 (for Figure 1h). One HS^- anion was coordinated to the zinc active site of angiotensin-converting enzyme (ACE). Isosurface maps (a1 and b1, isovalue = 0.05 a.u.) and contour maps (**a2** and **b2**) of localized molecular orbitals (LMO) of the active sites of ACE coordinated with HS^- (**a**) or H_2O (**b**). Mayer bond order (in Hilbert space) and LMO (Pipek-Mezey algorism with Mulliken population) were calculated at ε = 4/PBE0-D3(BJ)/def2-SVP|SDD level. Using orbital occupancy-perturbed bond order analysis, contribution of specific LMO to bond order of S–Zn or O–Zn bonds was given at the bottom of individual LMO maps. Red and blue regions respectively denoted the positive and negative orbital phases.

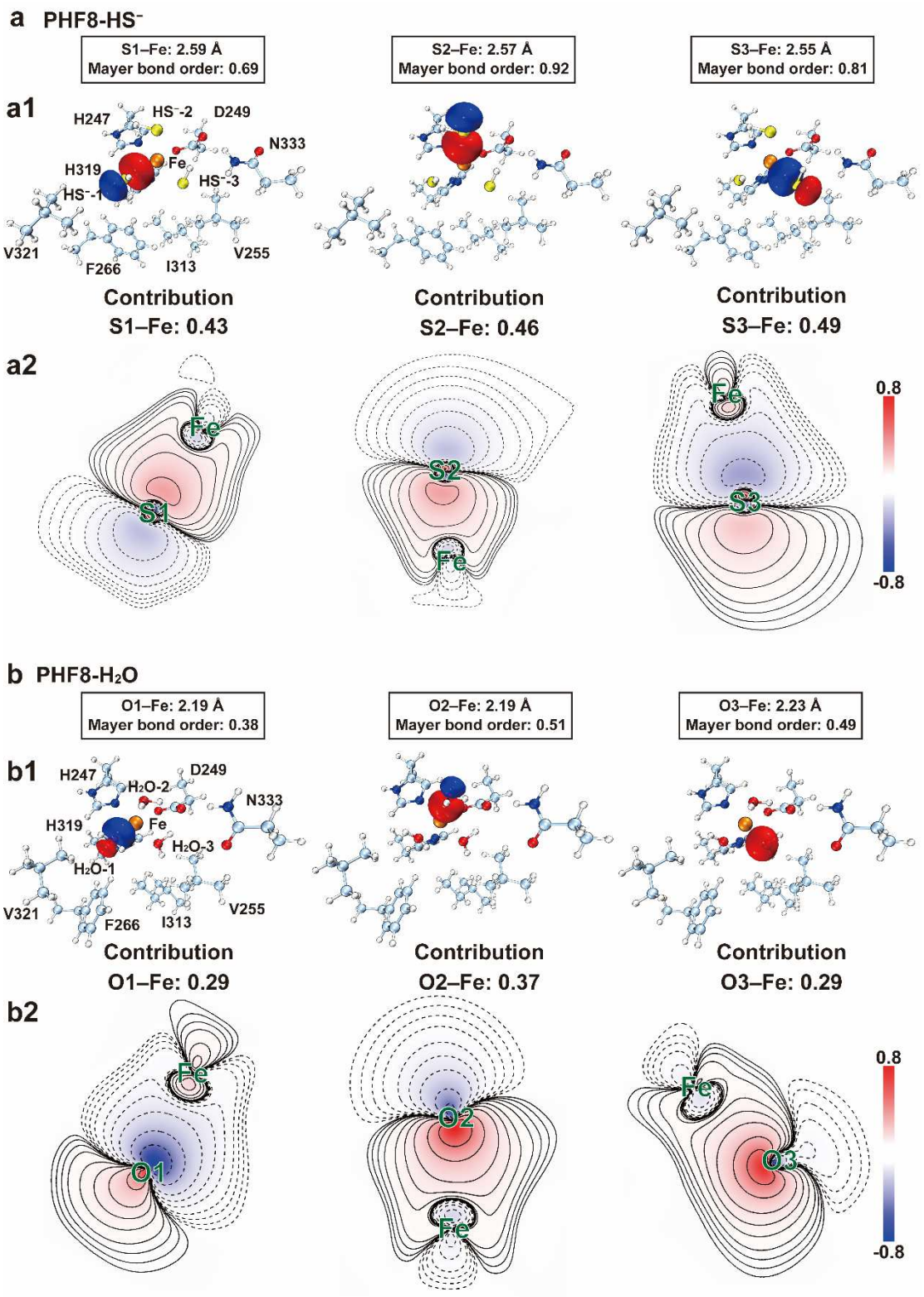

a PHF8-HS⁻
S1–Fe: 2.59 Å
Mayer bond order: 0.69
S2–Fe: 2.57 Å
Mayer bond order: 0.92
S3–Fe: 2.55 Å
Mayer bond order: 0.81
a1
H247
HS⁻-2
D249
N333
H319
Fe
HS⁻-3
HS⁻-1
V321
F266
I313
V255
Contribution
S1–Fe: 0.43
Contribution
S2–Fe: 0.46
Contribution
S3–Fe: 0.49
a2
Fe
S1
S2
Fe
Fe
S3
0.8
-0.8
b PHF8-H₂O
O1–Fe: 2.19 Å
Mayer bond order: 0.38
O2–Fe: 2.19 Å
Mayer bond order: 0.51
O3–Fe: 2.23 Å
Mayer bond order: 0.49
b1
H247
H₂O-2
D249
N333
H319
Fe
H₂O-3
H₂O-1
V321
F266
I313
V255
Contribution
O1–Fe: 0.29
Contribution
O2–Fe: 0.37
Contribution
O3–Fe: 0.29
b2
Fe
O1
O2
Fe
Fe
O3
0.8
-0.8

Figure S11 (for Figure 1h). Three HS^- anions were coordinated to the ferrum active site of histone lysine demethylase (PHF8). Isosurface maps (**a1** and **b1**, isovalue = 0.05 a.u.) and contour maps (**a2** and **b2**) of localized molecular orbitals (LMO) of the active sites of PHF8 coordinated with HS^- (**a**) or H_2O (**b**). Mayer bond order (in Hilbert space) and LMO (Pipek-Mezey algorism with Mulliken population) were calculated at ε = 4/PBE0-D3(BJ)/def2-SVP|SDD level. Using orbital occupancy-perturbed bond order analysis, contribution of specific LMO to the bond order of S–Fe or O–Fe bonds was given at the bottom of individual LMO maps. Red and blue regions respectively denoted the positive and negative orbital phases.

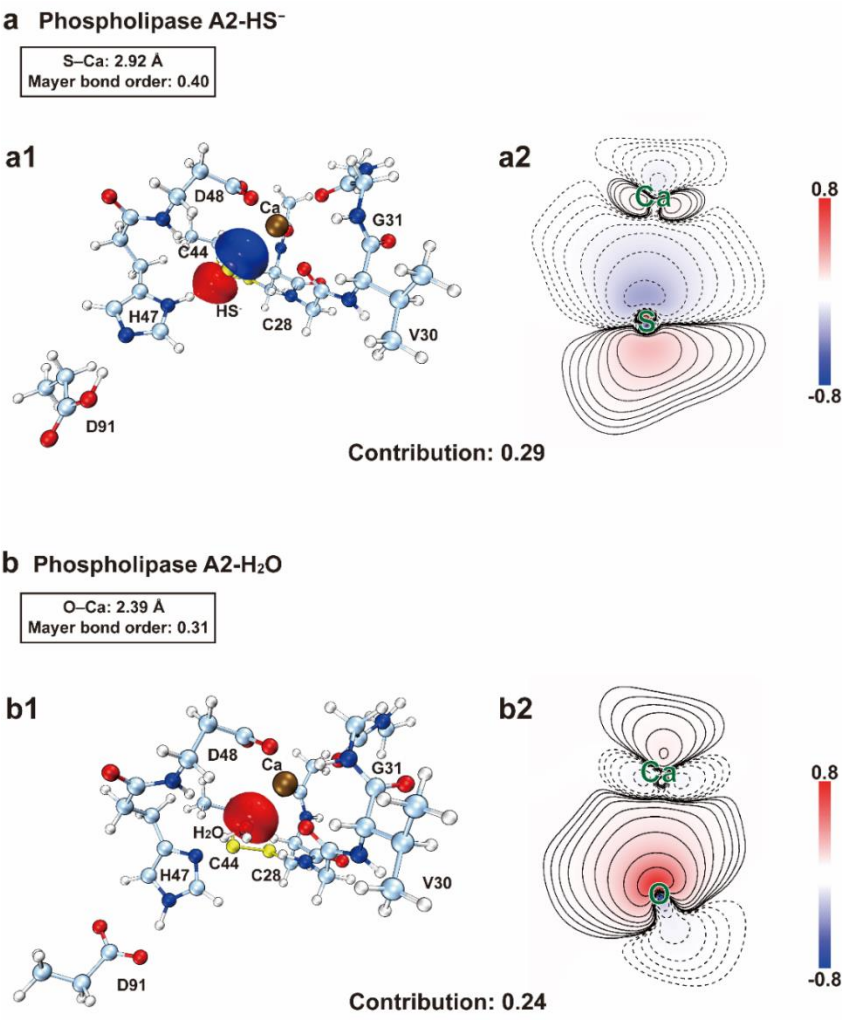


Figure S12 (for Figure 1h). One HS^- anion was coordinated to the calcium active site of phospholipase A2. Isosurface maps (a1 and b1, isovalue = 0.05 a.u.) and contour maps (**a2** and **b2**) of localized molecular orbitals (LMO) of the active sites of phospholipase A2 coordinated with HS^- (**a**) or H_2O (**b**). Mayer bond order (in Hilbert space) and LMO (Pipek-Mezey algorism with Mulliken population) were calculated at ε = 4/PBE0-D3(BJ)/def2-SVP|SDD level. Using orbital occupancy-perturbed bond order analysis, contribution of specific LMO to the bond order of S–Ca or O–Ca bonds was given at the bottom of individual LMO maps. Red and blue regions respectively denoted the positive and negative orbital phases.

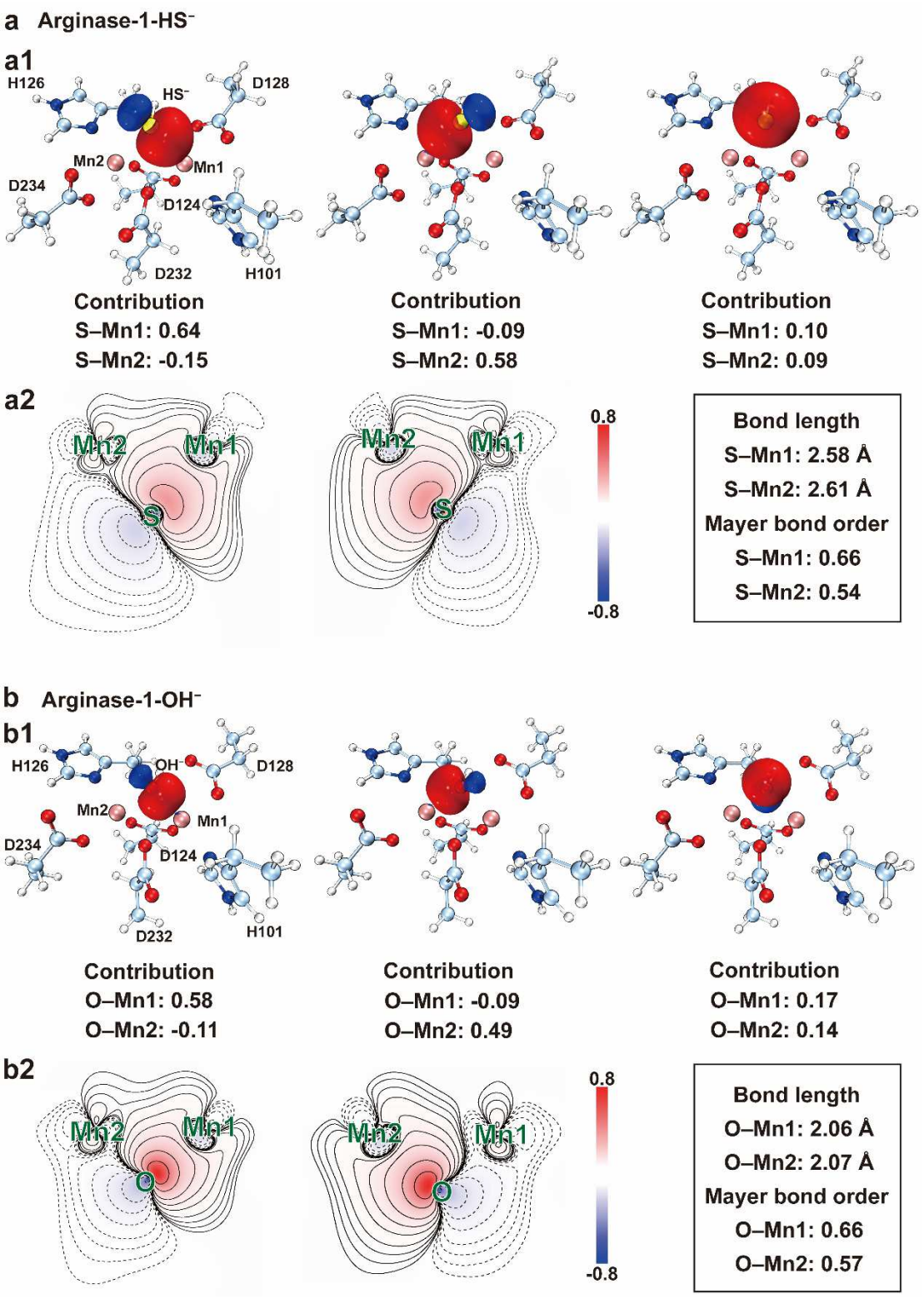

a Arginase-1-HS⁻
a1
H126
HS⁻
D128
Mn2
Mn1
D234
D124
D232
H101
Contribution
S–Mn1: 0.64
S–Mn2: -0.15
Contribution
S–Mn1: -0.09
S–Mn2: 0.58
Contribution
S–Mn1: 0.10
S–Mn2: 0.09
a2
Mn2
Mn1
S
0.8
-0.8
Bond length
S–Mn1: 2.58 Å
S–Mn2: 2.61 Å
Mayer bond order
S–Mn1: 0.66
S–Mn2: 0.54
b Arginase-1-OH⁻
b1
H126
OH⁻
D128
Mn2
Mn1
D234
D124
D232
H101
Contribution
O–Mn1: 0.58
O–Mn2: -0.11
Contribution
O–Mn1: -0.09
O–Mn2: 0.49
Contribution
O–Mn1: 0.17
O–Mn2: 0.14
b2
Mn2
Mn1
O
0.8
-0.8
Bond length
O–Mn1: 2.06 Å
O–Mn2: 2.07 Å
Mayer bond order
O–Mn1: 0.66
O–Mn2: 0.57

Figure S13 (for Figure 1h). One HS^- anion was coordinated to two catalytic manganese ions in the active site of arginase-1. Isosurface maps (**a1** and **b1**, isovalue = 0.05 a.u.) and contour maps (**a2** and **b2**) of localized molecular orbitals (LMO) of the active sites of arginase-1 coordinated with HS^- (a) or H_2O (b). Mayer bond order (in Hilbert space) and LMO (Pipek-Mezey algorism with Mulliken population) were calculated at ε = 4/PBE0-D3(BJ)/def2-SVP|SDD level. Using orbital occupancy-perturbed bond order analysis, contribution of specific LMO to the bond order of S–Mn or O–Mn bonds was given at the bottom of individual LMO maps. Red and blue regions respectively denoted the positive and negative orbital phases.

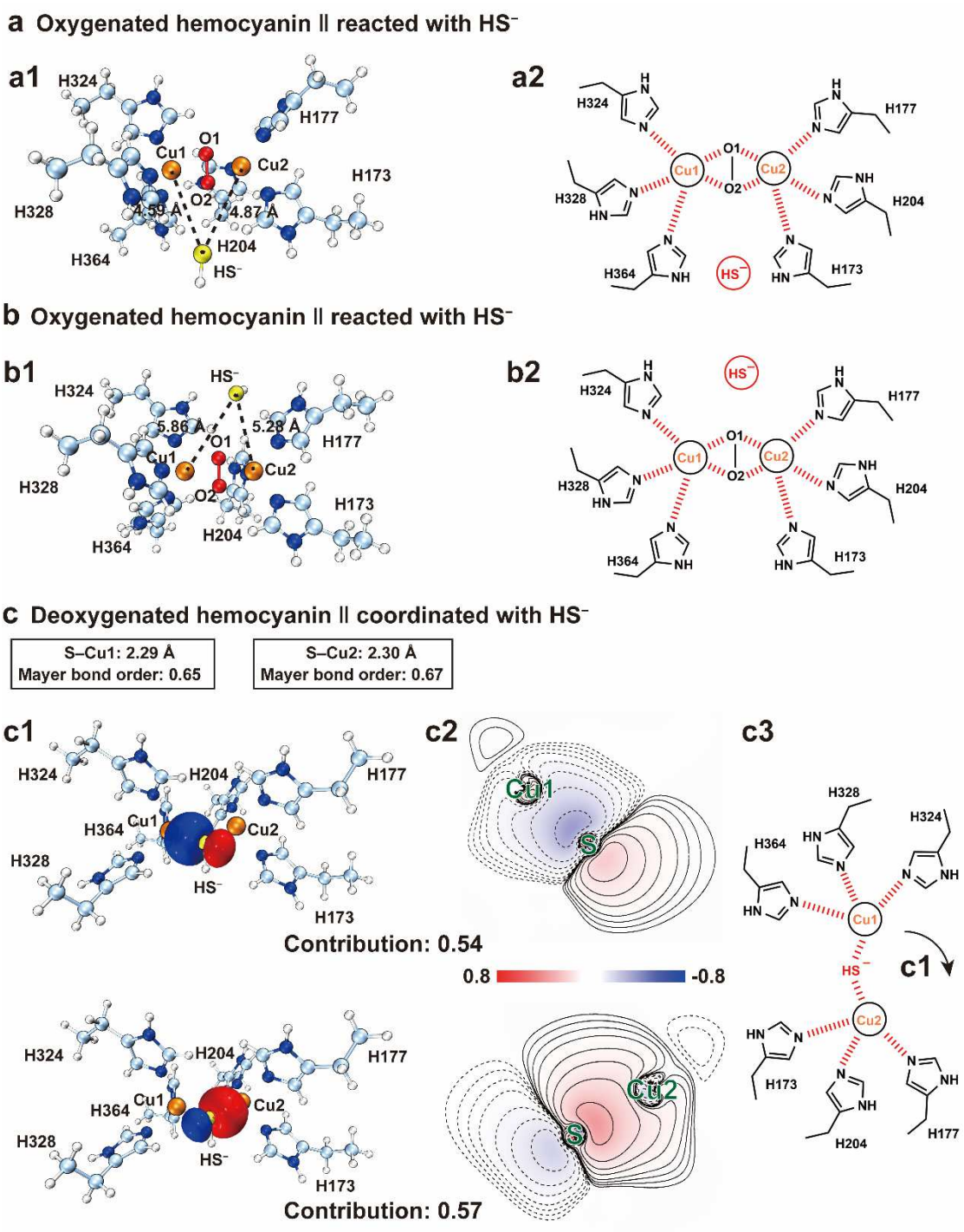

a Oxygenated hemocyanin II reacted with HS⁻
a1
H324
H177
O1
Cu1
Cu2
H173
H328
O2
4.59 Å
4.87 Å
H204
H364
HS⁻
a2
b Oxygenated hemocyanin II reacted with HS⁻
b1
HS⁻
H324
5.86 Å
5.28 Å
O1
H177
Cu1
Cu2
H328
O2
H173
H364
H204
b2
c Deoxygenated hemocyanin II coordinated with HS⁻
S–Cu1: 2.29 Å
Mayer bond order: 0.65
S–Cu2: 2.30 Å
Mayer bond order: 0.67
c1
c2
c3
Contribution: 0.54
0.8
-0.8
Contribution: 0.57
c1

Figure S14 (for Figure 1h). HS^- did not coordinated at the Cu-centered active site of oxygenated hemocyanin II but to that of deoxygenated hemocyanin II. HS^- was modeled around the two Cu ions in the active site at the initial state of the structure. Two minima (**a1** and **b1**) of HS^- locations were found following structure optimization where S–Cu distance was at least 4.59 Å. **a2** and **b2**, Schematic diagrams of **a1** and **b1** showing that fully coordinated active-site Cu^{2+} ions (five-coordinate) did not coordinate with HS^-. **c**, Isosurface maps (**c1**, isovalue = 0.05 a.u.) and contour maps (**c2**) of localized molecular orbitals (LMO) of the active sites of deoxygenated hemocyanin II coordinated with an HS^-. Mayer bond order (in Hilbert space) and LMO (Pipek-Mezey algorism with Mulliken population) were calculated at ε = 4/PBE0-D3(BJ)/def2-SVP|SDD level. Using orbital occupancy-perturbed bond order analysis, contribution of specific LMO to the bond order of S–Cu bonds was given at the bottom of individual LMO maps. Red and blue regions respectively denoted the positive and negative orbital phases. **c3**, Schematic diagrams (90-degree clockwise rotation) of **c1** showing two active-site Cu^+ ions coordinated with one HS^-.

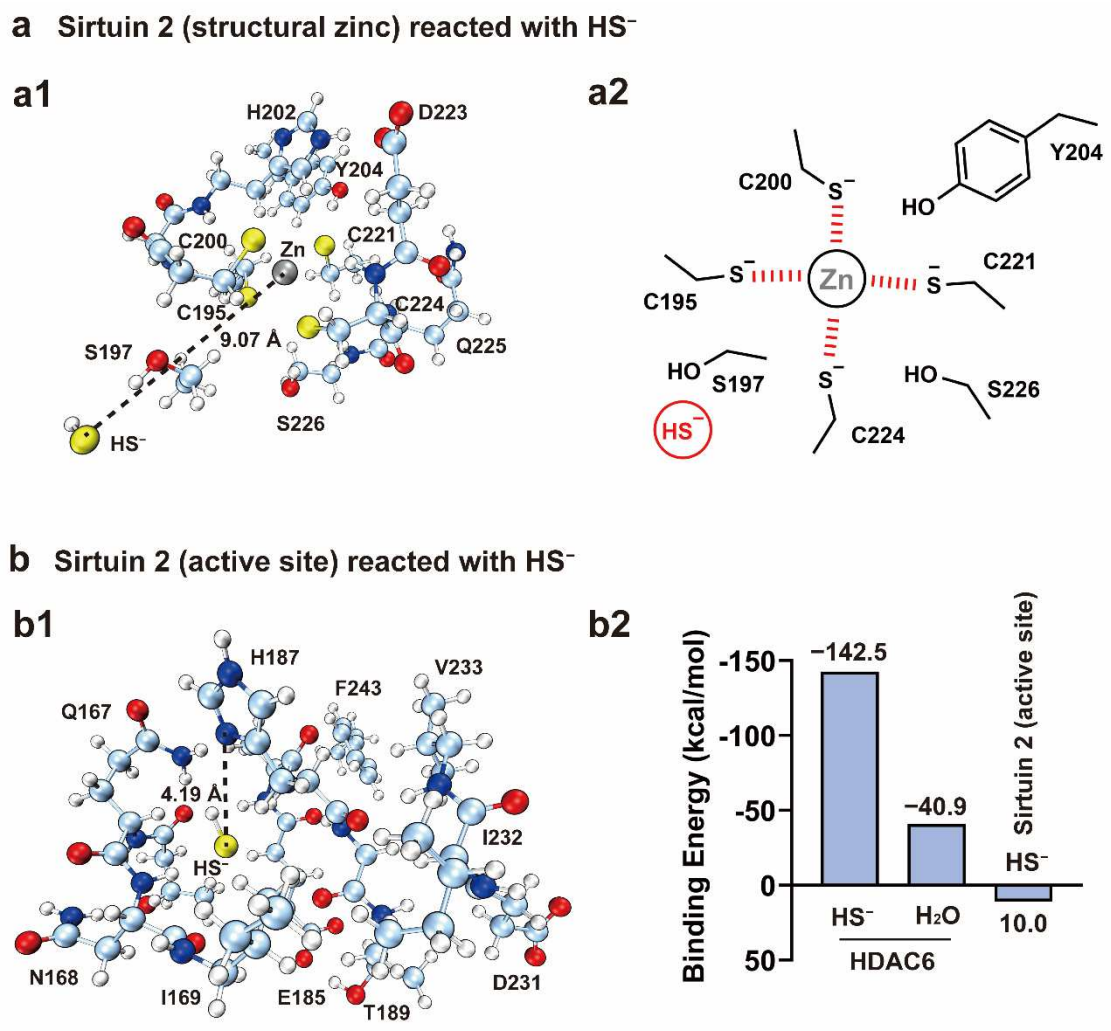


Figure S15 (for Figure 1h). HS^- did not coordinate to structural zinc ion (a) contained in sirtuin 2, nor to the non-metallic active site of the enzyme (b). a, Optimized structure of sirtuin 2 structural zinc with surrounding residues interacted with HS^- (**a1**). A minimum of HS^- location was 9.07 Å away from the structural Zn^{2+} ion. **a2**, Schematic diagram showing that HS^- was kept away from the structural Zn^{2+} ion by surrounding steric hindrance. **b**, Optimized structure of active site of sirtuin 2 interacted with HS^- (b1). **b2**, Binding electronic energy between HDAC6 and HS^-/H_2O in contrast to that between sirtuin 2 and HS^- calculated at MN15/6-311+G(2d,2p)|SDD level.

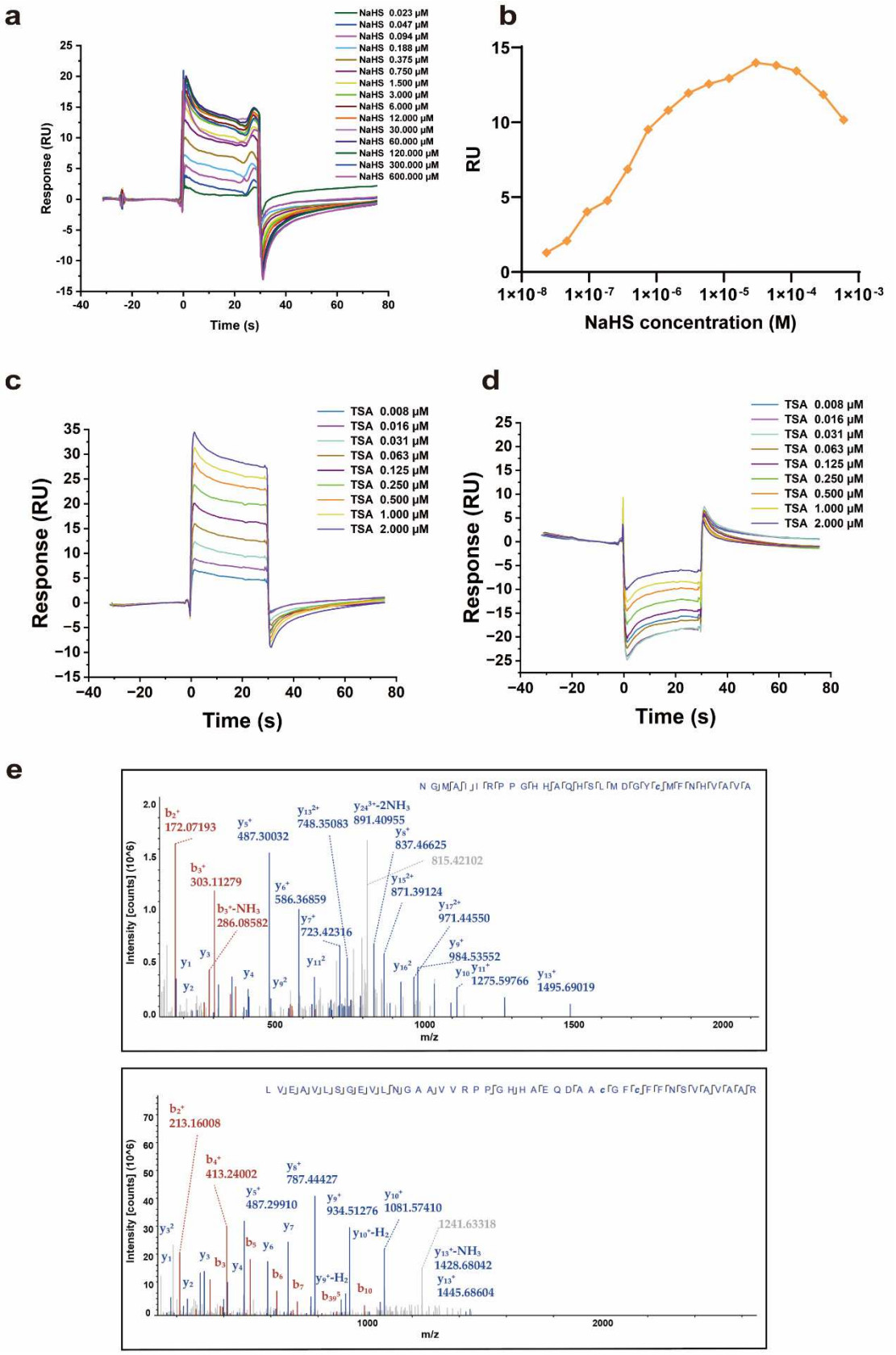

a
NaHS 0.023 μM
NaHS 0.047 μM
NaHS 0.094 μM
NaHS 0.188 μM
NaHS 0.375 μM
NaHS 0.750 μM
NaHS 1.500 μM
NaHS 3.000 μM
NaHS 6.000 μM
NaHS 12.000 μM
NaHS 30.000 μM
NaHS 60.000 μM
NaHS 120.000 μM
NaHS 300.000 μM
NaHS 600.000 μM
Response (RU)
Time (s)
b
RU
NaHS concentration (M)
c
TSA 0.008 μM
TSA 0.016 μM
TSA 0.031 μM
TSA 0.063 μM
TSA 0.125 μM
TSA 0.250 μM
TSA 0.500 μM
TSA 1.000 μM
TSA 2.000 μM
Response (RU)
Time (s)
d
TSA 0.008 μM
TSA 0.016 μM
TSA 0.031 μM
TSA 0.063 μM
TSA 0.125 μM
TSA 0.250 μM
TSA 0.500 μM
TSA 1.000 μM
TSA 2.000 μM
Response (RU)
Time (s)
e
Intensity [counts] (10^6)
m/z
Intensity [counts] (10^6)
m/z

Figure S16 (for Figure 2). H_2S bound directly to the catalytic zinc in hHDAC6-CD1-2 without inducing any chemical modifications on the cysteine residues. a-b, SPR sensorgram showing the kinetic analysis of H_2S binding to the hHDAC6-CD1-2 protein. **c**, SPR sensorgram showing the TSA binding to the hHDAC6-CD1-2 protein with the presence of 12 μM NaHS. **d**, SPR sensorgram showing the TSA binding to the hHDAC6-CD1-2 protein with the presence of 600 μM NaHS. **e**, Representative HPLC-MS results showing no S-sulfhydration was detected on the cysteine residues of the hHDAC6 CD1-2 protein treated with 12 μM NaHS.

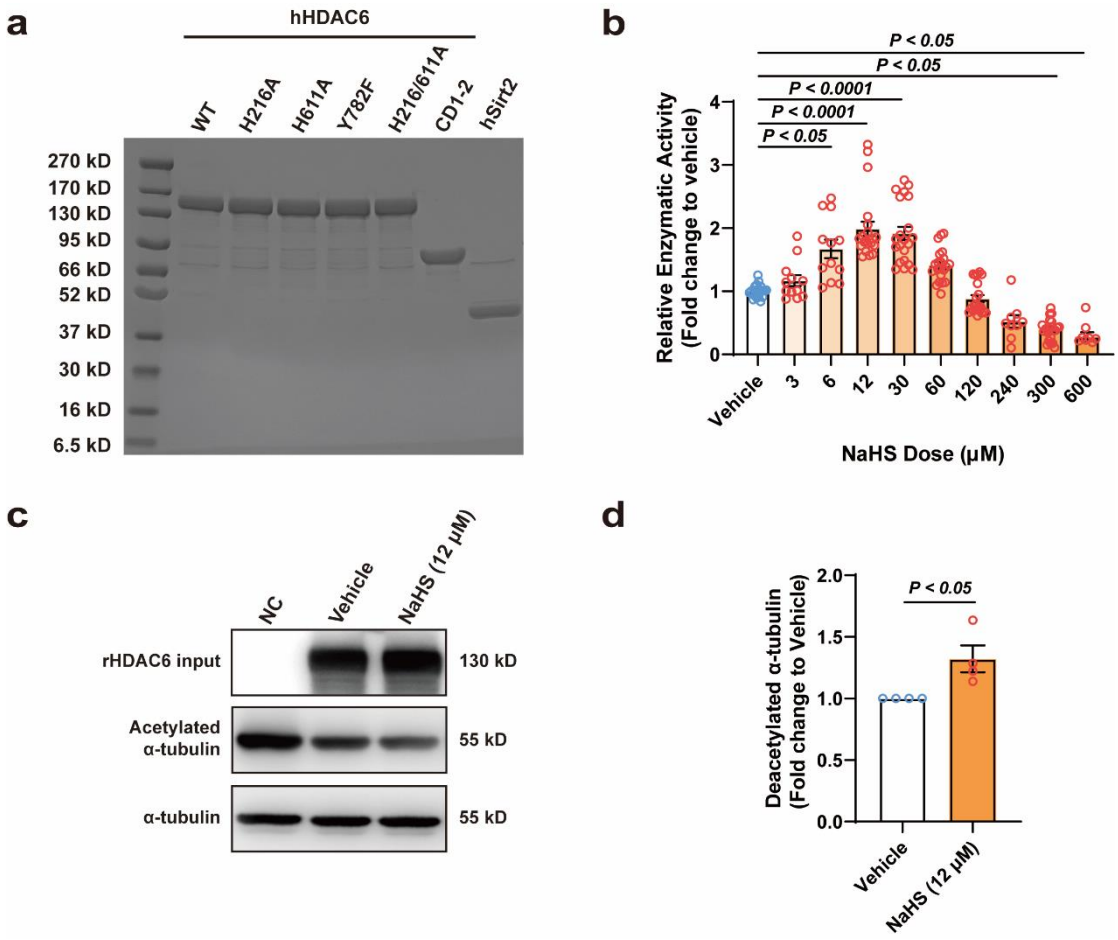


Figure S17 (for Figure 3). H_2S up-regulated the enzyme activity of hHDAC6. a, SDS-PAGE analysis of the purified recombinant human HDAC6 constructs and human sirt2 used in enzymatic analysis. **b**, Dose-response relationship of NaHS treatment on enzyme activity of HDAC6-CD1-2, n = 15-21. **c-d**, Effects of NaHS treatment (12 μM) on the enzyme activity of full-length α-tubulin substrate extracted from HDAC6 knockout EA.hy926 endothelial cells, n = 4.

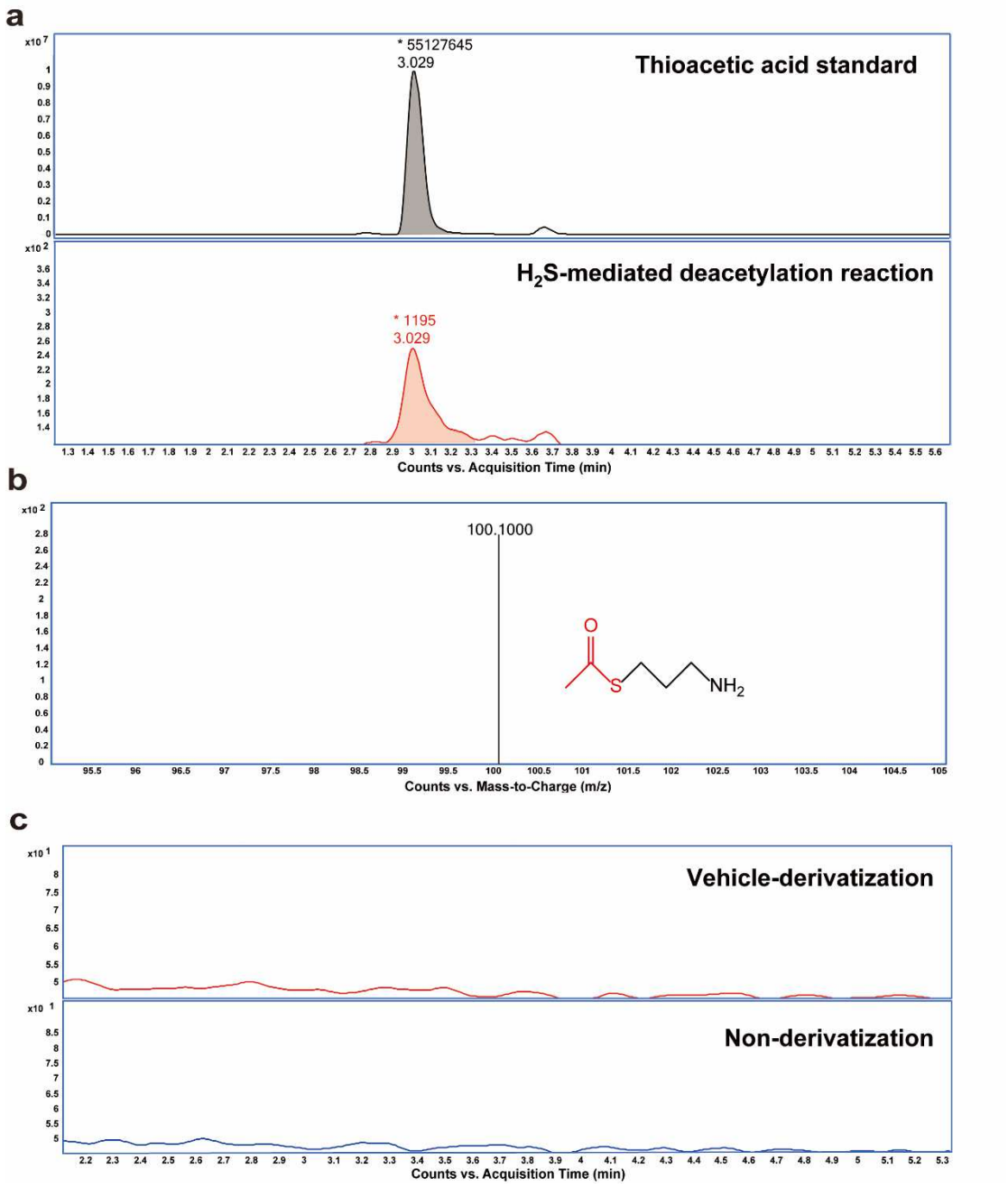


Figure S18 (for Figure 3h). Thioacetic acid was identified in cell-free system. a - b, UHPLC-qqq-MS analysis of the derivatized Thioacetic acid standard and products yielded from the enzymatic assay administrated with 12 μM NaHS. **c**, UHPLC-qqq-MS analysis of the derivatized and non-derivatized products from the enzymatic assay. UHPLC-qqq-MS, Ultra-high performance liquid chromatography-tandem triple

quadrupole mass spectrometry.

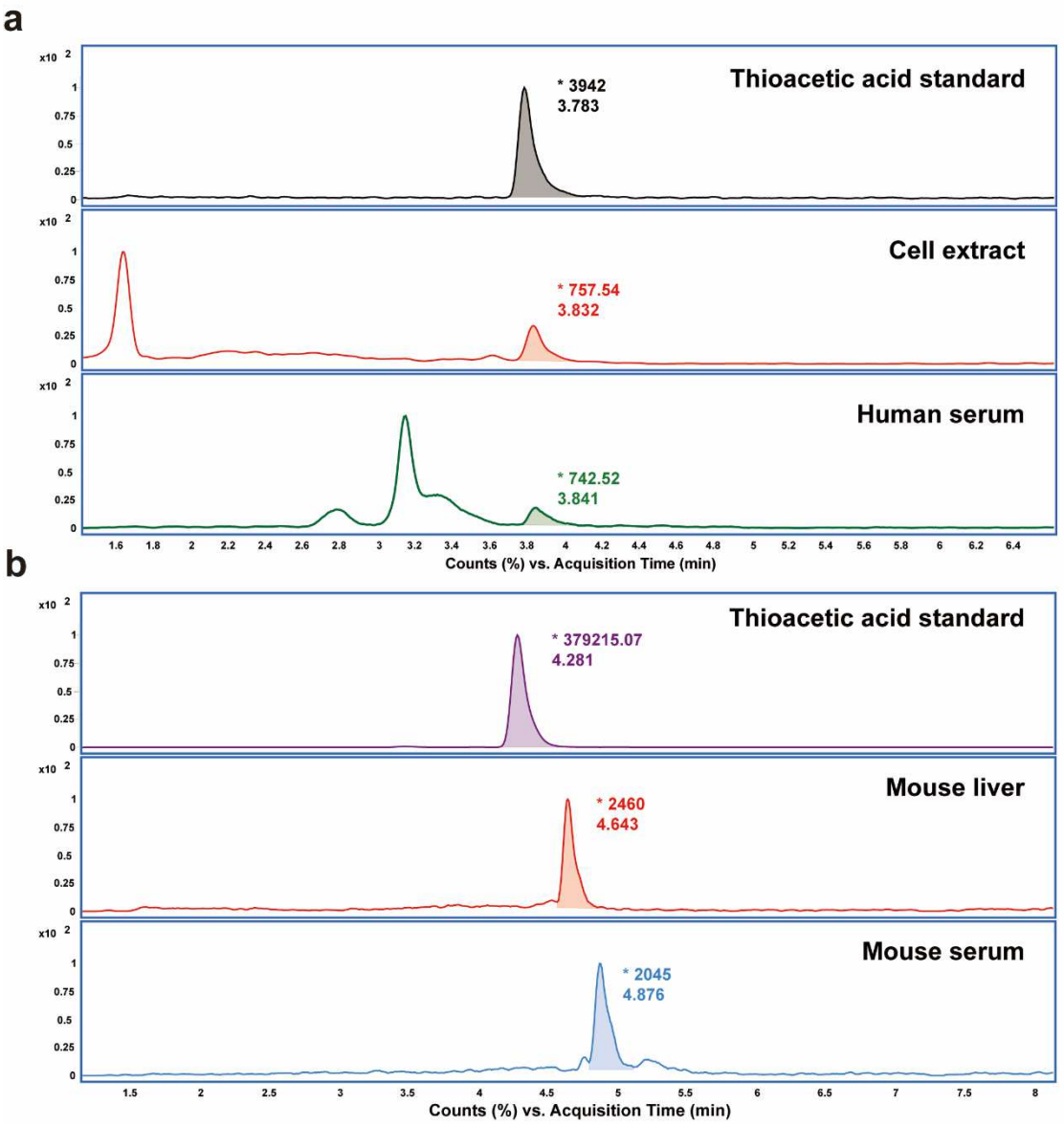


Figure S19 (for Figure 3). Thioacetic acid was identified in a series of biological samples. a, Representative UHPLC-qqq-MS analysis of the derivatized Thioacetic acid standard and samples extracted from cultured 293T cells and human serum. **b**, Representative UHPLC-qqq-MS analysis of the derivatized Thioacetic acid standard and samples extracted from mouse liver and serum.

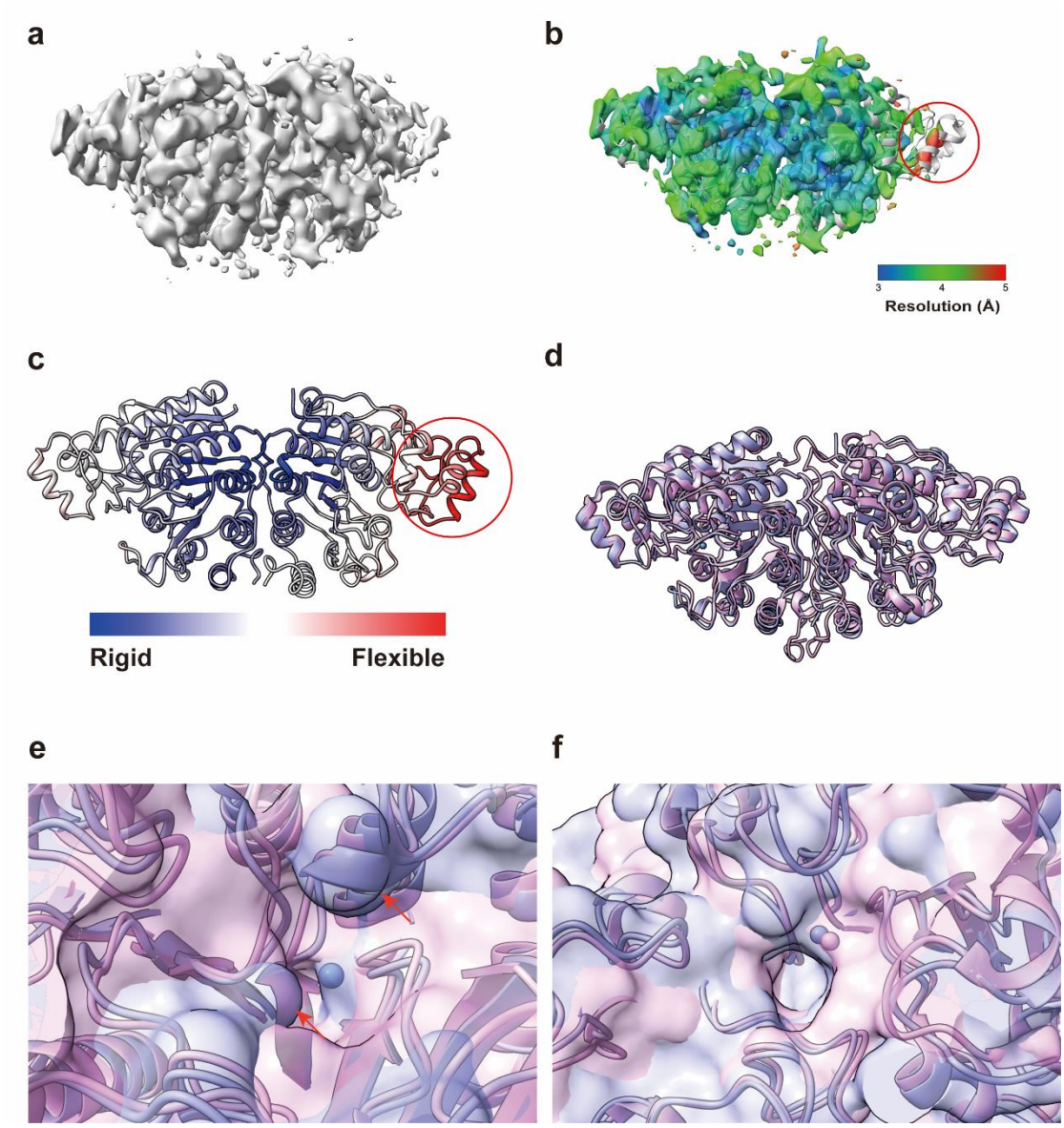


Figure S20 (for Figure 4). Determination of the structure of hHDAC6 and the comparison between hHDAC6 and zHDAC6. a, Cryo-EM density map of hHDAC6-CD1-2. **b**, Local resolution of the cryo-EM density map of hHDAC6-CD1-2 overlapping with AlphaFold2 predicted model with a red circle indicating the region with deteriorated density quality in CD2 tip. **c**, B-factor coloring showing flexibility of various regions in the overall hHDAC6-CD1-2 model. **d**, Backbone structure showing

hHDAC6-CD1-2 overlapping with zHDAC6-CD1-2 (PDB ID: 5G0J). **e** and **f**, top view of overlapped active-site tunnels of hHDAC6 (purple) and zHDAC6 (pink) in CD1 (**e**) and CD2 (**f**), respectively. Red arrows indicate the distinct mass of K353 and Y225 found in hHDAC6-CD1 but not in zHDAC6.

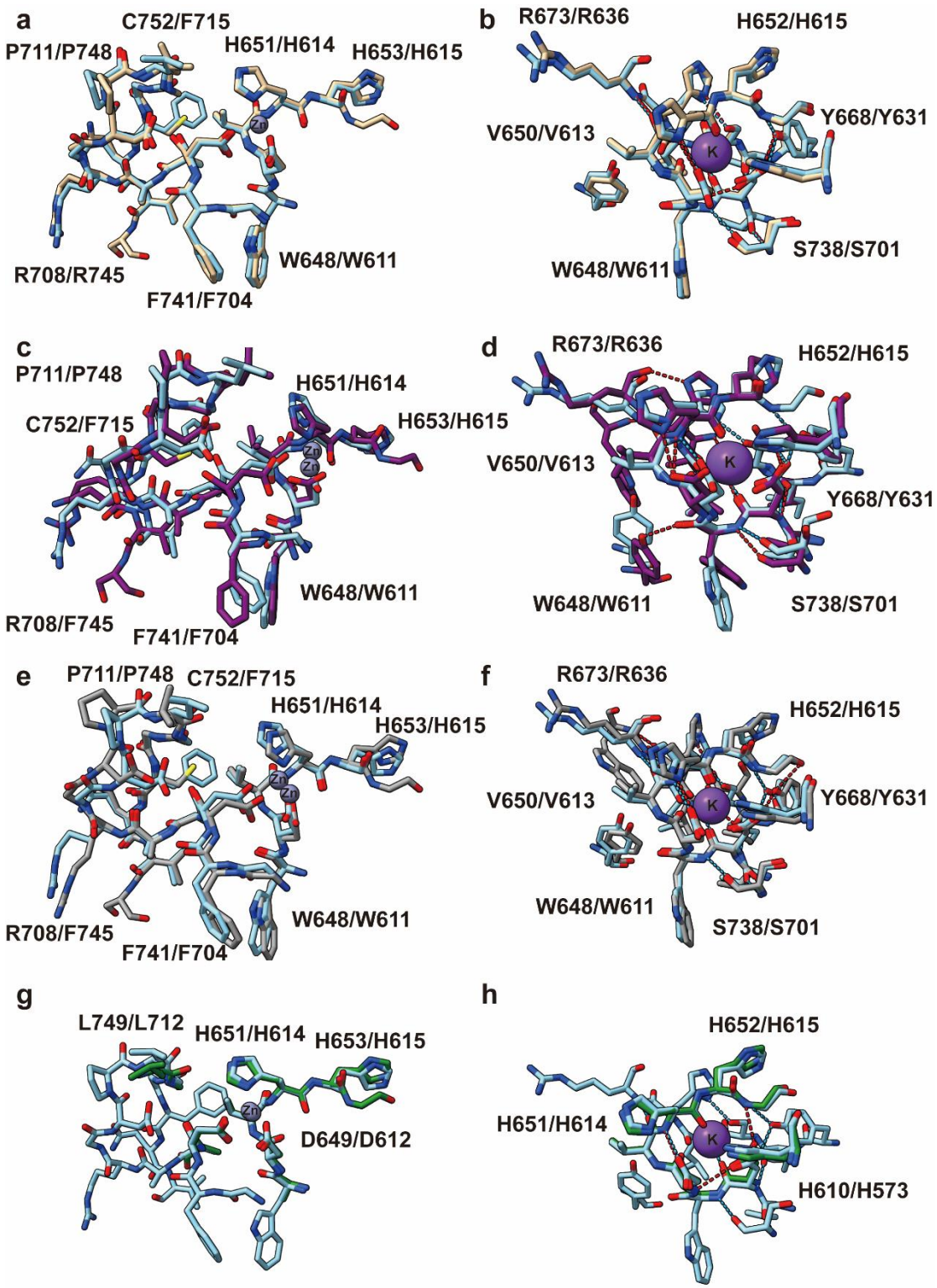


Figure S21 (for Figure 4). The comparison of the hydrogen-binding networks and the second shell amino acids centered by the catalytic Zn^{2+} ion between hHDAC6-CD2 and zHDAC6-CD2. a and **b**, Close-up view of the second shell amino acids

surrounding the Zn^{2+} ion (**a**), and position and hydrogen-binding networks of K^+ ion (**b**) in the crystal zHDAC6-CD2 (PDB ID: 5WGI) (blue) and the starting model generated by AlphaFold2 (tan). The dashed line indicates the position of hydrogen bonds in the zHDAC6-CD2 structure (blue) and starting model generated by AlphaFold2 (red). **c**, Close-up view of the second shell amino acids surrounding the Zn^{2+} ion in the crystal zHDAC6-CD2 (PDB ID: 5WGI) (blue) and the CryoEM structure (purple). **d**, Close-up view of the position and hydrogen-binding networks of K^+ ion in the crystal zHDAC6-CD2 (PDB ID: 5WGI) (blue) and the MD-equilibrated CryoEM structure including K^+ ion (purple). The dashed line indicates the position of hydrogen bonds in the zHDAC6-CD2 structure (blue) and the MD-equilibrated CryoEM structure including K^+ ion (red). **e** and **f**, Close-up view of the second shell amino acids surrounding the Zn^{2+} ion (**e**), and position and hydrogen-binding networks of K^+ ion (**f**) in the crystal zHDAC6-CD2 (PDB ID: 5WGI) (blue) and the MD-derived model of ES complex (grey). The dashed line indicates the position of hydrogen bonds in the zHDAC6-CD2 structure (blue) and the MD-derived model of ES complex (red). **g** and **f**, Close-up view of the second shell amino acids surrounding the Zn^{2+} ion (**g**), and position and hydrogen-binding networks of K^+ ion (**f**) in the crystal zHDAC6-CD2 (PDB ID: 5WGI) (blue) and the optimized model used in QC calculation (green). The dashed line indicates the position of hydrogen bonds in the zHDAC6-CD2 structure (blue) and the optimized model used in QC calculation (red).

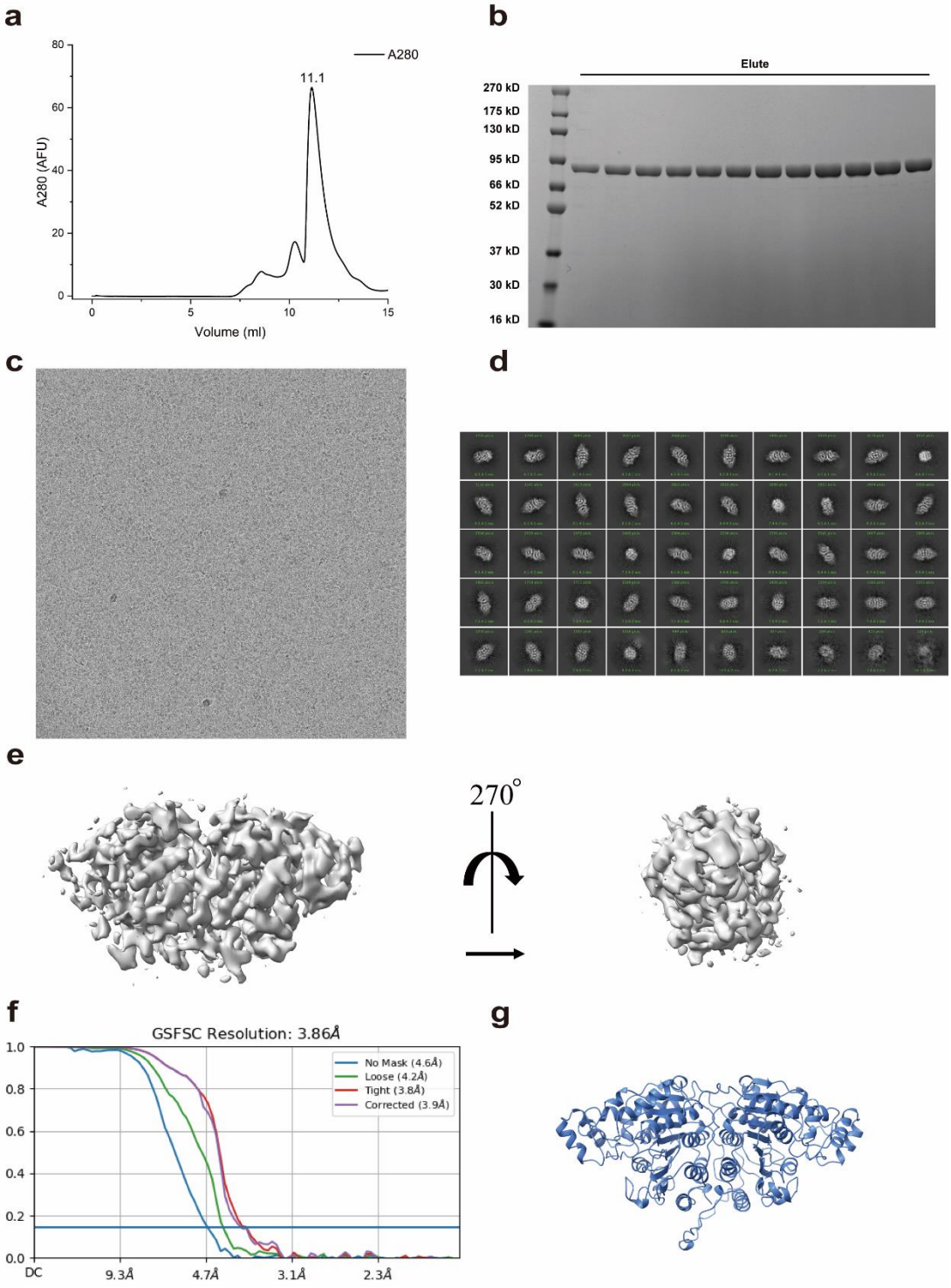


Figure S22 (for Figure 4). Sample preparation, imaging and data processing in Cryo-EM. a, Gel filtration chromatography of hHDAC6-CD1-2. **b**, SDS-PAGE analysis of the peak sample collected from **a**. **c**, Representative cryo-EM image of

hHDAC6-CD1-2 samples. **d**, 2D classification results of the final 109,995 particles used in local refinement. **e**, Front and side view of the hHDAC6-CD1-2 cryo-EM density map. **f**, GSFSC curve of the hHDAC6-CD1-2 cryo-EM density map. g, Start-up model predicted by AlphaFold2.

1

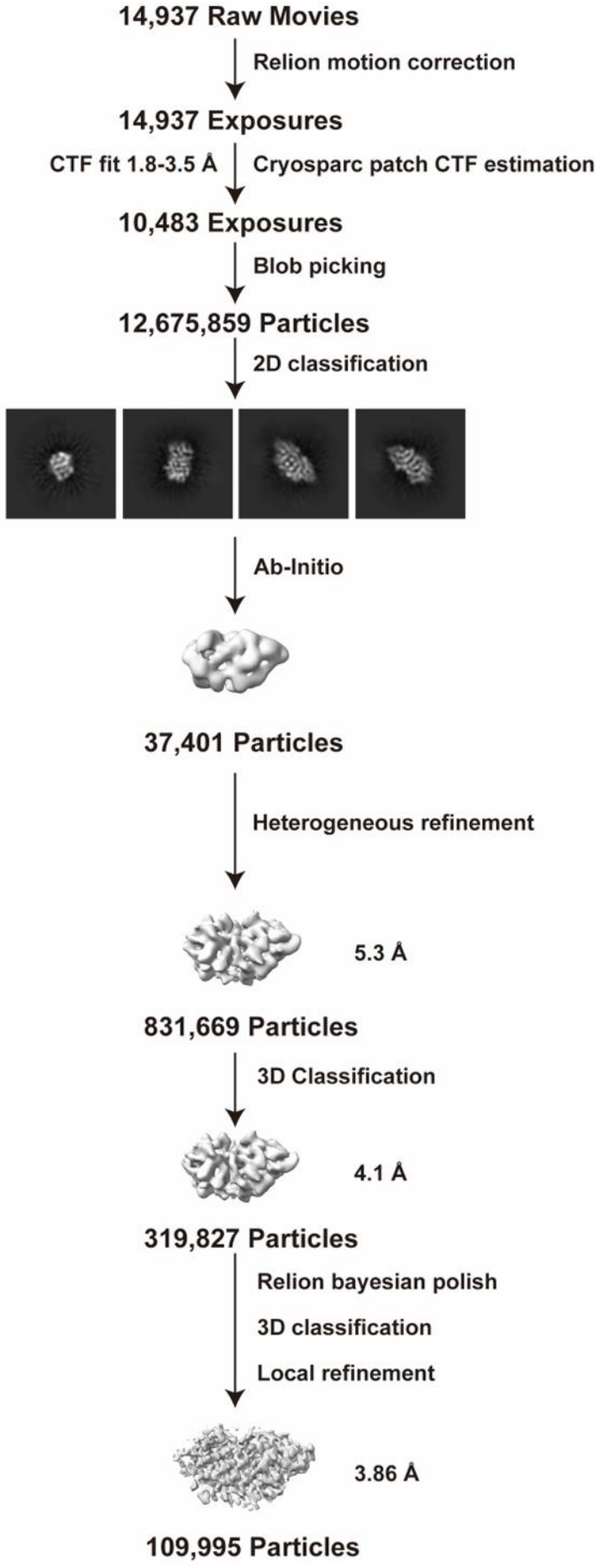

14,937 Raw Movies
Relion motion correction
14,937 Exposures
CTF fit 1.8-3.5 Å
Cryosparc patch CTF estimation
10,483 Exposures
Blob picking
12,675,859 Particles
2D classification
Ab-Initio
37,401 Particles
Heterogeneous refinement
5.3 Å
831,669 Particles
3D Classification
4.1 Å
319,827 Particles
Relion bayesian polish
3D classification
Local refinement
3.86 Å
109,995 Particles

Figure S23 (for Figure 4). Cryo-EM data processing and 3D reconstruction procedures.

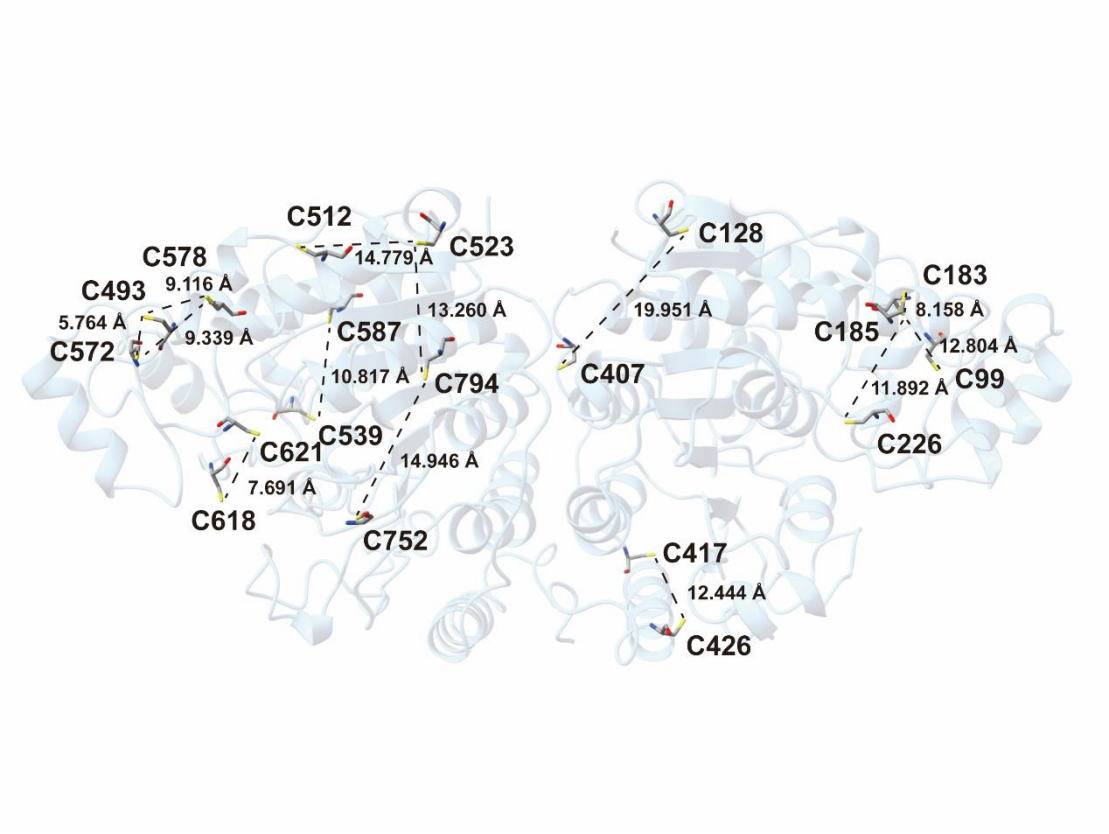


Figure S24 (for Figure 4). The distances of all adjacent cysteine residues in hHDAC6-CD1-2.

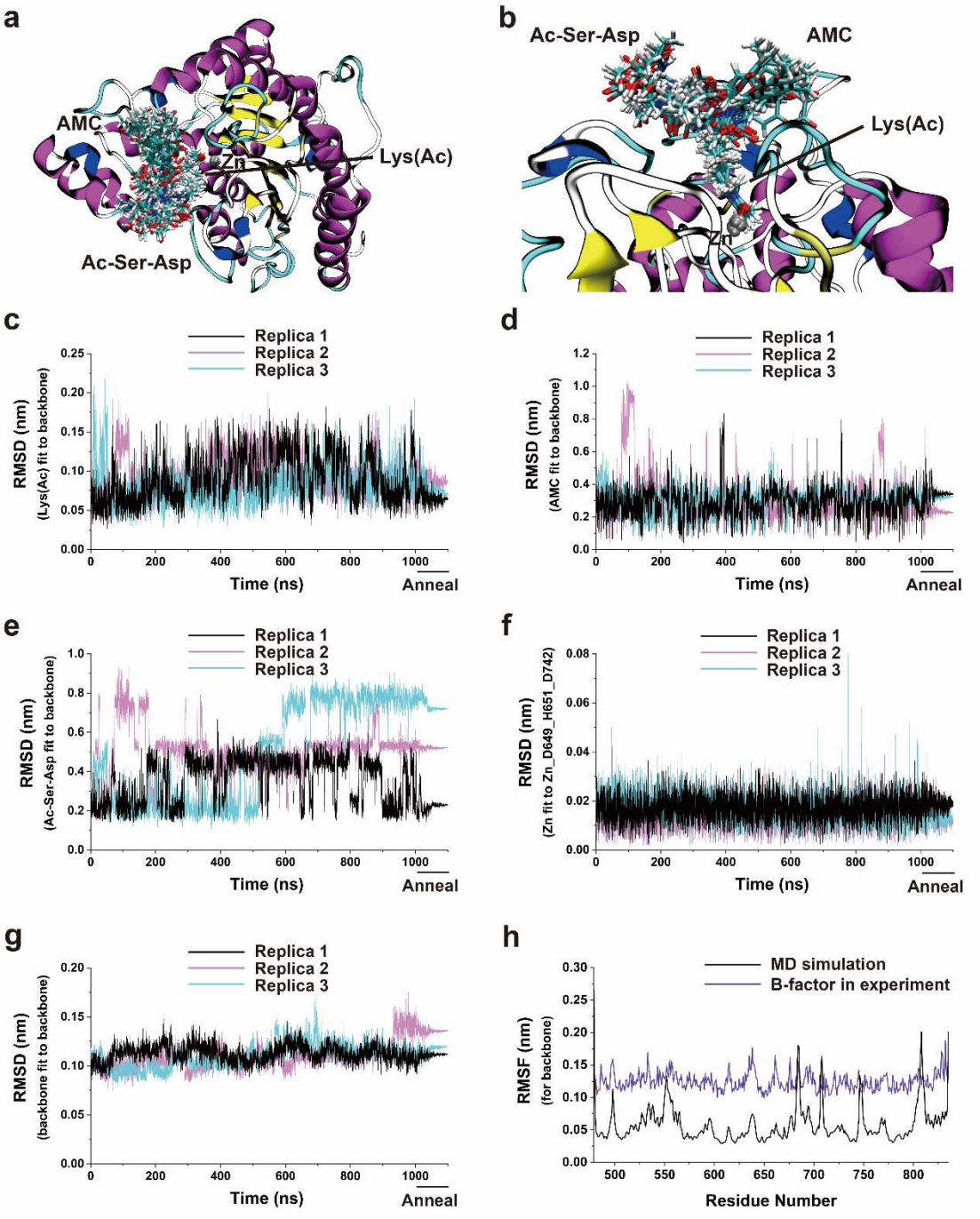

a
AMC
Zn
Lys(Ac)
Ac-Ser-Asp
b
Ac-Ser-Asp
AMC
Lys(Ac)
Zn
c
Replica 1
Replica 2
Replica 3
RMSD (nm)
(Lys(Ac) fit to backbone)
Time (ns)
Anneal
d
Replica 1
Replica 2
Replica 3
RMSD (nm)
(AMC fit to backbone)
Time (ns)
Anneal
e
Replica 1
Replica 2
Replica 3
RMSD (nm)
(Ac-Ser-Asp fit to backbone)
Time (ns)
Anneal
f
Replica 1
Replica 2
Replica 3
RMSD (nm)
(Zn fit to Zn_D649_H651_D742)
Time (ns)
Anneal
g
Replica 1
Replica 2
Replica 3
RMSD (nm)
(backbone fit to backbone)
Time (ns)
Anneal
h
MD simulation
B-factor in experiment
RMSF (nm)
(for backbone)
Residue Number

Figure S25. Molecular dynamics simulations of the formation of enzyme-substrate complex. a and **b**, Visualization of substrate (Ac-Ser-Asp-Lys (Ac)-AMC) movement during MD simulations yielding stable binding. Purple, α-helix; yellow, β-sheet; white, coil; cyan, turn; blue, 3-10 helix. **c-g**, Root-mean-square deviation (RMSD) of three segments of the substrate (**c - e**), Zn (**f**), and backbone (**g**) over MD simulations for 1000 ns and annealing from 310K to 0K for 100 ns, respectively. **h**, Root-mean-square fluctuations (RMSF) of the B-factor from crystallography data (PDB ID: 5EDU) and MD simulations for hHDAC6-CD2 backbone.

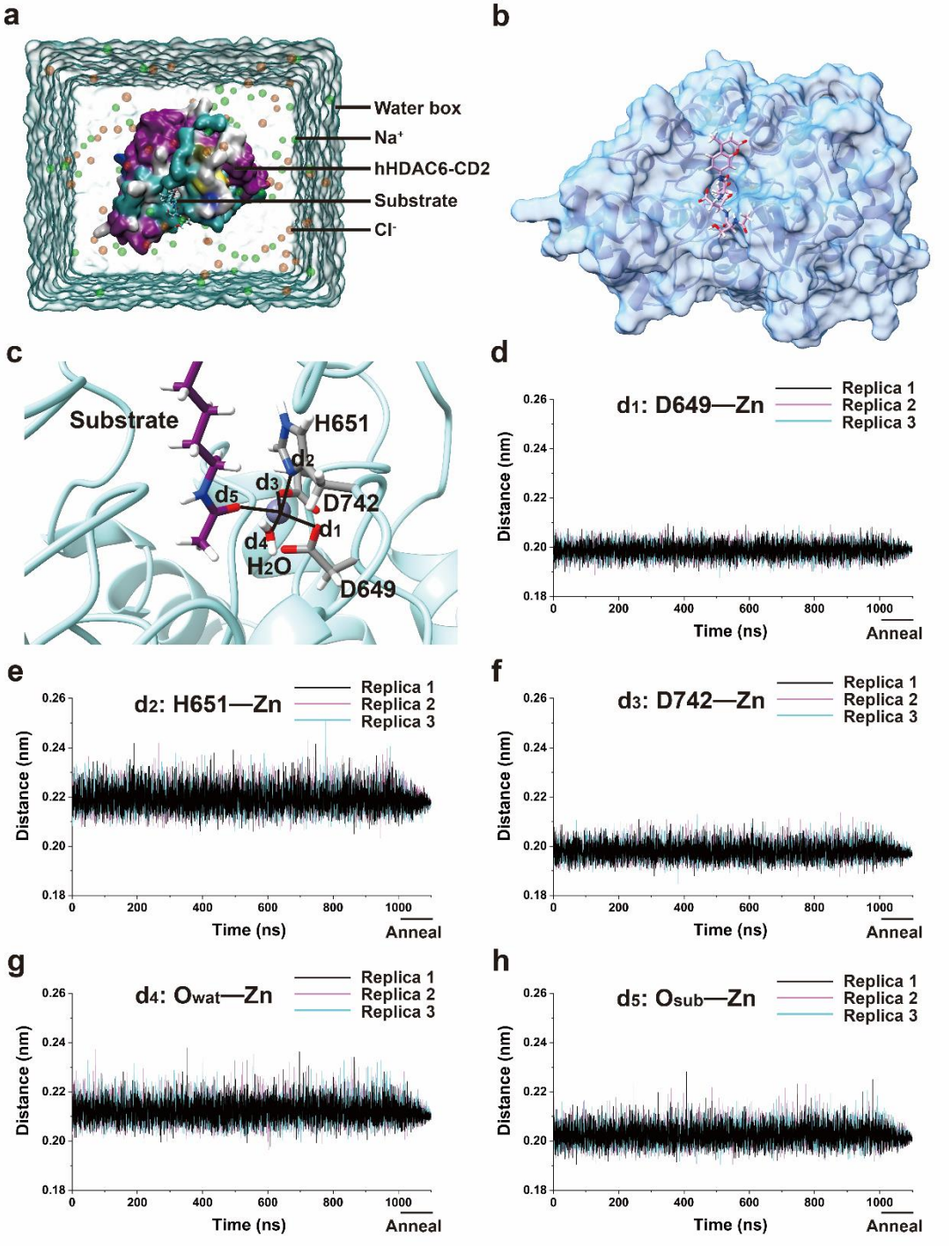
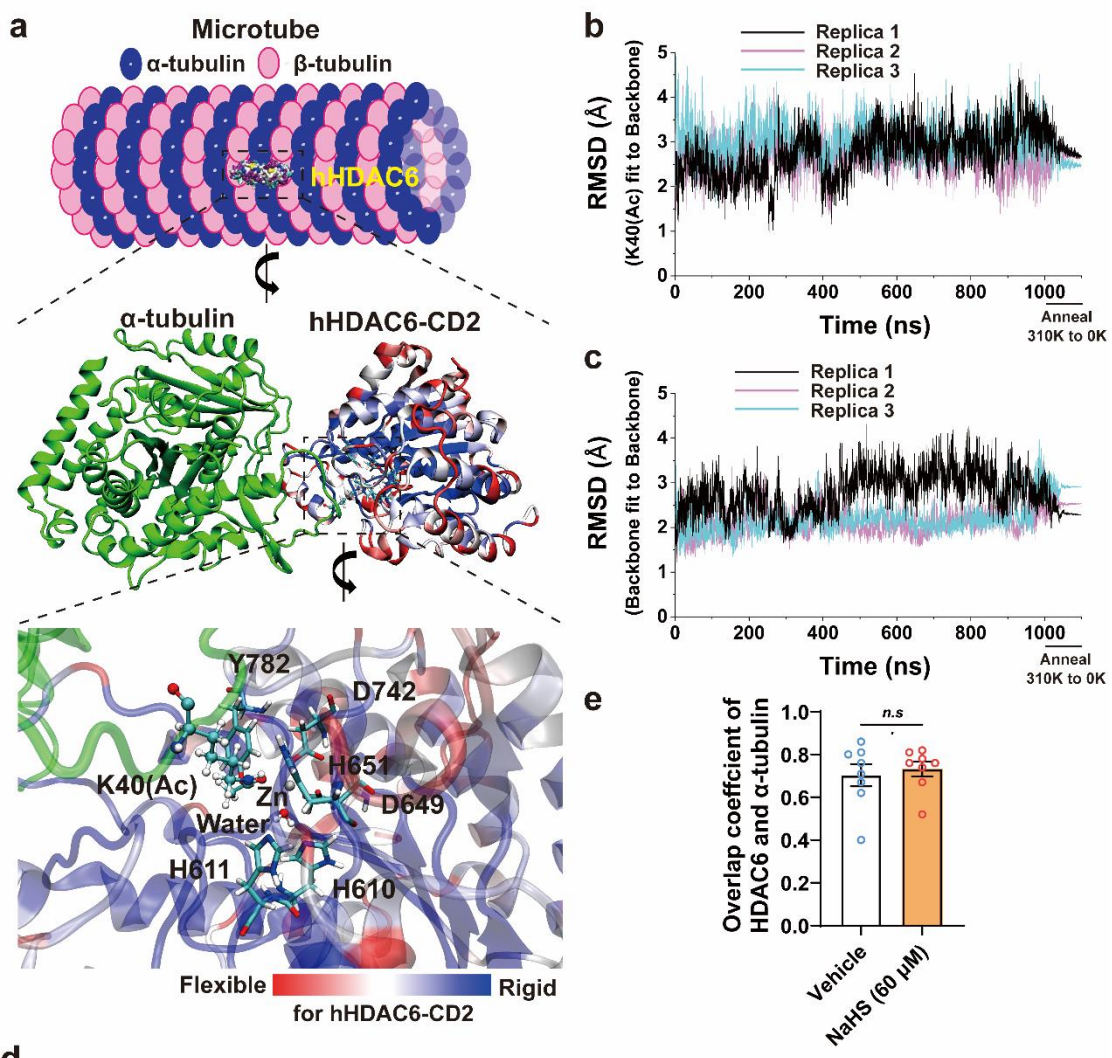

a
Water box
Na+
hHDAC6-CD2
Substrate
Cl-
b
c
Substrate
H651
d2
d3
d5
D742
d1
d4
H2O
D649
d
d1: D649—Zn
Replica 1
Replica 2
Replica 3
Distance (nm)
Time (ns)
Anneal
e
d2: H651—Zn
f
d3: D742—Zn
g
d4: Owat—Zn
h
d5: Osub—Zn

Figure S26 (for Figure S25). Molecular dynamics simulations showing five-fold coordination of the Zn^{2+} ion. a, The overall MD simulations systems of the substrate (Ac-Ser-Asp-Lys (Ac)-AMC) enzyme (hHDAC6-CD2) complex. Purple, α-helix; yellow, β-sheet; white, coil; cyan, turn; blue, 3-10 helix. **b**, Bird view of the MD simulations structures showing the substrate bound to the hHDAC6-CD2 active-site. **c-h**, Five-fold coordination of the Zn^{2+} ion over MD simulations for 1000 ns and annealing from 310K to 0K for 100 ns.


a
Microtube
α-tubulin
β-tubulin
hHDAC6
α-tubulin
hHDAC6-CD2
Y782
D742
H651
K40(Ac)
Zn
D649
Water
H611
H610
Flexible
Rigid
for hHDAC6-CD2
b
Replica 1
Replica 2
Replica 3
RMSD (Å)
(K40(Ac) fit to Backbone)
Time (ns)
Anneal
310K to 0K
c
Replica 1
Replica 2
Replica 3
RMSD (Å)
(Backbone fit to Backbone)
Time (ns)
Anneal
310K to 0K
e
Overlap coeffcient of
HDAC6 and α-tubulin
n.s
Vehicle
NaHS (60 μM)

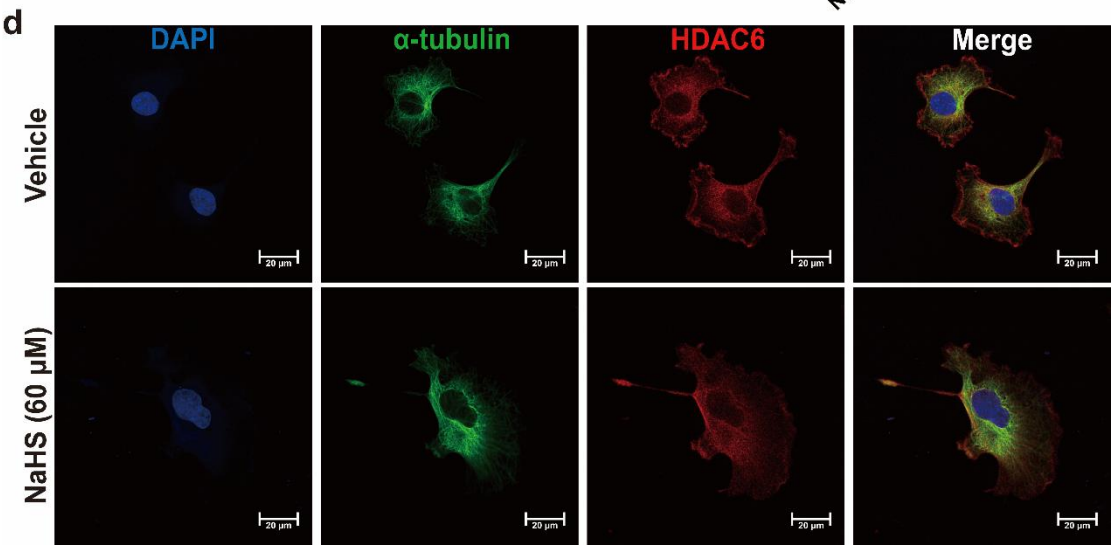

d
DAPI
α-tubulin
HDAC6
Merge
Vehicle
NaHS (60 μM)

Figure S27. Interaction between α-tubulin and hHDAC6. a, Molecular dynamics simulations showing the binding between acetylated α-tubulin (green) and hHDAC6-CD2. **b**, Root-mean-square deviation (RMSD) of K40(Ac) fit to the backbone of hHDAC6-CD2 over MD simulations for 1000 ns and annealing from 310K to 0K for 100 ns. **c**, RMSD of backbone fit to the backbone over MD simulations for 1000 ns and annealing from 310K to 0K for 100 ns. **d** and **e**, Representative photomicrographs showing the effects of NaHS treatment (60 μM) on co-localization of α-tubulin and HDAC6 in HUVECs, bar = 20 μm.

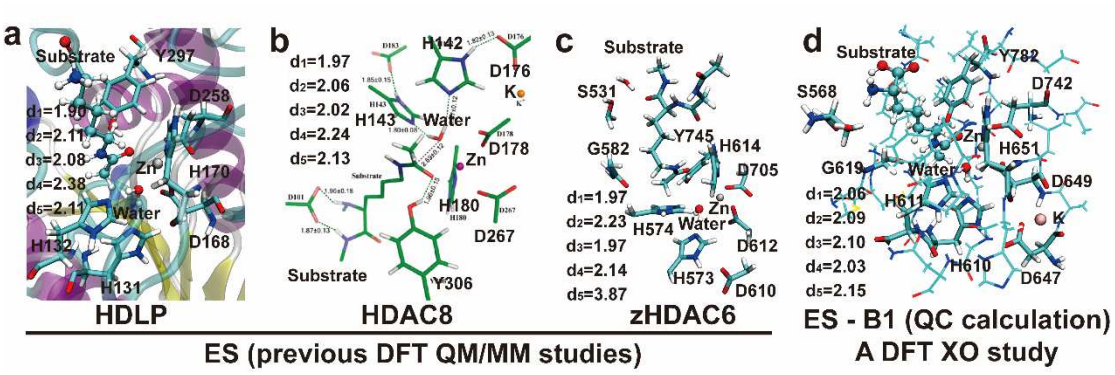


Figure S28. Comparison of the ES complex of the reported density functional theory (DFT) quantum mechanics/molecular mechanics (QM/MM) studies with current ES - B1 structure.

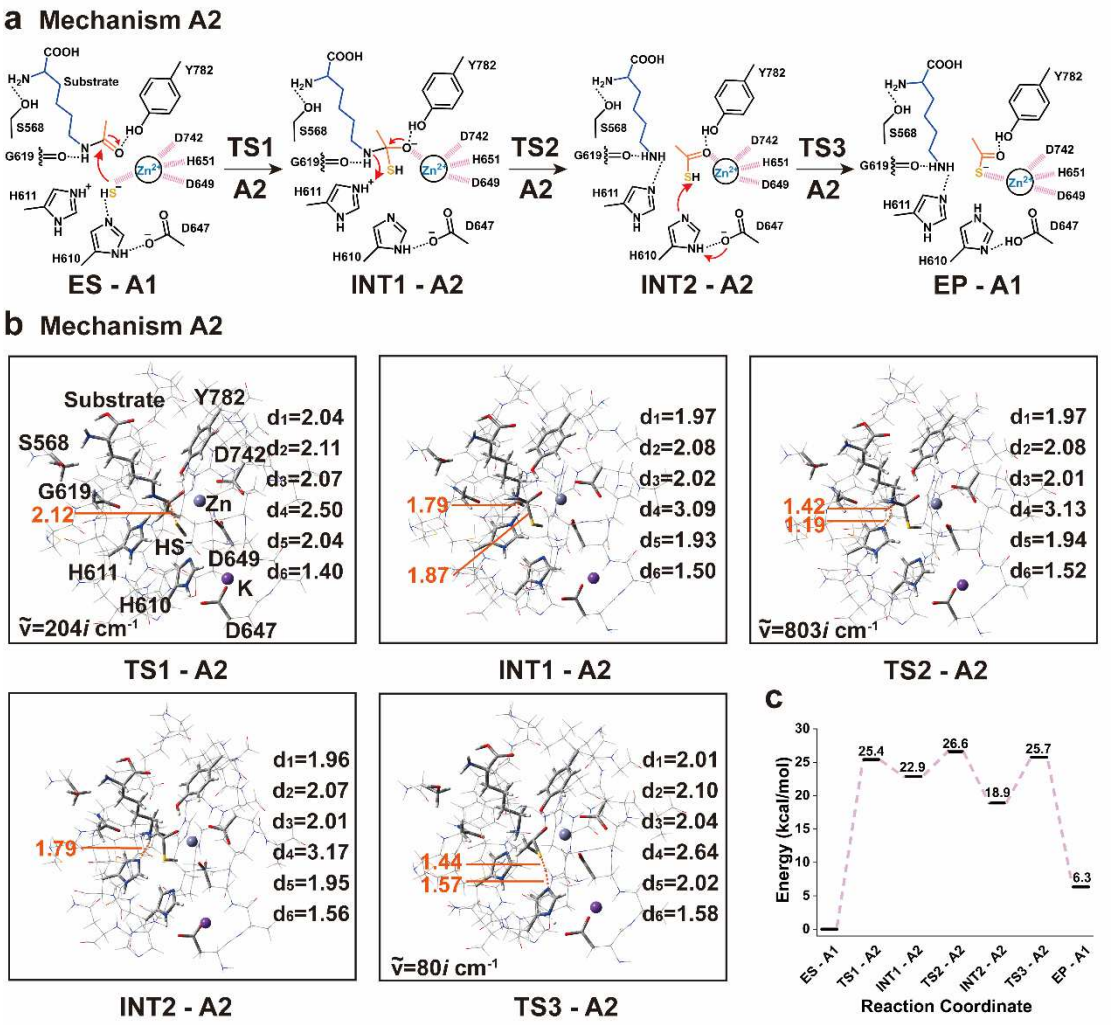


Figure S29 (for Figure 5). Quantum chemical calculations of HS^--mediated mechanisms of deacetylation reactions catalyzed by hHDAC6-CD2 (mechanism A2). a, Mechanism scheme of mechanism A2. The arrows indicate the directions of electron transfer. The dotted lines represent hydrogen bonds. The pink dashed lines represent coordination bonds. **b**, XO2 (ε = 4/B3LYP-D3(BJ)/6-31G(d,p)|6-311+G(d,p)|SDD:PM6-D3) optimized structures of ES, TSs, INTs, and EP in mechanism A2. d_1: distance between Zn^{2+} and D649; d_2: distance between Zn^{2+} and H651; d_3: distance between Zn^{2+} and D742; d_4: distance between Zn^{2+} and the S atom of the coordinated HS^-; d_5: distance between Zn^{2+} and the O atom of the acetyl group

of the substrate; d_6: the amide bond of the substrate. Atom distances were given in Å. One imaginary frequency of every TS was given at the bottom left in the corresponding panels. **c**, XO2 (ε = 4/MN15/def2-TZVP|SDD:PM6-D3) relative electronic energy profile for mechanism A2. ES, enzyme-substrate complex; TS, transition state; INT, intermediate; EP, enzyme-product complex.

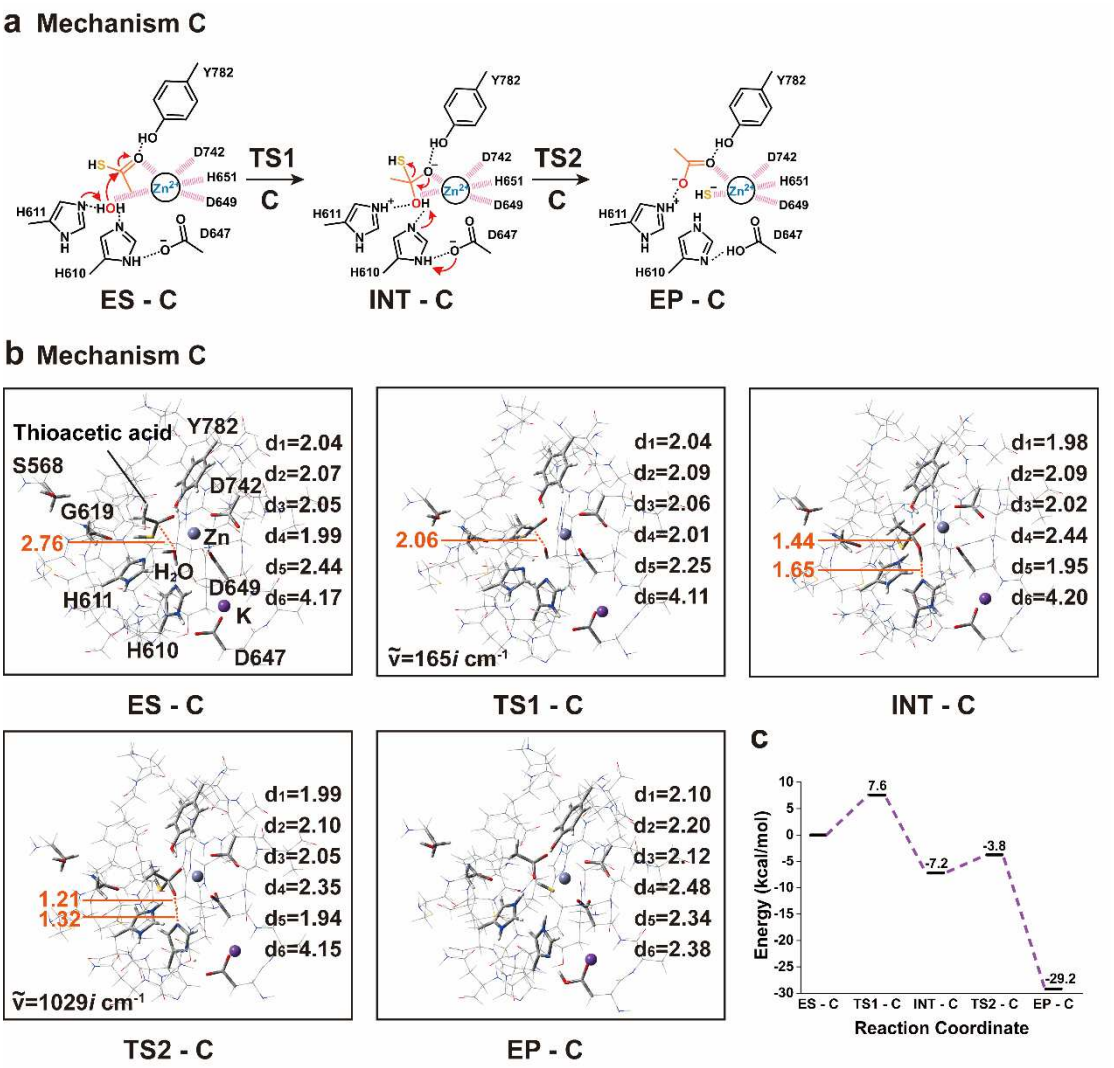


Figure S30 (for Figure 5). Quantum chemical mechanism underlying hydrolysis of thioacetic acid catalyzed by hHDAC6-CD2 coupled with recycle of H_2S (mechanism C). a, Mechanism scheme of mechanism C. The arrows indicate the

directions of electron transfer. The dotted lines represent hydrogen bonds. The pink dashed lines represent coordination bonds. **b**, XO2 (ε = 4/B3LYP-D3(BJ)/6-31G(d,p)|6-311+G(d,p)|SDD:PM6-D3) optimized structures of ES, TSs, INT, and EP in mechanism C. d_1: distance between Zn^{2+} and D649; d_2: distance between Zn^{2+} and H651; d_3: distance between Zn^{2+} and D742; d_4: distance between Zn^{2+} and the O atom of the coordinated H_2O; d_5: distance between Zn^{2+} and the O atom of the thioacetic acid; d_6: distance between Zn^{2+} and the S atom of the thioacetic acid. Atom distances were given in Å. One imaginary frequency of every TS was given at the bottom left in the corresponding panels. **c**, XO2 (ε = 4/MN15/def2-TZVP|SDD:PM6-D3) relative electronic energy profile for mechanism C. ES, enzyme-substrate complex; TS, transition state; INT, intermediate; EP, enzyme-product complex.

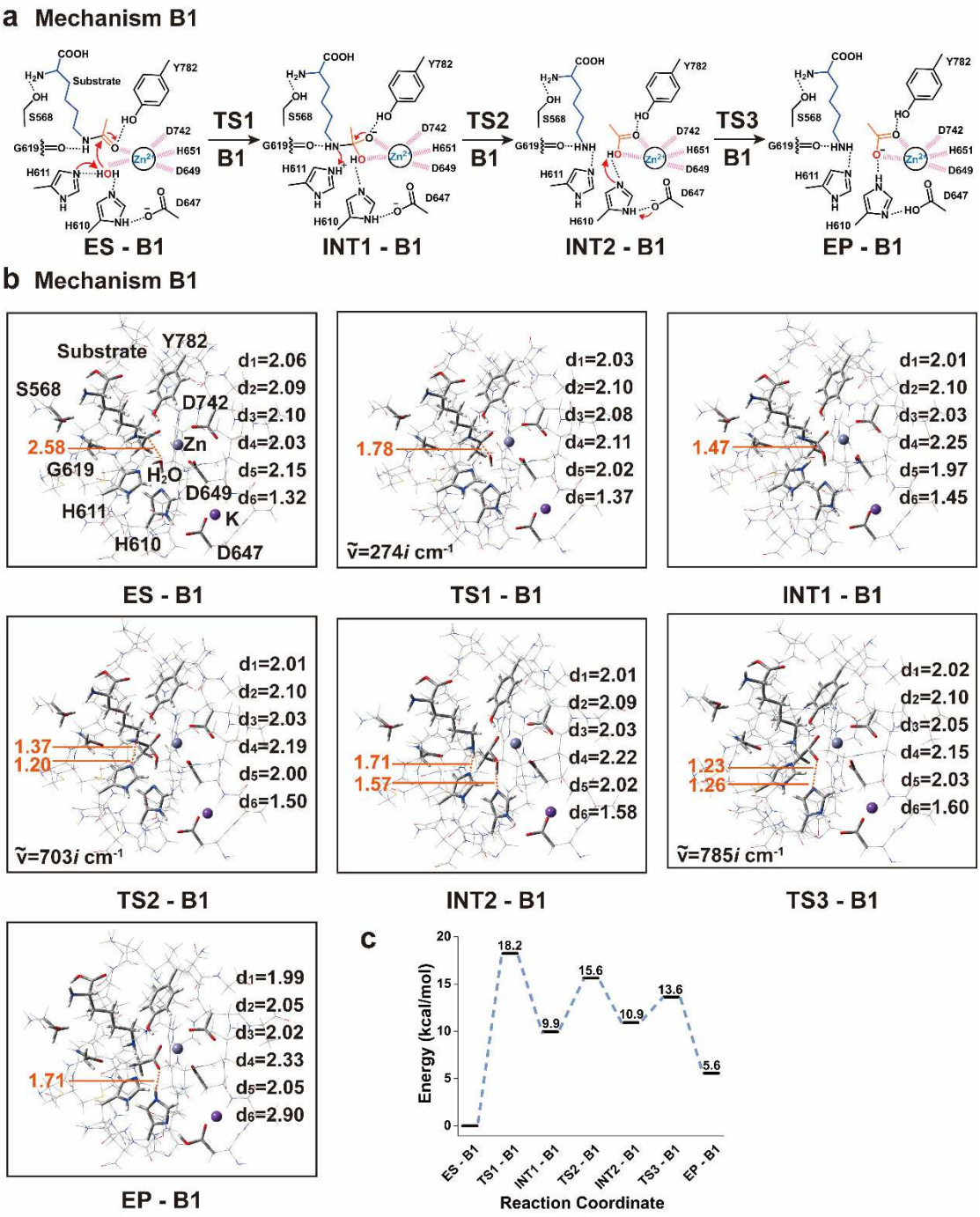


Figure S31 (for Figure 5). Quantum chemical calculations of canonical deacetylation reactions catalyzed by the hHDAC6-CD2 with its active-site coordinated with H_2O (mechanism B1). a, Mechanism scheme of mechanism B1. The arrows indicate the directions of electron transfer. The dotted lines represent

hydrogen bonds. The pink dashed lines represent coordination bonds. **b**, XO2 (ε = 4/B3LYP-D3(BJ)/6-31G(d,p)|6-311+G(d,p)|SDD:PM6-D3) optimized structures ES, TSs, INTs, and EP in mechanism B1. d_1: distance between Zn^{2+} and D649; d_2: distance between Zn^{2+} and H651; d_3: distance between Zn^{2+} and D742; d_4: distance between Zn^{2+} and the O atom of the coordinated H_2O; d_5: distance between Zn^{2+} and the O atom of the acetyl group of the substrate; d_6: the amide bond of the substrate. Atom distances were given in Å. One imaginary frequency of every TS was given at the bottom left in the corresponding panels. **c**, XO2 (ε = 4/MN15/def2-TZVP|SDD:PM6-D3) relative electronic energy profile for mechanism B1. ES, enzyme-substrate complex; TS, transition state; INT, intermediate; EP, enzyme-product complex.

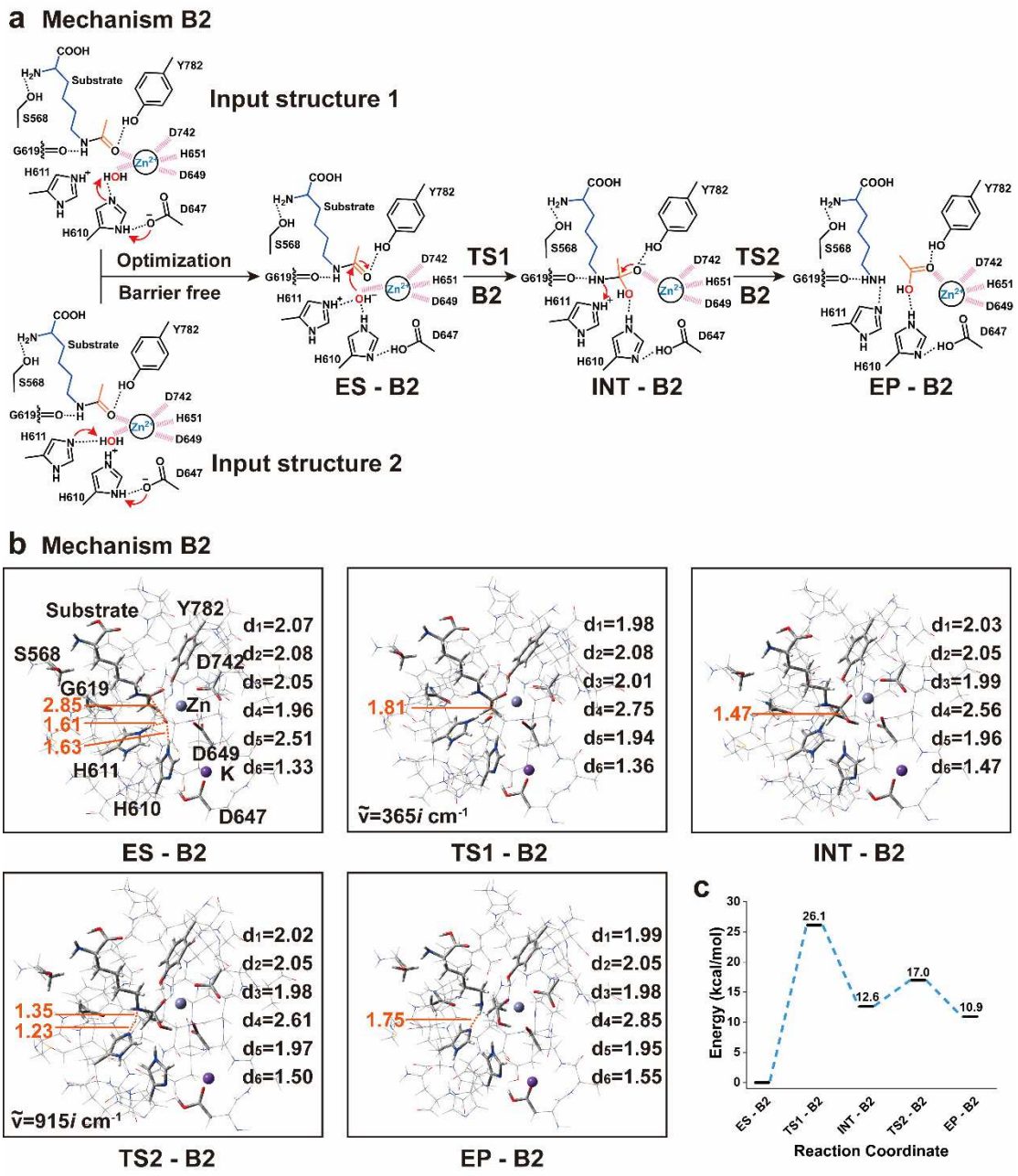


Figure S32 (for Figure 5). Quantum chemical calculations of canonical mechanisms of deacetylation reactions catalyzed by hHDAC6-CD2 with its active-site coordinated with H_2O at protonation status of HIP610/HID611 or HID610/HIP611 (mechanism B2). **a**, Mechanism scheme of mechanism B2. The arrows indicate the directions of electron transfer. The dotted lines represent hydrogen bonds. The pink dashed lines represent coordination bonds. **b**, XO2 (ε = 4/B3LYP-

D3(BJ)/6-31G(d,p)|6-311+G(d,p)|SDD:PM6-D3) optimized structures of ES, TSs, INT, and EP in mechanism B2. d_1: distance between Zn^{2+} and D649; d_2: distance between Zn^{2+} and H651; d_3: distance between Zn^{2+} and D742; d_4: distance between Zn^{2+} and the O atom of the coordinated H_2O; d_5: distance between Zn^{2+} and the O atom of the acetyl group of the substrate; d_6: the amide bond of the substrate. Atom distances were given in Å. One imaginary frequency of every TS was given at the bottom left in the corresponding panels. **c**, XO2 (ε = 4/MN15/def2-TZVP|SDD:PM6-D3) relative electronic energy profile for mechanism B2. ES, enzyme-substrate complex; TS, transition state; INT, intermediate; EP, enzyme-product complex.

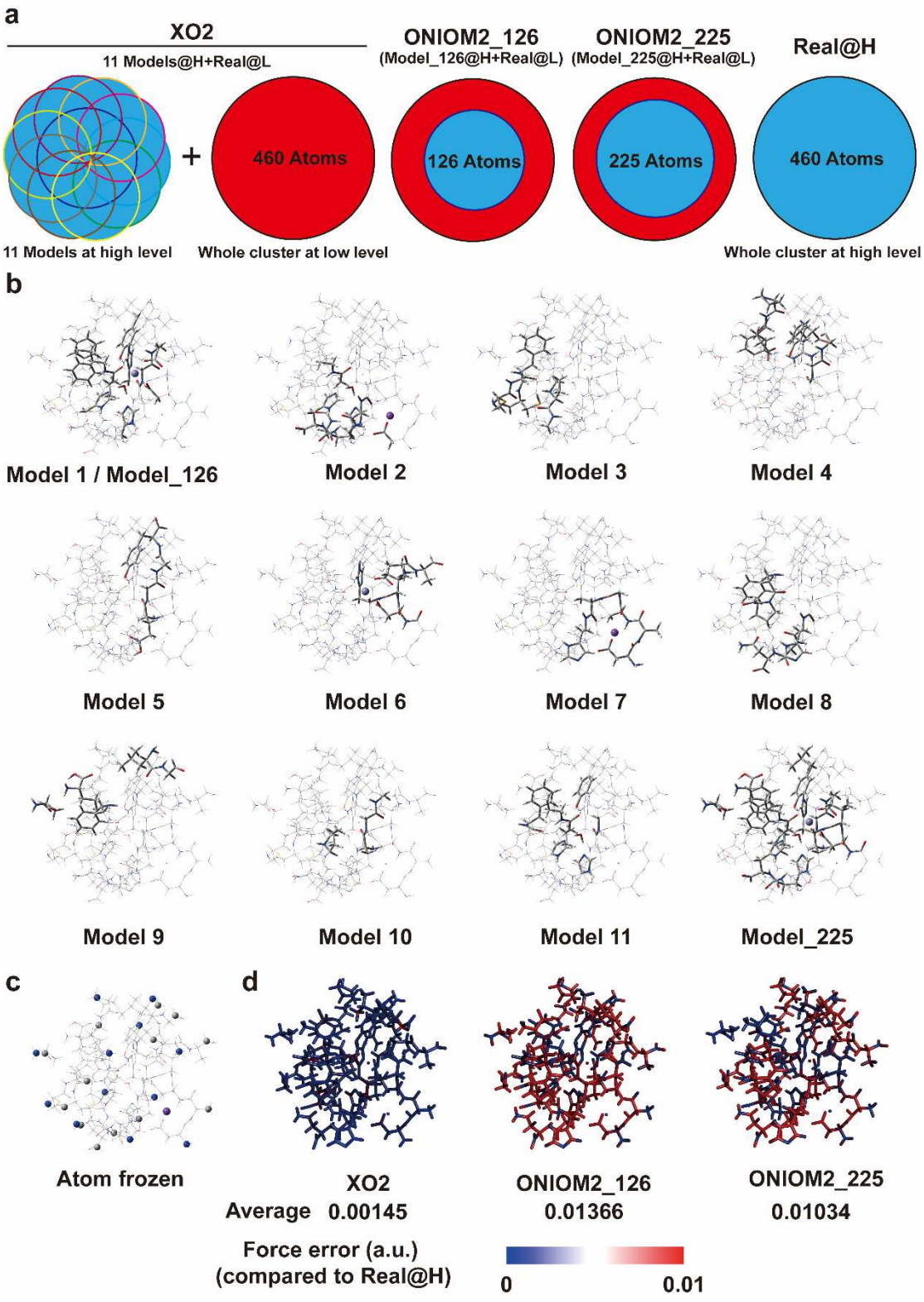

a
XO2
11 Models@H+Real@L
ONIOM2_126
(Model_126@H+Real@L)
ONIOM2_225
(Model_225@H+Real@L)
Real@H
460 Atoms
126 Atoms
225 Atoms
460 Atoms
11 Models at high level
Whole cluster at low level
Whole cluster at high level
b
Model 1 / Model_126
Model 2
Model 3
Model 4
Model 5
Model 6
Model 7
Model 8
Model 9
Model 10
Model 11
Model_225
c
Atom frozen
d
XO2
Average 0.00145
ONIOM2_126
0.01366
ONIOM2_225
0.01034
Force error (a.u.)
(compared to Real@H)
0
0.01

Figure S33 (for Figure 5 and Figure S29 – S32). The two-level eXtended ONIOM (XO) schemes. a, Comparison of the schemes of XO2, ONIOM2, and Real@H system. Red represents low level (PM6-D3) and blue represents high level (ε = 4/B3LYP-D3(BJ)/6-31G(d,p)|6-311+G(d,p)|SDD). **b**, Details of the schemes for XO2 and ONIOM2. **c**, Twenty-six atoms at the boundary of the cluster model systems were frozen to stabilize the active-site structure. **d**, Force error tests for XO2 schemes and ONIOM2 schemes as compared to the Real@H system.

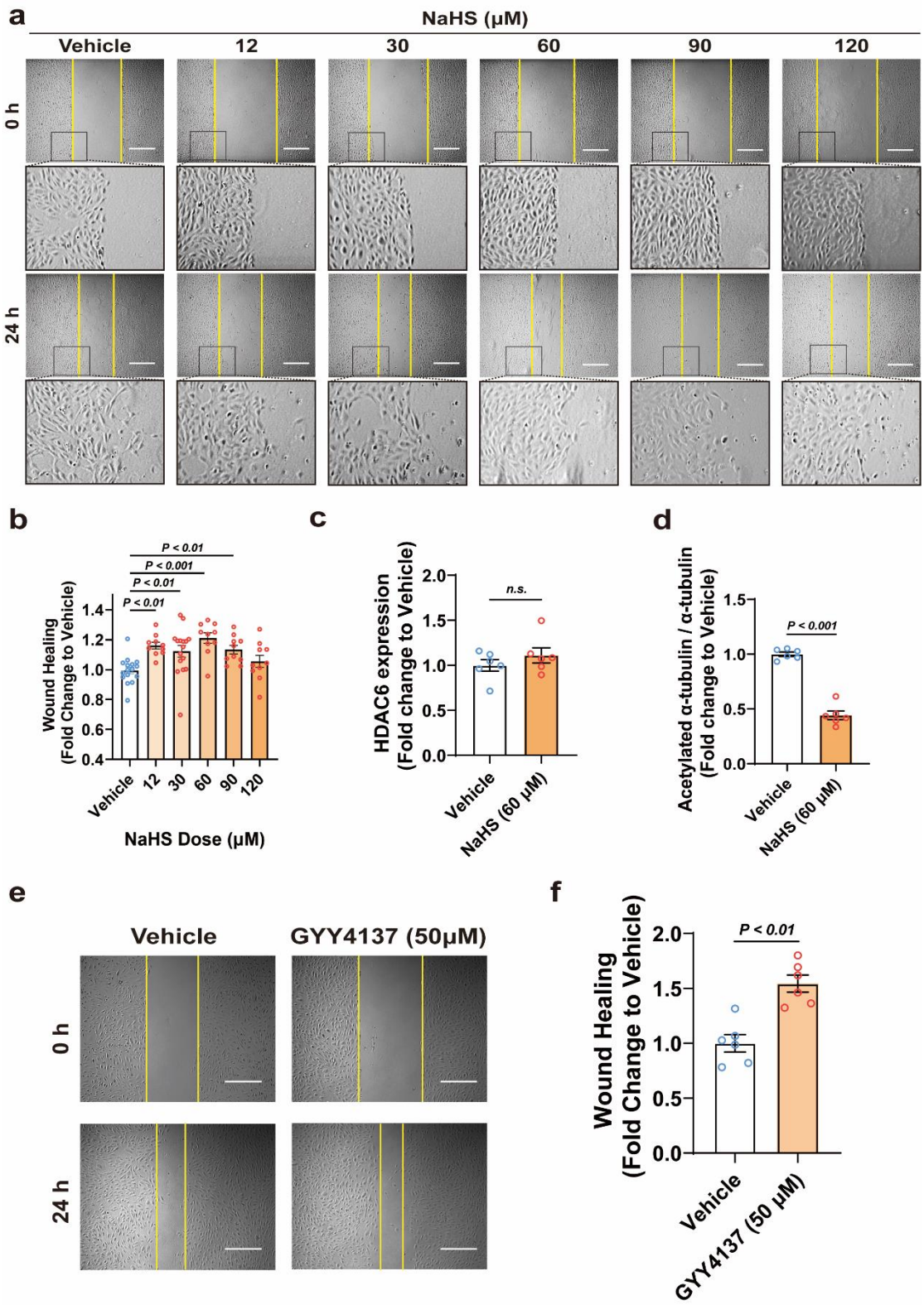


Figure S34 (for Figure 6). Exogenous H_2S treatment increased HDAC6 activity and promoted cell migration in HUVECs. **a** and **b**, Effects of NaHS treatment (12-

120 μM) on wound healing of HUVECs, bar = 200 μm, n = 10-16, black rectangular frame indicates the magnified area displayed below the photomicrographs. **c** and **d**, Acetylation of α-tubulin and HDAC6 in HUVECs treated with NaHS at 60 μM, n = 6. **e** and **f**, Effects of treatment with a slow releasing H_2S donor (GYY4137, 50 μM) on wound healing of HUVECs, bar = 200 μm, n = 6.

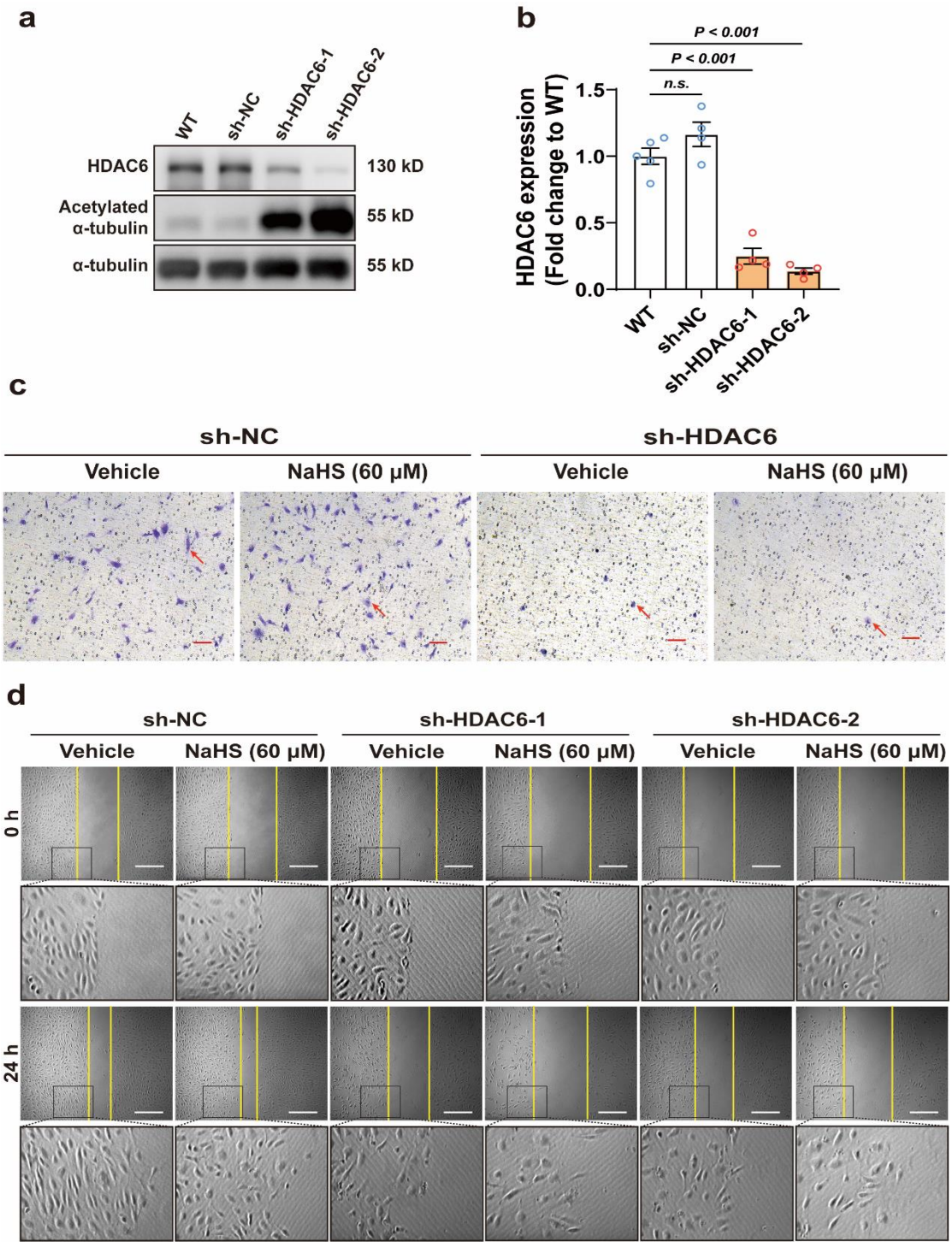


Figure S35 (for Figure 6). HDAC6 knockdown reduced cell migration in HUVECs.

a and **b**, Protein expression of HDAC6 and acetylated α-tubulin in WT HUVECs and HUVECs infected with sh-NC, sh-HDAC6-1, or sh-HDAC6-2 lentivirus, n = 4-5. **c**, Representative photomicrographs showing the effects of NaHS treatment (60 μM) on

the migration of HUVECs in a transwell model with or without knockdown of HDAC6, bar=100 μm, red arrow indicates the migrated cell. **d**, Representative photomicrographs showing the effects of NaHS treatment (60 μM) on wound healing of HUVECs infected with sh-NC, sh-HDAC6-1, or sh-HDAC6-2 lentivirus, bar = 200 μm, the black rectangular frame indicates the magnified area displayed below the photomicrographs. sh-NC, short hairpin RNA negative control.

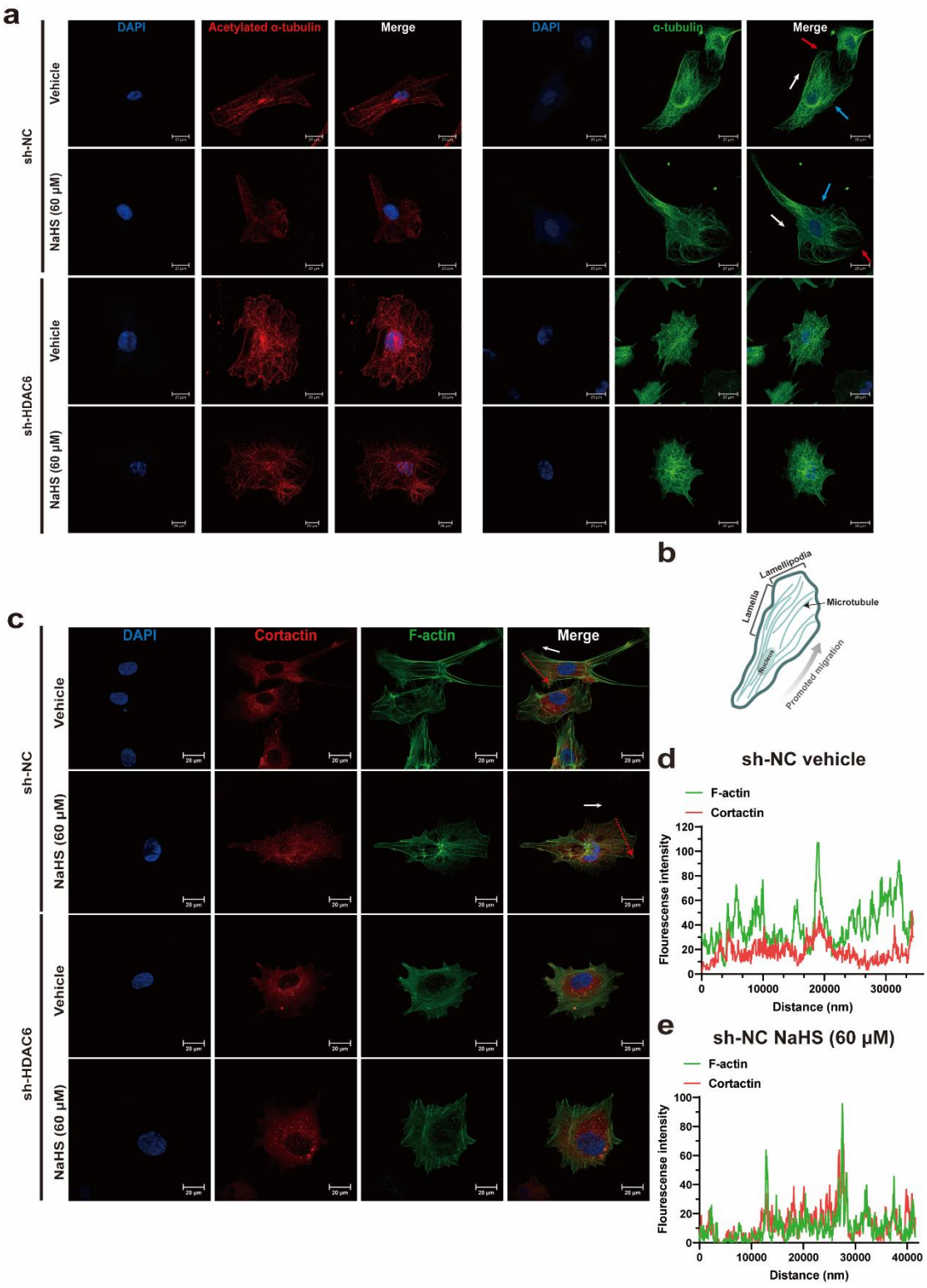

a
DAPI
Acetylated α-tubulin
Merge
DAPI
α-tubulin
Merge
sh-NC
Vehicle
NaHS (60 μM)
sh-HDAC6
Vehicle
NaHS (60 μM)
b
Lamellipodia
Lamella
Microtubule
Nucleus
Promoted migration
c
DAPI
Cortactin
F-actin
Merge
sh-NC
Vehicle
NaHS (60 μM)
sh-HDAC6
Vehicle
NaHS (60 μM)
d
sh-NC vehicle
F-actin
Cortactin
Flourescense intensity
Distance (nm)
e
sh-NC NaHS (60 μM)
F-actin
Cortactin
Flourescense intensity
Distance (nm)

Figure S36 (for Figure 6). Effects of exogenous H_2S on cytoskeletal proteins and cell morphology via HDAC6 in HUVECs. **a,** Representative photomicrographs showing the effects of NaHS treatment (60 μM) on the cellular distribution of acetylated alpha-tubulin and alpha-tubulin in HUVECs with or without knockdown of HDAC6 with white arrow indicates the direction of cell migration and red arrow indicates area of lamellipodia, blue arrow indicates area of lamella, respectively. bar = 20 μm. **b**, Cartoon image of a polarized endothelial cell. Arrow indicates the direction of polarization and migration. **c**, Representative photomicrographs showing the effects of NaHS treatment (60 μM) on co-localization of F-actin and Cortactin in HUVECS with or without HDAC6 knockdown, white arrow indicates the direction of cell migration, red dashed arrow indicates linear area chosen for colocalization analysis, bar = 20 μm. **d** and **e**, Bar graph showing the effects of NaHS treatment (60 μM) on co-localization of Cortactin (red) and F-actin (green) in the leading edge of the cells marked in **c**.

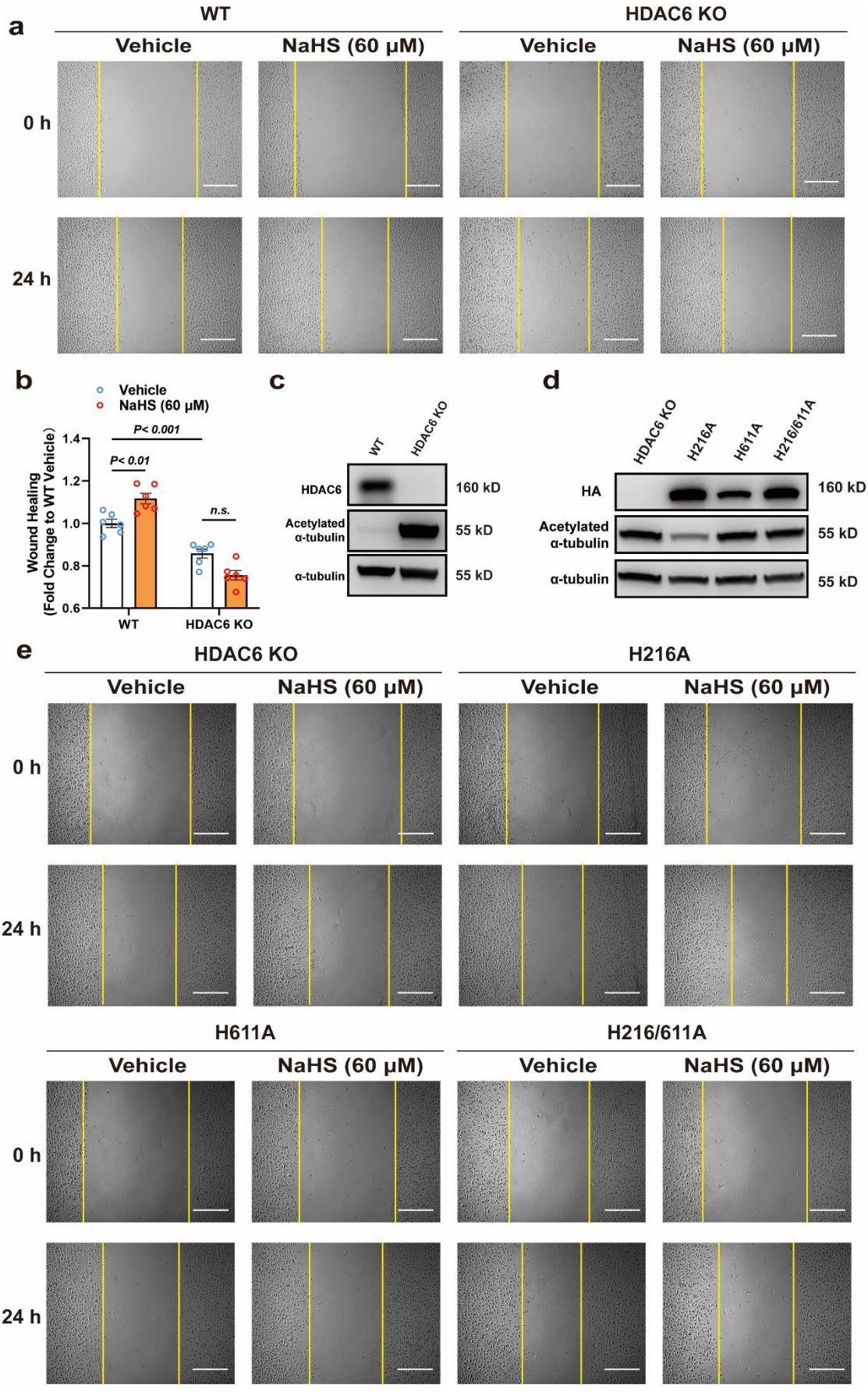

a
WT
HDAC6 KO
Vehicle
NaHS (60 μM)
Vehicle
NaHS (60 μM)
0 h
24 h
b
Vehicle
NaHS (60 μM)
P< 0.001
P< 0.01
n.s.
Wound Healing
(Fold Change to WT Vehicle)
1.4
1.2
1.0
0.8
0.6
WT
HDAC6 KO
c
WT
HDAC6 KO
HDAC6
160 kD
Acetylated
α-tubulin
55 kD
α-tubulin
55 kD
d
HDAC6 KO
H216A
H611A
H216/611A
HA
160 kD
Acetylated
α-tubulin
55 kD
α-tubulin
55 kD
e
HDAC6 KO
H216A
Vehicle
NaHS (60 μM)
Vehicle
NaHS (60 μM)
0 h
24 h
H611A
H216/611A
Vehicle
NaHS (60 μM)
Vehicle
NaHS (60 μM)
0 h
24 h

Figure S37 (for Figure 6). H_2S effects in promoting migration of vascular endothelial cells was dependent on the CD2 active site of hHDAC6. a and **b,** Effects of NaHS treatment (60 μM) on wound healing of WT and HDAC6 knockout EA.hy 926 endothelial cells, bar = 200 μm, n = 6. **c**, Representative western blot image showing the protein expression of HDAC6 and acetylated α-tubulin in WT and HDAC6 knock out EA.hy 926 endothelial cells. **d**, Representative western blot image showing the protein expression of HA tagged HDAC6 and acetylated α-tubulin in HDAC6 knock out EA.hy 926 endothelial cells overexpressed with either CD1 active-stie mutated HDAC6 (H216A), CD2 active-stie mutated HDAC6 (H611A) or CD1 and CD2 mutated HDAC6 (H216/611A). **e**, Representative photomicrographs showing the effects of NaHS treatment (60 μM) on wound healing of HDAC6 knock out EA.hy 926 endothelial cells overexpressed with either CD1 active-stie mutated HDAC6 (H216A), CD2 active-stie mutated HDAC6 (H611A) or CD1 and CD2 mutated HDAC6 (H216/611A), bar = 200 μm.

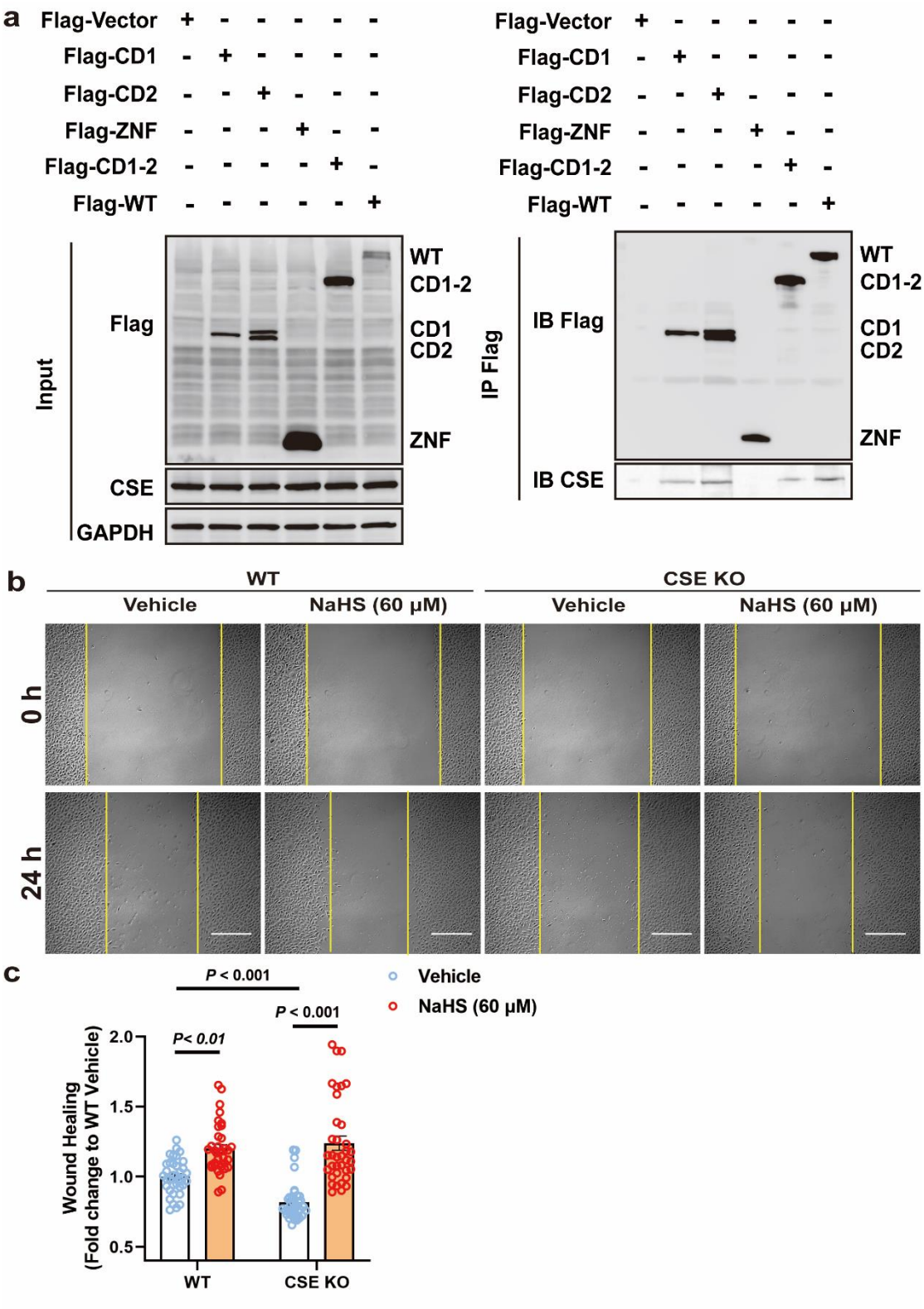

a
Flag-Vector
Flag-CD1
Flag-CD2
Flag-ZNF
Flag-CD1-2
Flag-WT
Input
Flag
CSE
GAPDH
WT
CD1-2
CD1
CD2
ZNF
IP Flag
IB Flag
IB CSE
b
WT
CSE KO
Vehicle
NaHS (60 μM)
0 h
24 h
c
P < 0.001
P < 0.001
P< 0.01
Vehicle
NaHS (60 μM)
Wound Healing
(Fold change to WT Vehicle)
2.0
1.5
1.0
0.5
WT
CSE KO

Figure S38 (for Figure 6). H_2S-generating enzyme, CSE, bound to the catalytic domains of HDAC6 and mediated migration of the endothelial cells. a, Representative image showing the co-immunoprecipitation of Flag-tagged different HDAC6 domains and CSE in EA.hy 926 endothelial cells. **b** and **c**, Effects of NaHS treatment (60 μM) on wound healing of WT and CSE knock out EA.hy 926 endothelial cells, bar = 200 μm, n = 36. CSE, Cystathionine Gamma-Lyase.

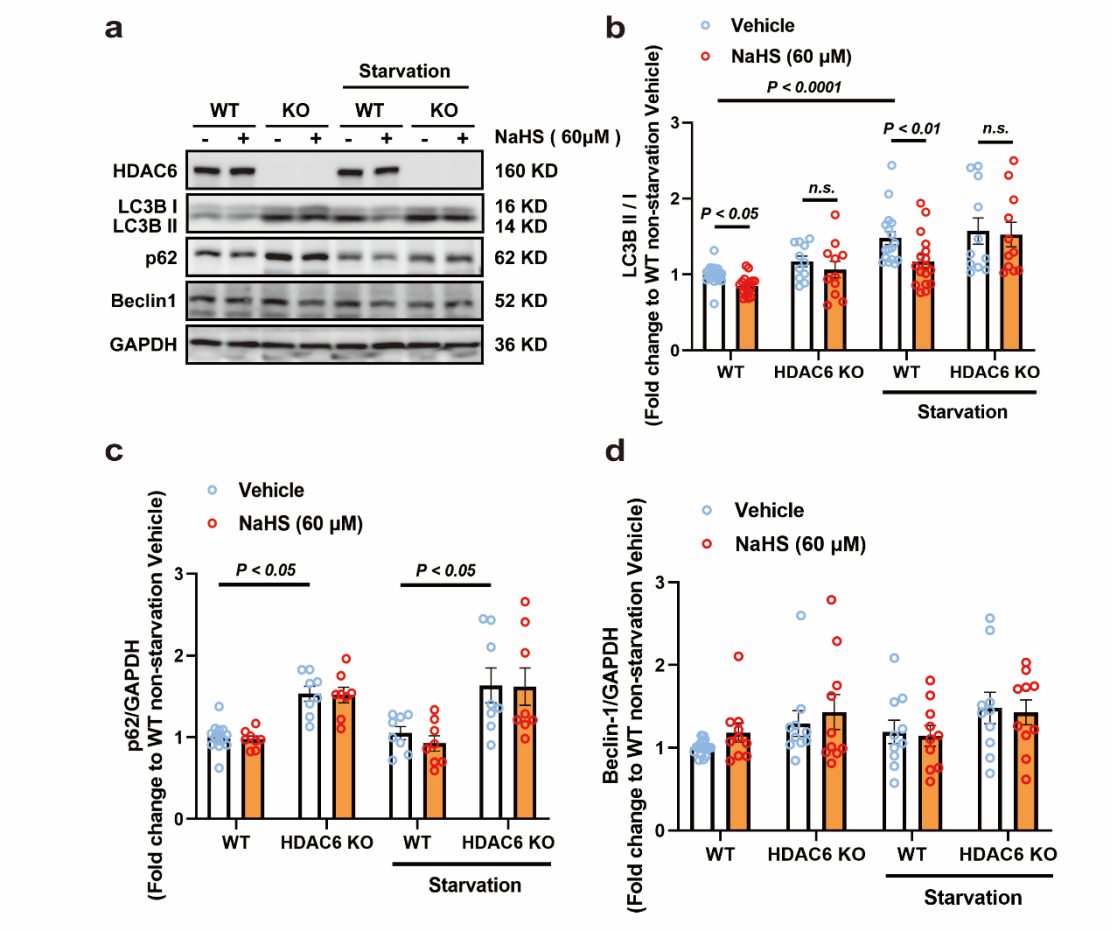


Figure S39. Effects of H_2S treatment on autophagy-related genes in serum-starved cells with or without knockout of HDAC6. a-d, Protein expression of HDAC6, LC3B II/I, p62 and Beclin-1 in WT and HDAC6 knockout EA.hy 926 cells starved of serum treated with NaHS at 60 μM, n = 8 - 25. LC3B, Microtubule-associated proteins 1A/1B light chain 3B.

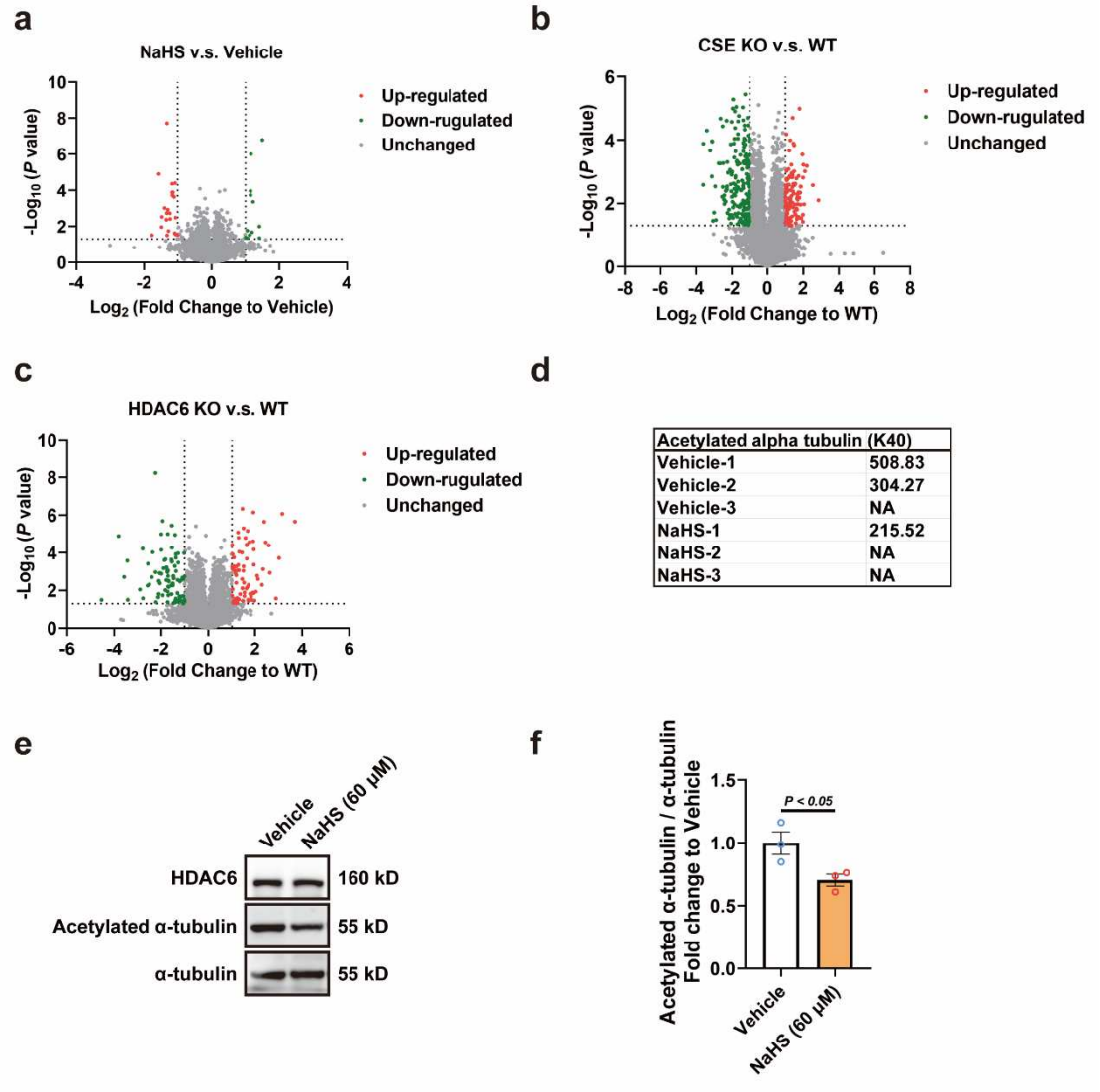


Figure S40 (for Figure 6). Acetylomics and proteomics in the cells treated with exogeneous H_2S, knocked-out of CSE or knocked-out of HDAC6. a, Volcano plot of proteomic analysis of the EA.hy 926 cells treated with NaHS (60 μM). n = 3. **b,** Volcano plot of proteomic analysis of the EA.hy 926 cells knocked out of CSE. n = 3. **c,** Volcano plot of proteomic analysis of the EA.hy 926 cells knocked out of HDAC6. n = 3. Cells with vehicle treatment (a) or WT cells (b and c) served as control. **d,** Raw mass spectrometry data showing the intensity of acetylated alpha-tubulin (K40) in EA.hy 926 cells treated with NaHS (60 μM). NA indicates the signals beneath the

detection limit (200.22). **e** and **f,** Western blot analysis showing acetylation of α-tubulin (K40) and expression of HDAC6 in EA.hy 926 cells treated with NaHS at 60 μM. n = 3.

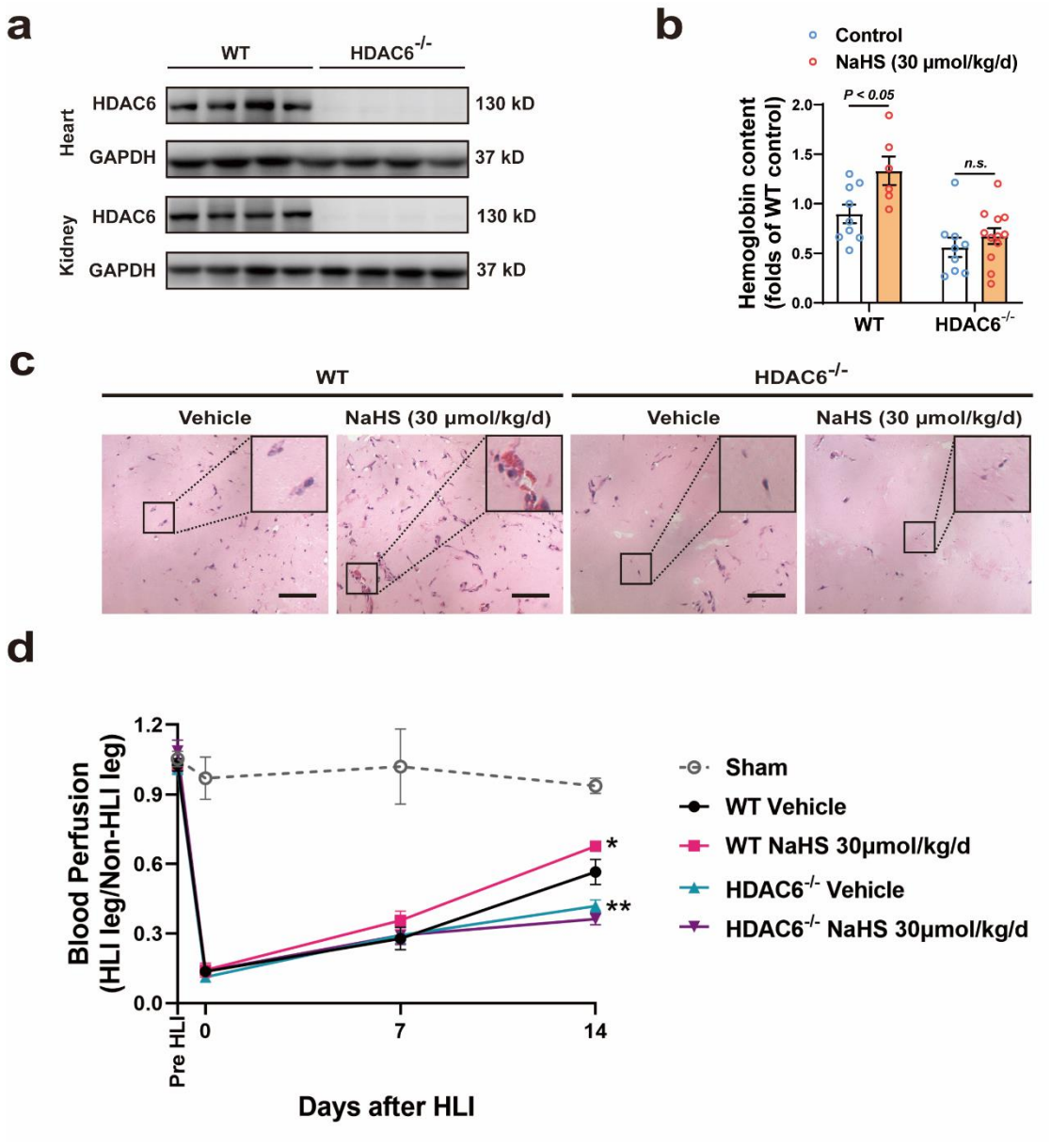


Figure S41 (for Figure 6). The proangiogenic effect of H_2S was blocked in HDAC6 knock out mice. **a**, Representative Western Blot image of HDAC6 expression in the heart and kidney tissues from WT and HDAC6$^{-/-}$ mice. **b**, Representative

photomicrographs showing hematoxylin-eosin stained Matrigel sections embedded in wild type or HDAC6$^{-/-}$ mice treated with vehicle or NaHS (30 μmol/kg/d). **c**, Hemoglobin content was increased in Matrigel plugs embedded in wild type mice treated with NaHS at a dose of 30 μmol/kg/d and this effect was blunted in HDAC6$^{-/-}$ mice. bar = 100 μm. n = 6-12. **d**, Bar graphs show that blood flow was significantly increased in injured limbs in wild type mice treated with NaHS at 30 μmol/kg/d for 14 days as compared with that of vehicle-treated mice (* $P < 0.05$, ** $P < 0.01$). This effect was blunted in HDAC6$^{-/-}$ mice, n = 5-18.

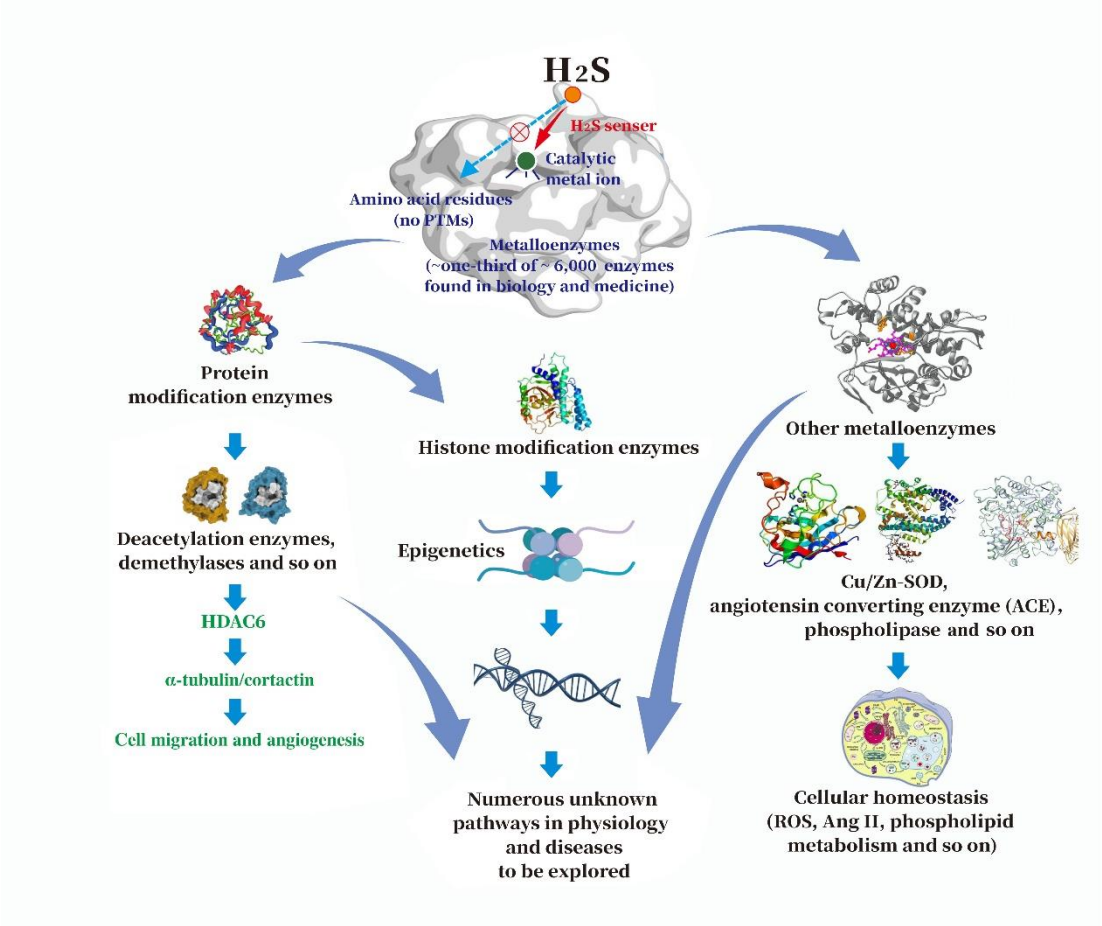


Figure S42. Schematic illustration of the prospect of the work. PTMs, post-translational modifications; Cu/Zn-SOD, Cu/Zn-Cu/Zn-Superoxide Dismutase; ROS, Reactive Oxygen Species; Ang II, Angiotensin II.

Legends for supplemental videos

Video S1. HS^- diffused into the active site tunnel in hHDAC6-CD2 and bound at the catalytic Zn^{2+} ion coupled with dissociation of a coordinated H_2O molecule as shown in molecular dynamics (MD) simulations.

Video S2. HS^- did not bind at the CD2 active site of hHDAC6-CD2 abolished of catalytic Zn^{2+} ion.

Supplementary data for quantum chemical calculations

Structures of minima and transition states, absolute energies in hartrees, force error test, atom frozen and eXtended ONIOM schemes.

Table 3-1. Steady-state kinetics of H_2S effects on a series of human HDAC6 constructs

Constructs	K_M (μM)	k_{cat} (s^{-1})	k_{cat} / K_M ($\mu M^{-1}s^{-1}$)
hHDAC6-WT	11.60 ± 3.9	0.045 ± 0.004	0.004 ± 0.001
hHDAC6-H216A	65.54 ± 13.8	0.065 ± 0.005	0.001 ± 0.00014
hHDAC6-CD1-2	62.96 ± 8.4	0.106 ± 0.005	0.002 ± 0.00016
hHDAC6-H611A	n.a.	n.a.	n.a.
hHDAC6-Y782F	n.a.	n.a.	n.a.
hHDAC6-H216/611A	n.a.	n.a.	n.a.

Data represent mean values ± SEM. n.a., no activity.

Table 3-2. Steady-state kinetics of the H_2S effects on hHDAC6 constructs and hSirt2 administrated with NaHS (12 μM)

WT	**K_M (μM)**	**k_{cat} (s^{-1})**	**k_{cat} / K_M ($\mu M^{-1}s^{-1}$)**
Vehicle	20.27 ± 7.8	0.056 ± 0.006	0.003 ± 0.001
NaHS (12 μM)	64.67 ± 19.3	0.45 ± 0.05	0.007 ± 0.001

H216A	**K_M (μM)**	**k_{cat} (s^{-1})**	**k_{cat} / K_M ($\mu M^{-1}s^{-1}$)**
Vehicle	65.54 ± 13.8	0.065 ± 0.005	0.001 ± 0.00014
NaHS (12 μM)	110.0 ± 33.6	0.513 ± 0.068	0.005 ± 0.001

H611A	**K_M (μM)**	**k_{cat} (s^{-1})**	**k_{cat} / K_M ($\mu M^{-1}s^{-1}$)**
Vehicle	n.a.	n.a.	n.a.
NaHS (12 μM)	n.a.	n.a.	n.a.

Sirt2	**K_M (μM)**	**k_{cat} (s^{-1})**	**k_{cat} / K_M ($\mu M^{-1}s^{-1}$)**

Vehicle	120.3 ± 20.3	0.005 ± 0.0004	(4.3 ± 0.64) *10^{-5}
NaHS (12 μM)	118.7 ± 28.8	0.005 ± 0.001	(4.3 ± 0.48) *10^{-5}

1

2

Table 4-1 human HDAC6 CD1-2 cryo-EM data collection and processing parameters

Data collection and processing	
Magnification	130,000x
Voltage (kV)	300
Electron exposure ($e^-/Å^2$)	50
Defocus range (μm)	0.5-3.5
Pixel size (Å)	0.466
Symmetry imposed	C1
Initial particle images (no.)	12,675,859
Final particle images (no.)	109,995
Map resolution (Å)	3.86
FSC threshold	0.143
Refinement	
Initial model used	AlphaFold2 Predicted
Model resolution	4.4
FSC threshold	0.5
Map sharpening *B* factor ($Å^2$)	224.5
Model composition	
Total amino acids	714
Total atoms	5517

B factors (Å^2)	
Overall	50
R.m.s deviations	
Bond lengths (Å)	0.004
Bond angles (°)	1.079
Validation	
MolProbity score	1.87
Clashscore	10.48
Poor rotamers (%)	0
Ramachandran plot	
Favored (%)	95.21
Allowed (%)	4.79
Disallowed (%)	0

1

2

Methods

Cell culture

Human umbilical vein endothelial cells (HUVECs) were obtained from Sciencell (San Die-go, USA) and cultured according to suppliers' instructions. HEK 293T cells and EA.hy 926 endothelial cells were obtained from ATCC (United States) and cultured in DMEM medium supplemented with 10% fetal bovine serum at 37℃ with 5% CO_2.

Lentivirus-mediated gene knockdown and overexpression

For HDAC6 knockdown, shRNA sequences 5' CCGGCCTCACTGATCAGGCCATATTCTCGAGAATATGGCCTGATCAGTGAGG TTTTTG 3' (shHDAC6-1) and 5' CCGGCGGTAATGGAACTCAGCACATCTCGAGATGTGCTGAGTTCCATTACC GTTTTTG 3' (shHDAC6-2) were cloned into a pLKO.1 vector. pLKO.1-TRC plasmid was used for negative control. In addition, a series of HDAC6 constructs were cloned by PCR from a cDNA library derived from the 293T cells. Point mutations were created by site-directed mutagenesis. The lentiviral vectors were co-transferred with lentivirus packaging vectors into the HEK293T cells to generate lentiviral particles, which were subsequently purified and quantified as previously described[64]. The HUVECs and EA.hy 926 cells were infected with a serial amount of lentivirus and selected in the presence of 2 μg/ml puromycin for 2 days.

CRISPR-mediated gene knockout

Single guide RNA sequence 5' ACATGATCCGCAAGATGCGC 3' targeting the human HDAC6 gene and 5′-AGGCCACAGTGATGTTGTAA-3′ targeting the human CSE gene were cloned into a LentiCRISPRv2 vector using ligation-dependent cloning[65]. HEK 293T cells and EA.hy 926 endothelial cells were infected with this virus and selected in the presence of puromycin (2 μg/ml) for 2 days. Survived cells were diluted and cultured for single clone screening. The corresponding knockout clones were passaged for subsequent experiments.

The wound healing assay

The endothelial cells were seeded into 6-well plates and cultured till 100% confluence, which were then scratched with a plastic pipette. Detached cells were washed away with PBS. Images were taken at 0 h and 24 h after scratching, the wound closure area was calculated using the software ImageJ.

The transwell assay

The transwell migration assays were performed as previously described with slight modification[66,67]. The migrated cells were stained with crystal violet staining solution and photographed for visual counting.

Tube formation assay

Growth factor reduced matrigel (Sigma Merk, USA) was plated evenly in a 24-

well plate and incubated at 37˚C for 60 min before seeding the HUVECs. Fifty thousand cells were seeded to each well and incubated for sixteen hours before photographing. Tube length and branching points were quantified using the Image J software.

Immunoprecipitation

A series of Flag-tagged HDAC6 constructs including different domains were constructed into a pCDH vector which was used to infect EA.hy 926 cells via lentiviral transduction. The infected cells were collected and lysed using a native cell lysis buffer (50mM HEPES, 150 mM NaCl, 0.5 Triton X-100, pH 7.5). The lysate was centrifuged, and the supernatant was incubated with anti-Flag beads for 2 hours. After washing three time, 2× SDS loading buffer was added, followed by heating at 95 °C for 5 minutes. The samples were then analyzed using Western Blot analysis.

Serum-starvation induced cell autophagy

EA.hy 926 cells were first seeded in growth medium (DMEM-HG containing 10% FBS) for 48 hours. Then cells were washed twice with PBS to remove any residual serum. Subsequently, the medium was replaced with low-serum medium (DMEM-HG containing 0.1% FBS) to induce starvation. This serum-starvation condition was maintained for 24 hours to induce autophagy. The cells were then collected and subjected to Western blot analysis to examine expressions of autophagy-related genes including LC3B I, LC3B II, Beclin-1 and p62.

Immunofluorescence staining

The cells were seeded into the glass-bottom culture dishes, fixed with 4% paraformaldehyde, and permeabilized with 0.1% Trition X-100. F-actin was stained with FITC-labeled phalloidin (Thermo Fisher, USA). Acetylated α-tubulin, α-tubulin, and cortactin were stained using cooresponding primary antibodies and fluorescent secondary antibodies (Cell Signalling Technology, USA). Confocal laser scanning microscopy was carried out using a LSM710 confocal microscope (Zeiss, Germany).

Angiogenesis *in vivo*: Matrigel plug assay

Customized HDAC6$^{-/-}$ mice were constructed by SiDanSai Biotechnolog (Shanghai, China). C57 BL/6 (wild type or HDAC6$^{-/-}$) female mice were anesthetized by isoflurane inhalation and injected subcutaneously with 500 μl Matrigel. NaHS was injected intraperitoneally at a dosage of 30 μmol/L/kg/d for 7 days. In the vehicle groups, saline was injected instead of the NaHS solution.

Seven days after embedment, the Matrigel plugs were recovered by careful dissection in mice with anesthesia, and then the mice were sacrificed by cervical dislocation. Matrigel plugs were paraffin embedded and the sections (5 μm) were stained with hematoxylin–eosin. Angiogenesis in Matrigel in mice was assessed by morphological analysis and quantification of the hemoglobin content. Hemoglobin quantification was performed by the tetramethylbenzidine method. The investigation conformed to the “Guide for the Care and Use of Laboratory Animals” published by the National Institutes of Health (NIH publication, revised 2011) of the United States

and was approved by the local ethic committee of experimental research (Authorization code: 20160225-054).

Murine hindlimb ischemia model in mice

C57 BL/6 (wild type or HDAC6$^{-/-}$) mice underwent unilateral femoral artery ligation as described[52]. Briefly, following anesthesia with sodium pentobarbital (50 mg/kg i.p.), the left femoral artery was exposed under a dissection microscope. The proximal femoral artery and the distal portion of the saphenous artery were ligated and arteriotomy was performed. Sham operation was performed according to given surgical procedures except femoral artery ligation. Blood flow in the ischemic/sham-operated hindlimbs was monitored using a MoorLDI2-2l laser Doppler imaging system (Moor Instruments, Devon, UK) before the surgery and at 0, 7 and 14 days after surgery as well. Mice were euthanized and maintained at 37℃ on a heating plate to minimize temperature variation. Final blood flow values were expressed as the ratios of ischemic to non-ischemic hindlimb perfusion. All animal experimental procedures were performed according to the Guide for the Care and Use of Laboratory Animals of the National Institutes of Health (NIH) of the United States and approved by the Ethics Committee of Experimental Research, Fudan University Shanghai Medical College. IACUC Animal Project Numbers (APN): 20210226-003, 20180302-045 and 20240229-014.

Acetylomics and proteomics analysis

For each acetylomics analysis sample, 1 ×10^7 cells were lysed using ultrasonication

in SDT lysis buffer (100 mM Tris-HCl, pH 7.6, 2% SDS, 100 mM DTT), followed by centrifugation to clear the lysate. The extracted protein was reduced by adding DTT (1 M) to a final concentration of 100 mM and incubated at 37°C for 1 hour. Subsequently, the sample was added with IAA (0.8 M) to a final concentration of 50 mM and incubated at room temperature in dark for 30 minutes. The sample was then treated with UA buffer (8 M urea, 150 mM Tris-HCl, pH 8.0), followed by precipitation with cold acetone at -20°C overnight. The sample was centrifuged at 12,000g for 10 minutes at 4°C. The pellet was rinsed with cold acetone, centrifuged, and air-dried. The pellet was resuspended in 100 μL of UA buffer (8 M), diluted with NH_4HCO_3 (50 mM) to a final UA concentration below 1 M. Trypsin was added according to a trypsin-to-protein mass ratio of 1:25, followed by an incubation at 37°C for 16 - 18 hours. The digestion reaction was terminated by acidification with 100% TFA. The sample was desalted using Sep-PAK (Waters, Massachusetts, US) and subsequently lyophilized.

For proteomics analysis, peptides were generated by digesting the cell lysates and purified as mentioned above. The lyophilized peptides were then enriched for acetylation using the PTMScan® Acetyl-Lysine Motif (Ac-K) Kit (Cell Signaling Technology, Danvers, MA, USA). Briefly, the sample was resuspended in 1×IAP solution and incubated with PTMScan® Acetyl-Lysine Motif (Ac-K) Antibody Bead Conjugate for 2 hours. The beads were rinsed with 1×IAP solution and ultrapure water. The bound acetylated peptides were eluted with 0.15% TFA. The eluted peptides were collected, concentrated under vacuum, and further purified using C18 tips (Thermo Scientific, Waltham, MA, USA).

The lyophilized peptides were resuspended in 10 μL of 0.1% FA, and injected for chromatographic separation using the Vanquish Neo UHPLC system (Thermo Scientific, Waltham, MA, USA). The mobile phases were: A, 0.1% formic acid in water; and B, 0.1% formic acid in acetonitrile (80% acetonitrile). The column was equilibrated with 96% mobile phase A. Following sample injection onto the Trap Column (PepMap Neo 5 μm C18 300 μm × 5 mm, Thermo Scientific, Waltham, MA), the peptides were separated on the analytical column (μPAC Neo High Throughput Column, Thermo Scientific, Waltham, MA, USA) by gradient elution. The liquid chromatography gradient was as follows: 0–0.1 min, B increased from 4% to 8%; 0.1–1.2 min, B increased from 8% to 10%; 1.2–11.2 min, B increased from 10% to 28%; 11.2–13.5 min, B increased from 28% to 45%; and 13.5–15 min, B was held at 99%. After separation, the peptides were analyzed using DIA (data-independent acquisition) mass spectrometry with an Orbitrap Astral mass spectrometer (Thermo Scientific, Waltham, MA, USA). The analysis was conducted for 15 minutes with a spray voltage of 2.2 kV in positive ion mode. The parent ion scan range was 380–980 m/z, with a resolution of 240,000 for the first-stage MS, AGC target of 500%, and a maximum ion trap fill time of 3 ms. The second-stage MS resolution was 80,000, with an AGC target of 500%, a maximum ion trap fill time of 3 ms, RF-lens at 40%, MS2 activation type as HCD, isolation window of 2 Th, normalized collision energy of 25%, and a cycle time of 0.6 seconds.

Raw data were processed using Spectronaut (version 18, Biognosys AG), and the spectra were searched against the human UniprotKB protein sequence database. The

data were visualized using GraphPad Prism 8.0.

Protein expression and purification

The full-length homo sapien HDAC6 and Sirt2 cDNAs were cloned against a cDNA library prepared from the HEK293T cells. A series of constructs were created by subcloning the corresponding genes into a modified pCAG vector in-frame with a TEV/HRV-3C cleavable N-terminal Protein A tag using in-Fusion cloning. These vectors were constructed to express recombinant HDAC6 proteins, including hHDAC6-CD1-2, hHDAC6-H216A, hHDAC6-H611A, hHDAC6-Y782F, and hHDAC6-H216/611A. Among these, H216A was a CD1-inactive mutant, H611A and Y782F were the CD2-inactive mutants, and H216/611A was a dual-inactive mutant for both active sites of CD1 and CD2. Efforts were also made to create mutants at the zinc-binding sites in either active site of human HDAC6, i.e. D253A, D346A and H255A for the zinc-binding site of CD1, and D649A, D742A and H651A for the zinc-binding site of CD2. However, none of these mutants at the zinc-binding sites were successfully expressed. These recombinant human HDAC6 proteins were expressed in the 293F cells. Seventy-two hours after transfection, the cells were harvested by centrifugation and washed once with HBS (50 mM HEPES, pH 7.5; 150 mM NaCl). The cell debris was resuspended with lysis buffer (50 mM HEPES, pH 7.5; 300 mM NaCl; 0.5% CHAPS with 5 mM ATP; 10 mM $MgCl_2$; 1 mM TCEP; 10% glycerol), and centrifuged at 24,000g for 30 min at 4°C. The supernatants were incubated with pre-equilibrated IgG resins, washed with high salt wash buffer (50 mM HEPES, pH 7.5; 500 mM NaCl;

0.5% CHAPS with 5 mM ATP; 10 mM $MgCl_2$; 1 mM TCEP; 10% glycerol). The N-terminal tag was removed by on-column overnight TEV digestion. The eluted proteins were then loaded onto a Superdex 200 increase 10/300 GL gel filtration column equilibrated in 50 mM HEPES, pH 7.5; 150 mM NaCl; 1 mM TCEP using AKTA pure (Cytiva, Sweden). The peak fractions were collected and subsequently concentrated using ultrafiltration tubes (Cytiva, Sweden). hSirt2 protein was also expressed and purified to serve as one of the controls for subsequent functional analysis.

Cryo-EM sample preparation and data collection

Recombinant hHDAC6-CD1-2 protein was concentrated to 0.6 mg/ml. The cryo-EM grids were prepared using Vitrobot Mark IV (Thermo Fisher Scientific, German) set to 4°C and 100% humidity. Two point five microliters hHDAC6-CD1-2 protein solution was loaded onto a glow-discharged R1.2/1.3 Au/Cu holey carbon grid (Quantifoil Inc, German), which was blotted for 2 s and plunged frozen into liquid ethane pre-cooled with liquid nitrogen.

A total of 3 datasets including 14,937 movies were collected using a Titan Krios electron microscope (Thermo Fisher Scientific, Eindhoven, Netherlands) with a Falcon IV direct electron detector (Thermo Fisher Scientific, Eindhoven, Netherlands) at 300 kV with a magnification of 130,000, corresponding to a pixel size of 0.466 Å. Image acquisition was performed using EPU Software (Thermo Fisher Scientific, Eindhoven, Netherlands). Each micrograph was dose fractionated to 1080 EER frames with a total exposure time of 3.5 s, resulting in a total dose of ~50 $e^-/Å^2$.

Cryo-EM data processing

The beam-induced motion was corrected by relion[67]. Contrast transfer function (CTF) parameters were estimated by patch CTF estimation in CryoSPARC[68]. Micrographs with an estimated resolution exceeding 3.5 Å were discarded, leaving 10493 micrographs for downstream processing. Two rounds of blob picking were used to pick particles with a diameter of 60 to 120 Å. Templates were generated by 2D classification, followed by a final round of template-based auto picking resulting in a selection of 12,675,859 particles. After a few rounds of 2D classification, 37,401 particles were selected for ab-initio reconstruction for a start-up model. Iterative rounds of 2D classification and heterogeneous refinement were subsequently performed to clean the particle datasets. A total of 831,669 particles were subjected to 3D classification in CryoSPARC, among which 319,827 particles yielding clear density were exported to relion for Bayesian polishing. The polished particles were then imported back into CryoSPARC for a final round of 3D classification, leaving 109,995 particles yielding the best signal finally reconstituted to a 3.85-Å structure.

Model building and refinement

The initial model of human HDAC6 was predicted using AlphaFold 2[22]. Then the model was rigidly fitted into the density map using UCSF ChimeraX[69]. The orientation of the model was confirmed with the assistance of molecular dynamic analysis of the structure. Iterative rounds of automated real-space refinement and manual adjustment

were performed in Phenix[70] and COOT[71]. The final model statistics were validated by comprehensive validation in PHINEX. All structure figures were created using ChimeraX.

Deacetylase activity assay

The substrates were synthesized by Genescript (Nanjing, China) and dissolved in a 10 mM stock solution with DMSO. For HDAC6 activity assay, fluorogenic substrate (Ac-Ser-Asp-Lys(Ac)-AMC) and the enzyme were diluted into assay buffer (50 mM Tris-HCl, pH 8.0; 137 mM NaCl, 2.7 mM KCl; 1.0 mM $MgCl_2$) at a serial of concentrations. The reaction was initiated by mixing the substrate and the enzyme at 37℃ for a proposed time period. The reaction was then stopped by adding an equal volume of developer buffer (1 μM Trypsin, 10 μM TSA in assay buffer) and being incubated at 37℃ for 20 min. The reaction mix was transferred into a Costar 96-well half-area white bottom plate, and the fluorescence signals were measured using a SpectraMax i3x plate reader (Molecular Device, USA) (λ_{ex} = 360 nm, λ_{em} = 455 nm). The deacetylated substrates were quantified by a standard curve using Fluor de Lys deacetylated standard (Enzo Life Sciences, USA). K_M and k_{cat} values of the reactions were calculated according to Michaelis-Menten's equation. Sirt2 activity was measured with fluorogenic substrate (Ac-Gln-Pro-Lys-Lys(Ac)-AMC) in similar procedures, except NAD was supplemented into the assay buffer and Nicotinamide was used in the developer buffer instead of TSA.

The full-length α-tubulin substrate was extracted from HDAC6-KO EA.hy 926

cells with non-reducing native lysis buffer (50 mM Tris-HCl, pH 8.0; 137 mM NaCl; 2.7 mM KCl; 1.0 mM $MgCl_2$; 1% TritonX-100). The lysate was cleared by centrifugation and quantified by BCA analysis. Thirty microgram substrate was then mixed with 2 μg of purified recombinant HDAC6 protein, and incubated at 37 ℃ for 15 min. The reaction was stopped by adding 5× SDS-loading buffer followed by heating to 95 ℃ for 5 min. The acetylated α-tubulin was also quantified using Western blot analysis.

Thiolacetic acid measurement assay

Briefly, in a cell-free system, 100 μl of the enzyme (20 nM) in assay buffer with or without 20 μM NaHS was added to 100 μl substrate solution (1 μM). After incubation for 30 min at 37℃, the reaction mix was derivatized with 0.86 mg/ml 3-Bromopropylamine hydrobromide (pH 10) at 70℃ for 40 min. Then the derivatization reaction was stopped by adding formic acid to adjust the pH value to 7. The derivatized solution was analyzed using UHPLC-qqq-MS (Agilent Technologies Inc., USA). Thiolacetic acid in the samples was determined by comparing sample retention volume and m/z values to that of standard thiolacetic acid (Sigma, USA).

For cultured cells, 2×10^7 cells were collected and washed 3 times with PBS. Then cells were lysed 2 times with 50 μl 50% methanol by freeze thaw cycles and the cell lysate was cleared by centrifugation. Fifty μl supernatant were derivatized from the above procedures and subjected to UHPLC-qqq-MS analysis.

For mouse tissues, the organs were freshly harvested from the wild-type C57 BL/6

mice after sacrifice, 80 mg of tissue and 200 µl of saline were mixed, lysed and cleared by centrifugation. Fifty µl lysate were mixed with 150 µl methanol for protein precipitation. Following centrifugation, 50 µl supernatant were derivatized from the above procedure and subjected into UHPLC-qqq-MS (Agilent Technologies Inc., USA) analysis. For mouse serum samples, blood was freshly collected from wild-type C57 BL/6 mice under anesthesia with sodium pentobarbital (50 mg/kg i.p.), serums were separated by centrifugation in 3000 rpm at 4℃ for 20 mins. Fifty µl lysate were mixed with 150 µl methanol for protein precipitation. Following centrifugation, 50 µl supernatant were derivatized from the above procedure and subjected into UHPLC-qqq-MS (Agilent Technologies Inc., USA) analysis. All animal experimental procedures were performed according to the Guide for the Care and Use of Laboratory Animals of the National Institutes of Health (NIH) of the United States and approved by the Ethics Committee of Experimental Research, Fudan University Shanghai Medical College. IACUC Animal Project Numbers (APN): 20210226-003, 20180302-045 and 20240229-014.

For human serum samples, serums were freshly collected from heathy candidates, 50 µl serum were mixed with 150 µl methanol for protein precipitation. Following centrifugation, 50 µl supernatant were derivatized from the above procedure and subjected into UHPLC-qqq-MS (Agilent Technologies Inc., USA) analysis. Ethical approval for this study was obtained from the Ethical Committee of Fudan University School of Basical Medical Science (Approval No.2021-C002). The requirement for informed consent was waived due to the use of anonymized human samples, as per the

guidelines of the ethics committee.

Surface plasmon resonance assay

The binding between HDAC6 and H_2S was determined using surface plasmon resonance assay (SPR) assay on a biacore T200 instrument (GE Healthcare, Sweden) according to the manufacturer's instructions. Briefly, the hHDAC6-CD1-2 protein was immobilized onto a CM5 sensor chip, using standard amine coupling chemistry following the supplier's protocol. A concentration series of NaHS (0.023-600 μM) was injected over experimental and control flow cells at a flow rate of 30 μl/min at 25 °C. Duplicate injections of each NaHS concentration were performed with a blank buffer injected periodically for double referencing. The protein surface was regenerated between binding cycles by injection of EP+ buffer (Cytiva, USA). A zinc-dependent HDAC inhibitor Trichostatin A (TSA) (0.0008-2 μM) was used as a control ligand. All sensor-grams were processed by double referencing and kinetic rate constants were evaluated using BIAevaluation software (GE Healthcare, USA). The zinc-stripped hHDAC6-CD1-2 protein was obtained by adding 10 mM Sodium diethyldithiocarbamatre (DDTC) and 1% SDS into the protein solution, incubated at 37, then heated to 95℃ for 5 min. Then, the zinc-stripped protein was loaded onto a Hitrep Desalting column (GE Healthcare, Sweden) for buffer exchanging to HBS (50 mM HEPES, pH 7.5, 150 mM NaCl).

Quantum chemical calculations for the mechanisms underlying bond formation between H_2S and the metal-active-sites of the metalloenzymes

Size-reduced active site models of a series of metalloenzymes were established based on their crystallographic structures, including HDAC6 (PDB ID: 5EDU[20]), HDAC10 (7KUQ[72]), angiotensin-converting enzyme (ACE) (1O8A[73]), histone lysine demethylase (PHF8) (3KV4[74]), phospholipase A2 (3U8B[75]), arginase-1 (2AEB[76]), sirtuin-2 (1J8F[77]), oxygenated hemocyanin II (1OXY[78]), and deoxygenated hemocyanin II (1LLA[79]). The spin multiplicities (2S+1) of the model system of PHF8 (containing one Fe^{2+})[80], arginase (containing two Mn^{2+})[81], and oxygenated hemocyanin II (containing two Cu^{2+})[82] were set to 5, 11, and 1 (open-shell), respectively. The spin multiplicities of the rest systems were set to 1 (close-shell). HS^- anions were modeled around the metals in the initial structures. The C-α atoms in the residues were frozen and the structures were optimized using the TPSSh[20]-D3(BJ) functional. The basis sets used for structure optimization were in line with the high-level calculations in XO. Energy gap between highest occupied molecular orbital (HOMO) and lowest unoccupied molecular orbital (LUMO) were calculated at ε = 4/B3PW91[83]-D3(BJ)/6-311+G(2d,2p)|SDD level. Chemical bond analysis including bond order, localized molecular orbital (LMO)[84], bond order density (BOD)[84], natural adaptive orbital (NAdO)[86], electron density difference (EDD), charge decomposition analysis (CDA)[87,88], and extended transition state - natural orbitals for chemical valence (ETS-NOCV)[89] were calculated with corresponding methods at various levels using Multiwfn[90,91] software. Mayer bond order[92] (in Hilbert space) and LMO (Pipek-Mezey

algorism with Mulliken population) were calculated at ε = 4/PBE0[93]-D3(BJ)/def2-SVP|SDD level. Fuzzy bond order[94] (in Becke space), LMO (Pipek-Mezey algorism with Becke population), BOD (in Becke space), NAdO (in Becke space), EDD, and ETS-NOCV were calculated at ε = 4/PBE0-D3(BJ)/6-311+G(2d,2p)|SDD level. CDA (Mulliken method) was calculated at ε = 4/PBE0-D3(BJ)/def2-TZVP|SDD level. Binding energy was calculated at MN15/6-311+G(2d,2p)|SDD level where basis-set superposition errors (BSSE) were considered in the binding energy calculations with counterpoise correction[95].

Quantum chemical calculations for the reactions catalyzed by HDAC6 with H_2S or H_2O

To examine the microscope mechanism of the deacetylation reaction catalyzed by human HDAC6 CD2 (hHDAC6-CD2), a 460-atom (461-atom for mechanism B2 and 439-atom for mechanism C) cluster model system was established directly based on the crystallographic hHDAC6-CD2 structure (PDB ID: 5EDU)[20], which was the only available crystallographic structure for hHDAC6-CD2. The residues in our model were listed as following: P501, E502, R506, S568, P608, G609, H610, H611, C618, G619, F620, C621, D647, W648, D649, V650, H651, H652, G653, N654, F680, P681, D742, A743, L749, G750, E779, G780, G781, and Y782. The substrate acetylated lysine was modeled into the model of hHDAC6-CD2 active-site according to the structure alignment of hHDAC6-CD2 structure (PDB ID: 5EDU) and zHDAC6-CD2 Y745F structure (PDB ID: 5EFK)[20], which was the only available structure featuring a

substrate bound at the active-site. Hydrogen atoms were employed to saturate the dangling bonds on the boundary of the model system. The system contained a K^+ ion near the active site, which was reported to be important for the energy barrier of the deacetylation reaction in HDAC8[24,96]. Twenty-six atoms at the boundary of the model system were frozen to stabilize the active-site structure (Figure S33c).

A two-level eXtended ONIOM (XO)[97,98] fragmentation method was carried out for the calculations. Our choice to utilize the XO method was driven by its innovative nature as an extension of the traditional ONIOM method. The XO method exhibits notable advancements in both accuracy and efficiency compared to the conventional QM/QM or QM/MM approaches[99-101]. These attributes make it particularly suitable for precise and efficient computations in large-scale systems. Our XO2 partitioning schemes contained 12 primitive models (Figure S33a). The model involved the whole cluster was treated at the low-level. The rest 11 elementary sub-models at the high-level contained a size-reduced active-site model and 10 patches (Figure S33b). Combination of 11 models at the high-level covered all atoms, resulting in a final high-level calculation for the whole system according to the inclusion-exclusion principle (IEP):

$$\left|A_1 \cup A_2 \cup \cdots \cup A_n\right| = \sum_{i=1}^{n}\left|A_i\right| - \sum_{i<j}\left|A_i \cap A_j\right| + \sum_{i<j<k}\left|A_i \cap A_j \cap A_k\right| + \cdots + (-1)^{n-1}\left|A_1 \cap A_2 \cap \cdots \cap A_n\right| = \sum_{i=1}^{n}\left|A_i\right| - \sum_{m=2}^{n}(-1)^m\left|A_m^D\right| \quad (17)$$

The A_m^D represented all derived terms for a given m, which contains $\frac{n!}{(n-m)!}$ possible intersections of m primitive terms out of the total of n primitive terms.

The energy of a two-layered ONIOM2 (QM:MM or QM:QM) was calculated as

the following formula:

$$E\left(ONIOM2\left(H:L\right)\right)=E\left(Model@H\right)+E\left(Real@L\right)-E\left(Model@L\right)$$
$$=E\left(Model@H\right)+E\left(Real@L\right)-E\left(\left(Model\cap Real\right)@L\right)$$

The energy of a n-layered ONIOMn was calculated as the following formula:

$$E\left(ONIOMn\left(Level_1:\cdots:Level_n\right)\right)=\sum_{i=1}^{n}E\left(Model_i@Level_i\right)-\sum_{i=1}^{n-1}E\left(Model_i@Level_{i+1}\right)$$

Where

$Model_1\subset Model_2\subset\cdots\subset Model_n$ and $Level_1>Level_2>\cdots>Level_n$

XOn was a straightforward generalization of ONIOMn by IEP to allow for overlapping fragments:

$$E\left(XOn\left(Level_1:\cdots:Level_n\right)\right)=\sum_{i=1}^{p}E\left(Model_i@Level_i\right)-\sum_{m=2}^{p}\left(-1\right)^m E\left(Model_m^D@Level_m^D\right)$$

Where *p* represented the primitive models (e.g. 12 primitive models in our XO2 schemes (Figure S33a and b) and $Model_m^D$ represented the derivative models according to IEP.

Different models of XO were combined to effectively correct the boundary errors[102]. Force-error test[97] was used to control the marginal error of the models in the XO schemes. To further validate our methodological choice, we conducted rigorous tests on our system. Our findings revealed that the force-error associated with the XO2 method was considerably lower than that observed in the standard QM/QM approach, across various sizes of high-level (DFT) calculations (specifically, ONIOM2_126 and ONIOM2_225). This result underscores the reliability of the XO method in ensuring consistency with the full cluster calculations (Real@H) during geometry optimization (Figure S33d).

Another critical aspect of our study is the computational efficiency of the XO2 scheme. In our parallel computing setup, the overall computational cost of the XO2 scheme was comparable to that of the ONIOM2_126 scheme. Importantly, this cost-effectiveness was achieved without compromising accuracy, making it a more viable option than the more expensive ONIOM2_225 scheme.

Optimization and frequency calculations were performed using B3LYP[103] hybrid functional including Grimme's dispersion correction (BJ-damping)[104] for the high-level calculations, along with the 6-31G(d,p)[105] basis set for C, H, O, N atoms; 6-311+G(d,p)[106,107] for S atoms and Stuttgart ECP (SDD)[108] for the Zn and K atoms. Whereas, semi-empirical PM6[109] including Grimme's dispersion correction (zero-damping)[110] was used for the low-level calculations, which was accurate among semiempirical methods[111]. The polarizable continuum model (PCM)[112] was carried out for the high-level calculations with a dielectric constant $\varepsilon = 4$ for optimization and frequency calculations, which was appropriate for the enzyme active-site[113]. For single-point-energy calculations, the MN15[114] functional, which was recommended for an organic system with transition metal[115], with a larger basis set of def2-TZVP[116] was employed and solvation model based on electron density (SMD)[117] was used for the high-level calculations. Quantum chemical (QC) calculations were performed using the Gaussian 16 B.01 software package[118].

Molecular dynamics simulations

A model system of the human HDAC6 CD2 domain (hHDAC6-CD2) was

established based on the crystallographic hHDAC6-CD2 structure (PDB ID: 5EDU)[20]. Hydrogens were added to the protein using the H++ program[119]. H610 and H611 were single-protonated with a hydrogen on the delta nitrogen according to our QC calculations results from mechanism A1 (HID610/HID611) and the reported studies[23,24]. The α-tubulin (acetylated K40) structure was modeled based on the structure of human α1B/β3 microtubules (PDB ID: 6E7B)[120]. The substrate Ac-Ser-Asp-Lys (Ac)-AMC was modeled based on the crystallographic zHDAC6-CD2 Y745F structure (PDB ID: 5EFK)[20] and optimized at the B3LYP-D3(BJ)/def-TZVP[121] level. The initial ES complex structure of hHDAC6-CD2 and substrate Ac-Ser-Asp-Lys (Ac)-AMC were obtained according to structure alignment of hHDAC6-CD2 structure (PDB ID: 5EDU)[20] and zHDAC6-CD2 Y745F structure (PDB ID: 5EFK)[20]. Each complex was simulated with three replicas to test stability and reproducibility.

The molecular dynamics (MD) simulations were performed using the GROMACS package version 2019.3[122] with the AMBER14SB force field[123] for the protein hHDAC6-CD2 or α-tubulin and the generalized Amber force field (GAFF)[124] for the substrate Ac-Ser-Asp-Lys (Ac)-AMC and a non-standard residue, acetylated K40. The restrained electrostatic potential charges (RESP2)[125] of the substrate Ac-Ser-Asp-Lys (Ac)-AMC and acetylated K40 were calculated using Multiwfn[90,91] software at B3LYP-D3(BJ)/def2-TZVP level and the topology files were generated using Sobtop[126] software. The LJ12-6 parameters proposed by Zhang and coworkers were used for the zinc[127] and potassium[128] ion. In the simulations, a periodic boundary was utilized. The complex was placed within a rectangular box and the distance between the complex

surface and the wall of the box was greater than 15 Å. The translation and rotation of the mass center of the complex were eliminated to avoid too-close distance of the complex and periodic images in such a triclinic box. Water molecules were filled into the space of the box with the TIP3P[129] water model and 0.15M NaCl was added to neutralize the system (Figure S26a). The system underwent energy minimization using the conjugate gradient method followed by 300 ps of position restrained MD simulations. The complex was restrained and the solvent was freely equilibrated. Finally, the whole system was simulated for 1000 ns at 310K and slowly annealed from 310K to 0K during 100 ns to obtain a stable structure for graph generation and structure comparison (Figure S25 – S27), leaving the bonds connected to the hydrogen restraint using a time step of 2 fs with atomic coordinates saved every 2 ps for subsequent analysis. The v-rescale thermostat[130] with a time constant of 0.2 ps was applied to maintain a constant temperature of 310 K in the system while the solute and solvent were coupled separately. The Parrinello-Rahman barostat[131] with a time constant of 2 ps was applied to maintain a constant pressure of 1 atm for the long time MD simulations and the Berendsen barostat[132] for the 300 ps position restrained MD simulations. LJ and electrostatic interactions between charged groups within 1 nm were calculated explicitly, while the long-range interactions were treated using the particle mesh Ewald method[132]. Data analysis and graph generation were performed using the VMD software[134].

MD simulations were also performed to examine spontaneous diffusion of HS^- into CD2 active site of HDAC6. Twenty HS^- anions were added randomly in solution

around the hHDAC6-CD2 to simulate spontaneous binding between HS^- and the enzyme. An HS^- was found to enter the active-site tunnel of hHDAC6-CD2 spontaneously and bind at the zinc ion steadily. In addition, three replicas of MD simulations were performed with or without catalytic zinc ions in HDAC6-CD2 to clarify the role of the zinc ion in HS^- binding. CHARMM36m force field was applied in MD simulations involving HS^-[135,136].

Statistical analysis

Data are expressed as mean ± SEM. The data were analyzed by SPSS Inc. v24 software. Normal distribution of data was determined for each comparison firstly. Differences between two groups were compared with student's t-test and multiple group comparisons were tested by ANOVA with a Tukey's post hoc test for normally distributed data. Otherwise, Mann-Whitney U test or Kruskal-Wallis test followed by the Dunn's post hoc test was used. Probability values < 0.05 (two-sides) were considered statistically significant.

References

1. Walsh, G. & Jefferis, R. Post-translational modifications in the context of therapeutic proteins. *Nat. Biotechnol.* **24**, 1241-1252 (2006).

2. Wu, D. *et al.* Hydrogen sulfide functions as a micro-modulator bound at the copper active site of Cu/Zn-SOD to regulate the catalytic activity of the enzyme. *Cell Reports* **42**, 112750 (2023).

3. Waldron, K. J. & Robinson, N. J. How do bacterial cells ensure that metalloproteins get the correct metal? *Nat. Rev. Microbiol.* **7**, 25-35 (2009).

4. Holm, R. H., Kennepohl, P. & Solomon, E. I. Structural and functional aspects of metal sites in biology. *Chem. Rev.* **96**, 2239-2314 (1996).

5. Yu, J. *et al.* MeDBA: the metalloenzyme data bank and analysis platform. *Nucleic Acids Res.* **51**, D593-D602 (2023).

6. Schomburg, D. *Springer Handbook of Enzymes*. Springer Berlin Heidelberg, New York, (2013).

7. Fischer, E. Einfluss der configuration auf die wirkung der enzyme. *Ber. Dt. Chem. Ges.* **27**, 2985-2993 (1894).

8. Koshland, D. E. Application of a theory of enzyme specificity to protein synthesis. *Proc. Natl. Acad. Sci. U. S. A.* **44**, 98-104 (1958).

9. de Ruijter, A. J., van Gennip, A. H., Caron, H. N., Kemp, S. & van Kuilenburg, A. B. Histone Deacetylases (HDACs): Characterization of the Classical HDAC Family. *Biochem. J.* **370**, 737-749 (2003).

10. Kaluza, D. *et al.* Class IIb HDAC6 regulates endothelial cell migration and

angiogenesis by deacetylation of cortactin. *Embo J.* (2011).

11. Parmigiani, R. B. *et al.* HDAC6 is a specific deacetylase of peroxiredoxins and is involved in redox regulation. *Proc. Natl. Acad. Sci. U. S. A.* **105**, 9633-9638 (2008).

12. Valenzuela-Fernández, A., Cabrero, J. R., Serrador, J. M. & Sánchez-Madrid, F. HDAC6: a key regulator of cytoskeleton, cell migration and cell–cell interactions. *Trends Cell Biol.* **18**, 291-297 (2008).

13. Lam, H. C. *et al.* Histone deacetylase 6-mediated selective autophagy regulates COPD-associated cilia dysfunction. *J. Clin. Invest.* **123**, 5212-5230 (2013).

14. Polhemus, D. J. & Lefer, D. J. Emergence of hydrogen sulfide as an endogenous gaseous signaling molecule in cardiovascular disease. *Circ. Res.* **114**, 730-737 (2014).

15. Paul, B. D. *et al.* Cystathionine β-lyase deficiency mediates neurodegeneration in Huntington's disease. *Nature* **509**, 96-100 (2014).

16. Yuan, S., Shen, X. & Kevil, C. G. Beyond a gasotransmitter: hydrogen sulfide and polysulfide in cardiovascular health and immune response. *Antioxid. Redox Signal.* **27**, 634-653 (2017).

17. Cui, C. *et al.* CD4(+) T-cell endogenous cystathionine γ lyase-hydrogen sulfide attenuates hypertension by sulfhydrating liver kinase B1 to promote T regulatory cell differentiation and proliferation. *Circulation* **142**, 1752-1769 (2020).

18. Liu, F. *et al.* Hydrogen sulfide improves wound healing via restoration of endothelial progenitor cell functions and activation of angiopoietin-1 in type 2 diabetes. *Diabetes* **63**, 1763-1778 (2014).

19. Li, Z. *et al.* Mitochondrial H_2S regulates BCAA catabolism in heart failure. *Circ.*

Res. **131**, 222-235 (2022).

20. Hai, Y. & Christianson, D. W. Histone deacetylase 6 structure and molecular basis of catalysis and inhibition. *Nat. Chem. Biol.* **12**, 741-747 (2016).

21. Miyake, Y. *et al.* Structural Insights into HDAC6 Tubulin Deacetylation and its Selective Inhibition. *Nat. Chem. Biol.* **12**, 748-754 (2016).

22. Tunyasuvunakool, K. *et al.* Highly accurate protein structure prediction for the human proteome. *Nature* **596**, 19 (2021).

23. Corminboeuf, C., Hu, P., Tuckerman, M. E. & Zhang, Y. K. Unexpected deacetylation mechanism suggested by a density functional theory QM/MM study of histone-deacetylase-like protein. *J. Am. Chem. Soc.* **128**, 4530-4531 (2006).

24. Wu, R., Wang, S., Zhou, N., Cao, Z. & Zhang, Y. A proton-shuttle reaction mechanism for histone deacetylase 8 and the catalytic role of metal ions. *J. Am. Chem. Soc.* **132**, 9471-9479 (2010).

25. Prejanò, M., Vidossich, P., Russo, N., De Vivo, M. & Marino, T. Insights into the catalytic mechanism of domains CD1 and CD2 in histone deacetylase 6 from quantum calculations. *ACS Catal.* **11**, 3084-3093 (2021).

26. Sunner, S. & Wadso, I. The heat of hydrolysis of thiolacetic acid. *Trans. Faraday Soc.* **53**, 455-459 (1957).

27. Nechay, M. R. *et al.* Histone deacetylase 8: characterization of physiological divalent metal catalysis. *J. Phys. Chem. B* **120**, 5884-5895 (2016).

28. Bras, N. F., Fernandes, P. A. & Ramos, M. J. QM/MM study and MD simulations on the hypertension regulator angiotensin-converting enzyme. *ACS Catal.*

4, 2587-2597 (2014).

29. Katz, J., Lieberman, I. & Barker, H. A. Acetylation of amino acids by enzymes of clostridium-kluyveri. *J. Biol. Chem.* **200**, 417-429 (1953).

30. Choudhary, C., Weinert, B. T., Nishida, Y., Verdin, E. & Mann, M. The growing landscape of lysine acetylation links metabolism and cell signalling. *Nat. Rev. Mol. Cell Biol.* **15**, 536-550 (2014).

31. Wu, Q., Schapira, M., Arrowsmith, C. H. & Barsyte-Lovejoy, D. Protein arginine methylation: from enigmatic functions to therapeutic targeting. *Nat. Rev. Drug Discov.* **20**, 509-530 (2021).

32. Magee, P. N. & Hultin, T. Toxic liver injury and carcinogenesis. Methylation of proteins of rat-liver slices by dimethylnitrosamine in vitro. *Biochem. J.* **83**, 106-114 (1962).

33. Zhang, D. *et al.* Metabolic regulation of gene expression by histone lactylation. *Nature* **574**, 575 (2019).

34. Rimington, C. Phosphorylation of proteins. *Biochem. J.* **21**, 272-281 (1927).

35. Ardito, F., Giuliani, M., Perrone, D., Troiano, G. & Lo, M. L. The crucial role of protein phosphorylation in cell signaling and its use as targeted therapy. *Int. J. Mol. Med.* **40**, 271-280 (2017).

36. Mann, M. & Jensen, O. N. Proteomic analysis of post-translational modifications. *Nat. Biotechnol.* **21**, 255-261 (2003).

37. Gleeson, D. & Gleeson, M. P. Application of QM/MM and QM methods to investigate histone deacetylase 8. *Med. Chem. Commun.* **6**, 477-485 (2015).

38. Murdoch, J. R. What is the rate-limiting step of a multistep reaction. *J. Chem. Educ.* **58**, 32-36 (1981).

39. Filipovic, M. R., Zivanovic, J., Alvarez, B. & Banerjee, R. Chemical biology of H_2S signaling through persulfidation. *Chem. Rev.* **118**, 377-461 (2018).

40. Zhang, Y., Gilquin, B., Khochbin, S. & Matthias, P. Two catalytic domains are required for protein deacetylation. *J. Biol. Chem.* **281**, 2401-2404 (2006).

41. Zou, H., Wu, Y., Navre, M. & Sang, B. Characterization of the two catalytic domains in histone deacetylase 6. *Biochem. Biophys. Res. Commun.* **341**, 45-50 (2006).

42. Leucker, T. M. *et al.* Cystathionine β-lyase protects vascular endothelium: a role for inhibition of histone deacetylase 6. *Am. J. Physiol.-Heart Circul. Physiol.* **312**, H711-H720 (2017).

43. Chi, Z. *et al.* Histone deacetylase 6 inhibitor tubastatin A attenuates angiotensin II-induced hypertension by preventing cystathionine β-lyase protein degradation. *Pharmacol. Res.* **146** (2019).

44. Jung, J. K. *et al.* Inhibition of HDACs (histone deacetylases) ameliorates high-fat diet-induced hypertension through restoration of the MsrA (Methionine sulfoxide reductase A)/hydrogen sulfide axis. *Hypertension* **78**, 1103-1115 (2021).

45. Li, M. *et al.* Sp1 S-sulfhydration induced by hydrogen sulfide inhibits inflammation via HDAC6/MyD88/NF-κB signaling pathway in adjuvant-induced arthritis. *Antioxidants* **11** (2022).

46. Yang, X. *et al.* SSBP1 positively regulates RRM2, affecting epithelial

mesenchymal transition and cell cycle arrest in human lung adenocarcinoma cells. *Cell. Signal.* **127** (2025).

47. Su, J. *et al.* Identification of SSBP1 as a ferroptosis-related biomarker of glioblastoma based on a novel mitochondria-related gene risk model and in vitro experiments. *J. Transl. Med.* **20** (2022).

48. Weis, K. Regulating access to the genome: Nucleocytoplasmic transport throughout the cell cycle. *Cell* **112**, 441-451 (2003).

49. Strozynski, J. *et al.* Proteomic identification of the heterogeneous nuclear ribonucleoprotein K as irradiation responsive protein related to migration. *J. Proteomics* **113**, 154-161 (2015).

50. Chan, X. *et al.* Upregulation of ENAH by a PI3K/AKT/β-catenin cascade promotes oral cancer cell migration and growth via an ITGB5/Src axis. *Cell. Mol. Biol. Lett.* **29** (2024).

51. He, Z., Li, W., Zheng, T., Liu, D. & Zhao, S. Human umbilical cord mesenchymal stem cells-derived exosomes deliver microRNA-375 to downregulate ENAH and thus retard esophageal squamous cell carcinoma progression. *J. Exp. Clin. Cancer Res.* **39** (2020).

52. Hudlicka, O., Brown, M. D., Egginton, S. & Dawson, J. M. Effect of long-term electrical stimulation on vascular supply and fatigue in chronically ischemic muscles. *J. Appl. Physiol.* **77**, 1317-1324 (1994).

53. Battaglia, R. A., Delic, S., Herrmann, H. & Snider, N. T. Vimentin on the move:new developments in cell migration. *F1000Research* **7** (2018).

54. Coelho-Rato, L. S., Parvanian, S., Modi, M. K. & Eriksson, J. E. Vimentin at the core of wound healing. *Trends Cell Biol.* **34**, 239-254 (2024).

55. Tsai, H. & Lin, C. Hypo-phosphorylated hnRNPK promotes migration of triple negative breast cancer cells through an Aurora-A-independent manner. *Faseb J.* **32S** (2018).

56. Wallace, J. L. Hydrogen sulfide-releasing anti-inflammatory drugs. *Trends Pharmacol. Sci.* **28**, 501-505 (2007).

57. Geng, B. *et al.* Endogenous hydrogen sulfide regulation of myocardial injury induced by isoproterenol. *Biochem. Biophys. Res. Commun.* **318**, 756-763 (2004).

58. Foss, F. *et al.* A Phase II trial of Belinostat (PXD101) in patients with relapsed or refractory peripheral or cutaneous T-cell lymphoma. *Br. J. Haematol.* **168**, 811-819 (2015).

59. San-Miguel, J. F. *et al.* Phase Ib study of panobinostat and bortezomib in relapsed or relapsed and refractory multiple myeloma. *J. Clin. Oncol.* **31**, 3696-3703 (2013).

60. Batchu, S. N., Brijmohan, A. S. & Advani, A. The therapeutic hope for HDAC6 inhibitors in malignancy and chronic disease. *Clin. Sci.* **130**, 987-1003 (2016).

61. Henderson, R. The potential and limitations of neutrons, electrons and x-rays for atomic-resolution microscopy of unstained biological molecules. *Q. Rev. Biophys.* **28**, 171-193 (1995).

62. Glaeser, R. M. How good can single-particle cryo-EM become? What remains before it approaches its physical limits? *Annu. Rev. Biophys.* **48**, 45-61 (2019).

63. Elmlund, D., Le, S. N. & Elmlund, H. High-resolution cryo-EM: the nuts and bolts. *Curr. Opin. Struct. Biol.* **46**, 1-6 (2017).

64. Dull, T. *et al.* A third-generation lentivirus vector with a conditional packaging system. *J. Virol.* **72**, 8463-8471 (1998).

65. Sanjana, N. E., Shalem, O. & Zhang, F. Improved vectors and genome-wide libraries for CRISPR screening. *Nat. Methods* **11**, 783-784 (2014).

66. Sweeney, N. V. *et al.* Cyclic strain-mediated regulation of vascular endothelial cell migration and tube formation. *Biochem. Biophys. Res. Commun.* **329**, 573-582 (2005).

67. Kimanius, D., Dong, L., Sharov, G., Nakane, T. & Scheres, S. H. W. New tools for automated cryo-EM single-particle analysis in RELION-4.0. *Biochem. J.* **478**, 4169-4185 (2021).

68. Punjani, A., Rubinstein, J. L., Fleet, D. J. & Brubaker, M. A. cryoSPARC: algorithms for rapid unsupervised cryo-EM structure determination. *Nat. Methods* **14**, 290-296 (2017).

69. Pettersen, E. F. *et al.* UCSF ChimeraX: structure visualization for researchers, educators, and developers. *Protein Sci.* **30**, 70-82 (2021).

70. Liebschner, D. *et al.* Macromolecular structure determination using x-rays, neutrons and electrons: recent developments in phenix. *Acta Crystallogr. Sect. D-Struct. Biol.* **75**, 861-877 (2019).

71. Emsley, P., Lohkamp, B., Scott, W. G. & Cowtan, K. Features and development of Coot. *Acta Crystallogr. Sect. D-Biol. Crystallogr.* **66**, 486-501 (2010).

72. Hai, Y., Shinsky, S. A., Porter, N. J. & Christianson, D. W. Histone deacetylase 10 structure and molecular function as a polyamine deacetylase. *Nat. Commun.* **8**, 15368 (2017).

73. Natesh, R., Schwager, S., Sturrock, E. D. & Acharya, K. R. Crystal structure of the human angiotensin-converting enzyme-lisinopril complex. *Nature* **421**, 551-554 (2003).

74. Horton, J. R. *et al.* Enzymatic and structural insights for substrate specificity of a family of jumonji histone lysine demethylases. *Nat. Struct. Mol. Biol.* **17**, 38-52 (2010).

75. Lee, L. K. *et al.* Selective inhibition of human group IIA-secreted phospholipase A_2 (hGIIA) signaling reveals arachidonic acid metabolism is associated with colocalization of hGIIA to vimentin in rheumatoid synoviocytes. *J. Biol. Chem.* **288**, 15269-15279 (2013).

76. Di Costanzo, L. *et al.* Crystal structure of human arginase I at 1.29-Å resolution and exploration of inhibition in the immune response. *Proc. Natl. Acad. Sci. U. S. A.* **102**, 13058-13063 (2005).

77. Finnin, M. S., Donigian, J. R. & Pavletich, N. P. Structure of the histone deacetylase SIRT2. *Nat. Struct. Biol.* **8**, 621-625 (2001).

78. Magnus, K. A. *et al.* Crystallographic analysis of oxygenated and deoxygenated states of arthropod hemocyanin shows unusual differences. *Proteins* **19**, 302-309 (1994).

79. HAZES, B. *et al.* Crystal-structure of deoxygenated limulus-polyphemus

subunit-II hemocyanin at 2.18-angstrom resolution - clues for a mechanism for allosteric regulation. *Protein Sci.* **2**, 597-619 (1993).

80. Chaturvedi, S. S. *et al.* Catalysis by the non-heme iron(II) histone demethylase PHF8 involves iron center rearrangement and conformational modulation of substrate orientation. *ACS Catal.* **10**, 1195-1209 (2020).

81. Velazquez-Libera, J. L., Caballero, J., Tunon, I., Hernandez-Rodriguez, E. W. & Javier Ruiz-Pernia, J. On the nature of the enzyme-substrate complex and the reaction mechanism in human arginase I. A combined molecular dynamics and QM/MM study. *ACS Catal.* **10**, 8321-8333 (2020).

82. Saito, T. & Thiel, W. Quantum mechanics/molecular mechanics study of oxygen binding in hemocyanin. *J. Phys. Chem. B* **118**, 5034-5043 (2014).

83. Becke, A. D. Density-functional thermochemistry. III. The role of exact exchange. *J. Chem. Phys.* **98**, 5648-5652 (1993).

84. Pipek, J. & Mezey, P. G. A fast intrinsic localization procedure applicable for ab initio and semiempirical linear combination of atomic orbital wave-functions. *J. Chem. Phys.* **90**, 4916-4926 (1989).

85. Luis Casals-Sainz, J., Fernandez-Alarcon, A., Francisco, E., Costales, A. & Martin Pendas, A. Bond order densities in real space. *J. Phys. Chem. A* **124**, 339-352 (2020).

86. Menendez, M., Alvarez Boto, R., Francisco, E. & Martin Pendas, A. One-electron images in real space: natural adaptive orbitals. *J. Comput. Chem.* **36**, 833-843 (2015).

87. Gorelsky, S. I., Ghosh, S. & Solomon, E. I. Mechanism of N_2O reduction by the μ_4-S tetranuclear Cu_z cluster of nitrous oxide reductase. *J. Am. Chem. Soc.* **128**, 278-290 (2006).

88. Dapprich, S. & Frenking, G. Investigation of donor-acceptor interactions - a charge decomposition analysis using fragment molecular-orbitals. *J. Phys. Chem.* **99**, 9352-9362 (1995).

89. Mitoraj, M. P., Michalak, A. & Ziegler, T. A combined charge and energy decomposition scheme for bond analysis. *J. Chem. Theory Comput.* **5**, 962-975 (2009).

90. Lu, T. A comprehensive electron wavefunction analysis toolbox for chemists, Multiwfn. *J. Chem. Phys.* **161** (2024).

91. Lu, T. & Chen, F. Multiwfn: a multifunctional wavefunction analyzer. *J. Comput. Chem.* **33**, 580-592 (2012).

92. Mayer, I. Charge, bond order and valence in the ab initio SCF theory. *Chem. Phys. Lett.* **97**, 270-274 (1983).

93. Adamo, C. & Barone, V. Toward reliable density functional methods without adjustable parameters: The PBE0 model. *J. Chem. Phys.* **110**, 6158-6170 (1999).

94. Mayer, I. & Salvador, P. Overlap populations, bond orders and valences for 'fuzzy' atoms. *Chem. Phys. Lett.* **383**, 368-375 (2004).

95. Boys, S. F. & Bernardi, F. Calculation of small molecular interactions by differences of separate total energies - some procedures with reduced errors. *Mol. Phys.* **19**, 553 (1970).

96. Chen, K., Zhang, X., Wu, Y. D. & Wiest, O. Inhibition and mechanism of HDAC8 revisited. *J. Am. Chem. Soc.* **136**, 11636-11643 (2014).

97. Guo, W., Wu, A., Zhang, I. Y. & Xu, X. XO: An extended ONIOM method for accurate and efficient modeling of large systems. *J. Comput. Chem.* **33**, 2142-2160 (2012).

98. Guo, W., Wu, A. & Xu, X. XO: An extended ONIOM method for accurate and efficient geometry optimization of large molecules. *Chem. Phys. Lett.* **498**, 203-208 (2010).

99. Rao, L. *et al.* DOX: A new computational protocol for accurate prediction of the protein-ligand binding structures. *J. Comput. Chem.* **37**, 336-344 (2016).

100. Chung, L. W. *et al.* The ONIOM method and its applications. *Chem. Rev.* **115**, 5678-5796 (2015).

101. Ryde, U. & Soderhjelm, P. Ligand-binding affinity estimates supported by quantum-mechanical methods. *Chem. Rev.* **116**, 5520-5566 (2016).

102. He, J., Di Paola, C. & Kantorovich, L. Partitioning scheme for density functional calculations of extended systems. *J Chem Phys* **130**, 144104 (2009).

103. Stephens, P. J., Devlin, F. J., Chabalowski, C. F. & Frisch, M. J. Ab-initio calculation of vibrational absorption and circular-dichroism spectra using density-functional force-fields. *J. Phys. Chem.* **98**, 11623-11627 (1994).

104. Grimme, S., Ehrlich, S. & Goerigk, L. Effect of the damping function in dispersion corrected density functional theory. *J. Comput. Chem.* **32**, 1456-1465 (2011).

105. Francl, M. M. *et al.* Self-consistent molecular-orbital methods .23. a polarization-type basis set for 2nd-row elements. *J. Chem. Phys.* **77**, 3654-3665 (1982).

106. Clark, T., Chandrasekhar, J., Spitznagel, G. W. & Schleyer, P. V. Efficient diffuse function-augmented basis sets for anion calculations. 3. the 3-21+G basis set for first-row elements, Li-F. *J. Comput. Chem.* **4**, 294-301 (1983).

107. Mclean, A. D. & Chandler, G. S. Contracted gaussian-basis sets for molecular calculations .1. 2nd row atoms, z=11-18. *J. Chem. Phys.* **72**, 5639-5648 (1980).

108. Dolg, M., Wedig, U., Stoll, H. & Preuss, H. Energy-adjusted abinitio pseudopotentials for the 1st-row transition-elements. *J. Chem. Phys.* **86**, 866-872 (1987).

109. Stewart, J. J. P. Optimization of parameters for semiempirical methods V: modification of NDDO approximations and application to 70 elements. *J. Mol. Model.* **13**, 1173-1213 (2007).

110. Grimme, S., Antony, J., Ehrlich, S. & Krieg, H. A consistent and accurate ab initio parametrization of density functional dispersion correction (DFT-D) for the 94 elements H-Pu. *J. Chem. Phys.* **132**, 154104 (2010).

111. Sure, R. & Grimme, S. Comprehensive benchmark of association (free) energies of realistic host-guest complexes. *J. Chem. Theory Comput.* **11**, 3785-3801 (2015).

112. Cossi, M., Scalmani, G., Rega, N. & Barone, V. New developments in the polarizable continuum model for quantum mechanical and classical calculations on molecules in solution. *J. Chem. Phys.* **117**, 43-54 (2002).

113. Li, L., Li, C., Zhang, Z. & Alexov, E. On the 'dielectric "constant" of proteins: smooth dielectric function for macromolecular modeling and its implementation in DelPhi. *J. Chem. Theory Comput.* **9**, 2126-2136 (2013).

114. Yu, H. S., He, X., Li, S. L. & Truhlar, D. G. MN15: A Kohn-Sham global-hybrid exchange-correlation density functional with broad accuracy for multi-reference and single-reference systems and noncovalent interactions. *Chem. Sci.* **7**, 5032-5051 (2016).

115. Chan, B., Gill, P. & Kimura, M. Assessment of DFT methods for transition metals with the TMC151 compilation of data sets and comparison with accuracies for main-group chemistry. *J. Chem. Theory Comput.* **15**, 3610-3622 (2019).

116. Weigend, F. & Ahlrichs, R. Balanced basis sets of split valence, triple zeta valence and quadruple zeta valence quality for H to Rn: design and assessment of accuracy. *Phys. Chem. Chem. Phys.* **7**, 3297 (2005).

117. Marenich, A. V., Cramer, C. J. & Truhlar, D. G. Universal solvation model based on solute electron density and on a continuum model of the solvent defined by the bulk dielectric constant and atomic surface tensions. *J. Phys. Chem. B* **113**, 6378-6396 (2009).

118. M. J. Frisch *et al.* Gaussian 16 (Revision B.01; Gaussian, Inc.: Wallingford CT, 2016).

119. Gordon, J. C. *et al.* H++: a server for estimating pKas and adding missing hydrogens to macromolecules. *Nucleic Acids Res.* **33**, W368-W371 (2005).

120. Ti, S., Alushin, G. M. & Kapoor, T. M. Human β-tubulin isotypes can regulate

microtubule protofilament number and stability. *Dev. Cell* **47**, 175-190 (2018).

121. Schafer, A., Huber, C. & Ahlrichs, R. Fully optimized contracted gaussian-basis sets of triple zeta valence quality for atoms Li to Kr. *J. Chem. Phys.* **100**, 5829-5835 (1994).

122. Abraham, M. J. *et al.* GROMACS: high performance molecular simulations through multi-level parallelism from laptops to supercomputers. *SoftwareX* **1-2**, 19-25 (2015).

123. Maier, J. A. *et al.* ff14SB: improving the accuracy of protein side chain and backbone parameters from ff99SB. *J. Chem. Theory Comput.* **11**, 3696-3713 (2015).

124. Wang, J., Wolf, R. M., Caldwell, J. W., Kollman, P. A. & Case, D. A. Development and testing of a general amber force field. *J. Comput. Chem.* **25**, 1157-1174 (2004).

125. Schauperl, M. *et al.* Non-bonded force field model with advanced restrained electrostatic potential charges (RESP2). *Comm. Chem.* **3** (2020).

126. Lu, T. Sobtop, Version 1.0(dev3.1), http://sobereva.com/soft/Sobtop.

127. Zhang, Y., Jiang, Y., Peng, J. & Zhang, H. Rational design of nonbonded point charge models for divalent metal cations with Lennard-Jones 12-6 potential. *J. Chem Inf. Model.* **61**, 4031-4044 (2021).

128. Qiu, Y., Jiang, Y., Zhang, Y. & Zhang, H. Rational design of nonbonded point charge models for monovalent ions with Lennard-Jones 12-6 potential. *J. Phys. Chem. B* **125**, 13502-13518 (2021).

129. Jorgensen, W. L., Chandrasekhar, J., Madura, J. D., Impey, R. W. & Klein, M. L.

Comparison of simple potential functions for simulating liquid water. *J. Chem. Phys.* **79**, 926-935 (1983).

130. Bussi, G., Donadio, D. & Parrinello, M. Canonical sampling through velocity rescaling. *J. Chem. Phys.* **126** (2007).

131. Parrinello, M. & Rahman, A. Polymorphic transitions in single-crystals - a new molecular-dynamics method. *J. Appl. Phys.* **52**, 7182-7190 (1981).

132. Berendsen, H., Postma, J., Vangunsteren, W. F., Dinola, A. & Haak, J. R. Molecular-dynamics with coupling to an external bath. *J. Chem. Phys.* **81**, 3684-3690 (1984).

133. Darden, T., York, D. & Pedersen, L. Particle mesh ewald - an n.log(n) method for ewald sums in large systems. *J. Chem. Phys.* **98**, 10089-10092 (1993).

134. Humphrey, W., Dalke, A. & Schulten, K. VMD: Visual molecular dynamics. *J. Mol. Graph.* **14**, 33-38 (1996).

135. Huang, J. *et al.* CHARMM36m: an improved force field for folded and intrinsically disordered proteins. *Nat. Methods* **14**, 71-73 (2017).

136. Awoonor-Williams, E. & Rowley, C. N. The hydration structure of methylthiolate from QM/MM molecular dynamics. *J. Chem. Phys.* **149**, 45103 (2018).

Acknowledgments

This work was funded by Noncommunicable Chronic Diseases-National Science and Technology Major Project (2023ZD0503203 to Yi-Chun Zhu); the National Key R&D Program of China (2022YFE0205400 to Yi-Chun Zhu); the National Natural Science Foundation of China (NSFC) (32371227 and 31830042 to Yi-Chun Zhu, 32171194 to Qian-hui Qu); Science and Technology Development fund of Macau (FDCT 0007/2019/AKP, 003/2022/ALC and 0001/2024/AKP to Yi-Zhun Zhu); the Science and Technology Commission of Shanghai Municipality (21410761000 and 21140904200 to Yi-Chun Zhu); the start-up funds from Shanghai Stomatological Hospital & School of Stomatology, Fudan University (to Qian-hui Qu); the funding of innovative research team of high-level local universities in Shanghai and a key laboratory program of the Education Commission of Shanghai Municipality (ZDSYS14005 to Yi-Chun Zhu). The acetylomics and proteomics analyses were performed with the help of Shanghai Bioprofile Technology.

Author contributions

CS, SYC, KFX, YFW and XPM performed the experiments and analyzed the data; SYC designed the molecular dynamics and quantum chemical studies; CS, SYC, KFX, MYL, XPM, YFW, YLC, ZXZ, ZNZ and JQZ performed the experiments; IYZ and JWW provided instructions on molecular dynamics and quantum chemical studies; YC, WLX, MJW, AQC and QD analyzed the data; YZZ and BBT participated in the design of the studies; JLW, XQB and WM performed the LC-MS assays; CS and QHQ

designed and analyzed the structural studies; YCZ designed the whole studies and wrote the manuscript.

Data availability

The data supporting the findings of this manuscript are available from the corresponding author upon reasonable request. Model coordinates and density maps are available in the Protein Data Bank (PDB ID: 9K91) and the EM Data Bank (EMD-62184). Original LC-MS data for acetylomics are available via ProteomeXchange with identifier: PXD059553, token: hHqy6mNuliAC (acetylomics: CSE KO v.s. WT; HDAC6 KO v.s. WT); PXD059587, token: fRkU3n2xG5DY (proteomics: CSE KO v.s. WT; HDAC6 KO v.s. WT); PXD059540, token: UKM3vsMp8wHs (acetylomics: NaHS v.s. Vehicle); PXD059548, token: Osm8qYWYysQF (proteomics: NaHS v.s. Vehicle).

Supplementary Files

This is a list of supplementary files associated with this preprint. Click to download.

- uncutgelimageforthemanuscript.pdf
- D1300036976valreportfullP1.pdf
- D1300036976valreportfullP1.pdf
- SupplementaryVideos15forMolecularDynamicsSimulations.zip
- uncutgelimageforthemanuscript.pdf
- SupplementaryVideos610forMolecularDynamicsSimulations.zip
- VideoS1forFigure1acandS1.mp4
- VideoS2forFigureS2b.mp4
- uncutgelimageforthemanuscript.docx